Computational Investigations of Coordination Bonding and Adsorbate Properties in Metal-Organic Frameworks

by

Sudabeh Jawahery

A dissertation submitted in partial satisfaction of the

requirements for the degree of

Doctor of Philosophy

in

Chemical Engineering

in the

Graduate Division

of the

University of California, Berkeley

Committee in charge:

Professor Berend Smit, Chair
Professor Kranthi Mandadapu
Professor Mark Asta

Summer 2019

Computational Investigations of Coordination Bonding and Adsorbate Properties in Metal-Organic Frameworks

Abstract

Computational Investigations of Coordination Bonding and Adsorbate Properties in Metal-Organic Frameworks

by

Sudabeh Jawahery

Doctor of Philosophy in Chemical Engineering

University of California, Berkeley

Professor Berend Smit, Chair

In this thesis, I have used computational methods to the study of flexibility in metal-organic frameworks (MOFs) and the behavior of adsorbed gases and liquids in MOFs. Among nanoporous materials, MOFs are of particular interest for adsorption-based applications for reasons that include (1) their huge chemical space, which raises the possibility of tuning them for specific industrial processes and (2) the ability of the under-coordinated metals present in some MOFs to endow their respective materials with impressive adsorbate binding energies.

Chapters 2 and 4 relate to analogs of a series of MOFs with under-coordinated metals (the M-MOF-74 series). In Chapter 2, I report the discovery of a novel argon adsorbate-induced deformation pattern for this framework series. This result was arrived at using a flexible framework model, and is presented as an explanation for an intriguing signal observed in experimental small-angle X-ray scattering profiles upon argon adsorption. This hypothesis is supported by a complementary investigation of an alternative explanation for the X-ray signal, in which argon atoms are proposed to adsorb at different densities in adjacent pores.

In Chapter 3, I studied the dynamics of adsorbed xylene isomers in MOF-5. I compare the translational and rotational motion of the xylene isomers, and explain the differences based on molecular geometries. The most rod-like molecule, *para*-xylene, is more rotationally constricted in the pore due to its intermolecular interactions with the aromatic group of the MOF linker. This finding has implications for the rational design of MOFs, as a process that can take advantage of the MOF-induced variations in xylene isomer dynamics could be used for lucrative liquid-phase xylene separations.

In Chapter 4, I present a method for parameterizing the type of flexible framework model used in Chapter 2 from *ab initio* quantum chemistry calculations. The goal of this work is to facilitate the rapid development of flexible, versatile MOF models that can capture changes in the coordination bonding of metals in MOFs. This type of model can be used to study structural transitions and may be extended to study MOF formation. We demonstrated that our approach yields models for the M-MOF-74 series that are stable and have simulated structural properties in good agreement with quantum chemistry calculations.

Contents

Acknowledgments

I feel extraordinarily privileged for having had the opportunity to be a member of the MolSim@UC Berkeley and LSMO@EPFL Valais reasearch groups. I would like to extend my sincere gratitude to my advisor, Prof. Berend Smit. Without his scientific and practical advice, I would not have been able to see the most confusing (but also most rewarding) projects of my graduate career through to completion. Co-authoring papers with Prof. Smit has been an excellent learning experience, one which I believe has made me a better writer. An additional mentor that I wish to thank is Prof. Bess Vlaisavljevich, who introduced me to inorganic chemistry.

Working with external collaborators has been a pleasure. I wish to thank several members of the NMR community: Alex Forse, Velencia Witherspoon and Jeffrey Reimer have all been productive and pedagogical collaborators. I thank Mehrdad Asgari and Wendy Queen for including me in their neutron diffraction research. I have had the opportunity to work with computational colleagues performing rare event simulations, and thank Titus van Erp, Anders Lervik and Raffaela Cabriolu for their assistance and guidance. I thank Kristen Colwell for sharing ideas, inspiration and friendship with me over the last five years.

Working with all of my fellow labmates at both UC Berkeley and EPFL Valais has been an experience that I will cherish for the rest of my life. I wish to thank Cory Simon, Bess Vlaisvaljevich, Efrem Braun, Rocío Mercado, Sondre Schnell, Matthew Witman, Mohamad Moosavi and Nakul Rampal for all our work together. I once again thank Rocío Mercado, Matthew Witman and Efrem Braun, as well as Katie Deeg, Michelle Liu and Johanna Huck, for the sense of camaraderie we fostered as a group during our travels between California and Switzerland. I wish to thank Peter Boyd, Amber Mace and Senja Barthel for their assistance on the work we did together but did not publish. An additional thanks to Daniele Ongari, Lennart Joos, Özge Kadıoğlu, Henglu Li, Gloria Capano, Davide Tiana, Leopold Talirz, Aliaksandr Yakutovich, Andrés Ortega Guerrero and Olga Syzgantseva.

The work in this thesis would not have been possible without computational resources and the "kindness of strangers". I thank Kelley McDonald and NERSC for facilitating the calculations. I thank also the National Science Foundation for a Graduate Research Fellowship that funded the first three years of my PhD, to the U.S. Department of Energy for funding this research through the Center for Gas Separations and to the Peder Sather Center at UC Berkeley for making my rare event collaboration possible. I appreciate the administrative help I have received from Carlet Altamirano, Evelyn Ludi and Kristin Stangl.

Finally, I thank my husband, my parents, my in-laws and my friends for their unwavering support. Interacting with them, virtually or in the flesh, has brought much-needed perspective and joy to my life throughout this journey.

Chapter 1

Introduction

> *In the universe, an important mark of a civilization's technological advancement is its ability to control and make use of micro dimensions. Making use of fundamental particles without taking advantage of the micro dimensions is something that our naked, hairy ancestors already began back when they lit bonfires within caves. Controlling chemical reactions is just manipulating micro particles without regard to the micro dimensions. Of course, this control also progressed from crude to advanced: from bonfires to steam engines, and then generators. Now, the ability for humans to manipulate micro particles at the macro level has reached a peak: We have computers and nanomaterials. But all of that is accomplished without unlocking the many micro dimensions. From the perspective of a more advanced civilization in the universe, bonfires and computers and nanomaterials are not fundamentally different. They all belong to the same level. Thats also why they still think of humans as mere bugs. Unfortunately, I think they're right.*
>
> — Liu Cixin, The Three-Body Problem

The publication of several landmark papers in the late 20th century on metal-organic frameworks (MOFs)[1, 2, 3, 4] culminated in the synthesis of the canonical MOF-5 (also known as IRMOF-1) framework[5]. MOF-5 was the first example of a MOF that could demonstrate permanent, stable porosity without the presence of guest molecules inside the structure[5]. The general study of coordination chemistry and complexes, however, dates back to the beginning of modern chemistry[6]. Coordination complexes are molecules in which metal centers bind to electron-donating ligands (which can be ions, atoms, or other molecules)[6]. The vertices of MOFs and, by extension, MOFs themselves, are coordination complexes[7]. The science used to rationalize coordination complexes makes up a large part of the science that governs and allows researchers to understand and explain the stability and formation of MOFs. Other fundamental science fields contributing to the study of MOFs include crystallography, statistical thermodynamics, transport phenomena, and the physical chemistry of surfaces and solutions. By considering and combining our knowledge of the

different fields relevant to the study of MOFs, the scientific community can seek to improve its ability to manipulate and take advantage of the possibilities offered by this relatively new class of materials.

1.1 Properties of Metal-Organic Frameworks

MOFs are a class of crystalline, three-dimensional, nanoporous, hybrid organic-inorganic solids that are currently being widely studied for potential applications in a variety of fields, including, but not limited to, carbon capture[8], energy storage[9, 10], catalysis[11, 12, 13], and drug delivery[14, 15]. MOFs are synthesized using different combinations of constituent metal and organic linker building blocks, a feature which allows them to be tuned for different practical purposes[16]. The large number of possible building block combinations has resulted in the experimental synthesis of tens of thousands of MOFs[17], and the computational prediction of hundreds of millions[18, 19]. Fig 1.1 shows a schematic of linkers and metals forming a MOF.

Because of their porosity and frequently large internal surface areas, MOFs are promising candidates for adsorption-based applications such as gas separations and storage. The implications for gas adsorption properties of the various crystal structures that result from different building block combinations have therefore been thoroughly investigated[20, 21, 22, 23]. One of the most interesting and promising structural characteristics found in MOFs is the open-metal site[24, 25]. In frameworks possessing open-metal sites, the metal centers are coordinated to one less ligand atom than is thermodynamically favored: the system energy will decrease in the event that an additional ligand atom forms a coordination bond with the metal center. Open-metal sites form because a solvent molecule remains bound to the metal center during the crystallization process such that the framework metals initially have the thermodynamically-favored number of ligands. The solvent molecules can be removed after synthesis by a process called activation (often accomplished by heating the framework in vacuum conditions) such that the open-metal site is exposed[26]. These sites should decorate the rim of of an accessible pore - if the open site metal centers were not located in accessible pores, the detaching solvent molecules would not be able to leave the framework upon activation.

Open-metal sites endow MOFs with superior adsorptive capabilities because they enable the metal centers to form coordination bonds with certain adsorbents. Coordination bonds are stronger than typical physisorption interactions (a typical coordination bond energy is > 100 kJ/mol, compared with physisorption interactions ranging from 1-10 kJ/mol)[6, 27]. The potential of open-metal sites has been explored for a number of different adsorption applications, including hydrocarbon separations[28], air separations[29], carbon capture[30] and many more. Combined with the aforementioned structural versatility manifest in MOFs, it is possible to imagine engineering targeted, high-performance solid sorbents that include both open-metal sites and tailored ligand and structural properties. The reality is more challenging: the number of framework series in which stable, permanent open-metal sites

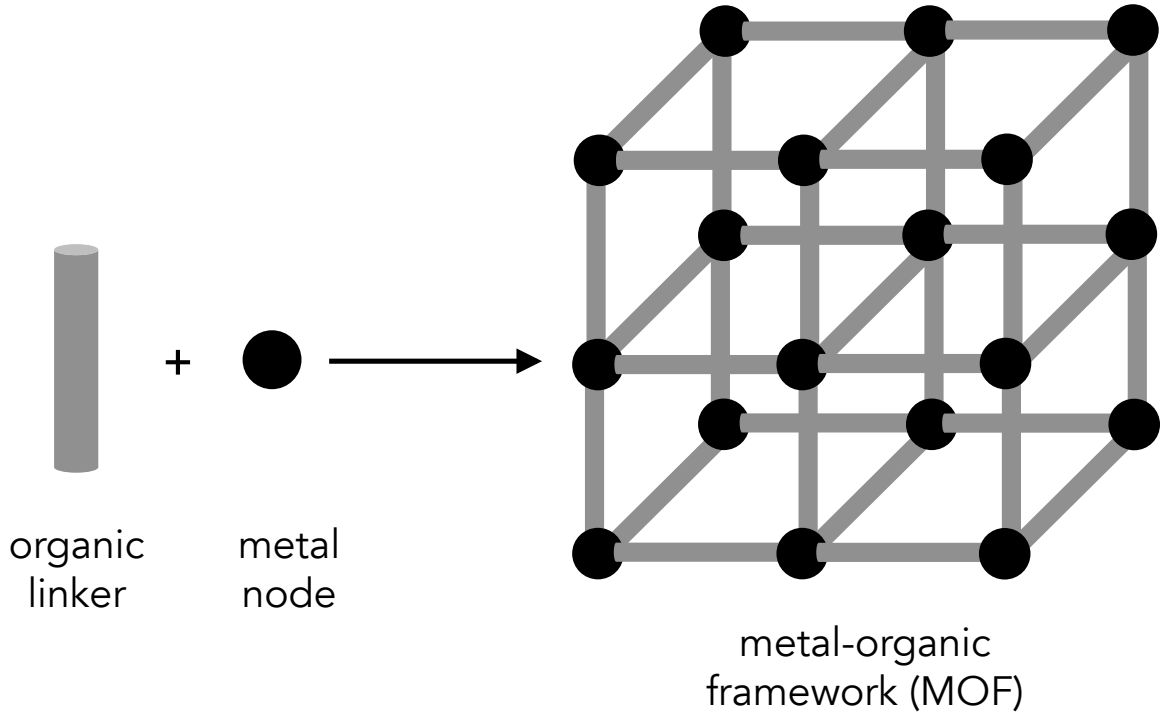

Figure 1.1: A schematic demonstrating how organic linker molecules and metal nodes combine via coordination bonds to form the three-dimensional, porous crystalline structures characteristic of MOFs. The cubic lattice shown in the schematic resembles the canonical MOF-5 structure, but a huge variety of pore geometries and framework topologies have been synthesized. Organic linker molecules contain atoms capable of forming coordination bonds with an electron-withdrawing metal center, such as oxygen, nitrogen, or sulfur.

have been observed are limited[30, 31, 32], which in turn limits the tunability of open-metal sites. Because only a select few frameworks containing open-metal sites can be synthesized, it not yet possible to fully take advantage of them via targeted design for storage and separation applications.

From their outset, MOFs sparked a revolution in reticular chemistry, a field based on synthesizing and predicting the structures of porous materials by linking together building block molecules[33, 34, 35, 36]. From the perspective of computational researchers, the sheer number of potentially realizable MOFs offers the scientific community an unprecedented chance to use the predictive power of computational methods. Applications of computational methods to MOFs have predicted large databases of crystal structures[19, 37] as well as assessed the performance of large MOF databses for different physisorption-based applications[38, 39]. Such significant progress has been made in computational database screening over the course of the last decade that a burden has been placed on experimental researchers to develop high-throughput methods of synthetizing MOFs, which has in turn led to the development of computational methods to streamline these procedures[40, 41].

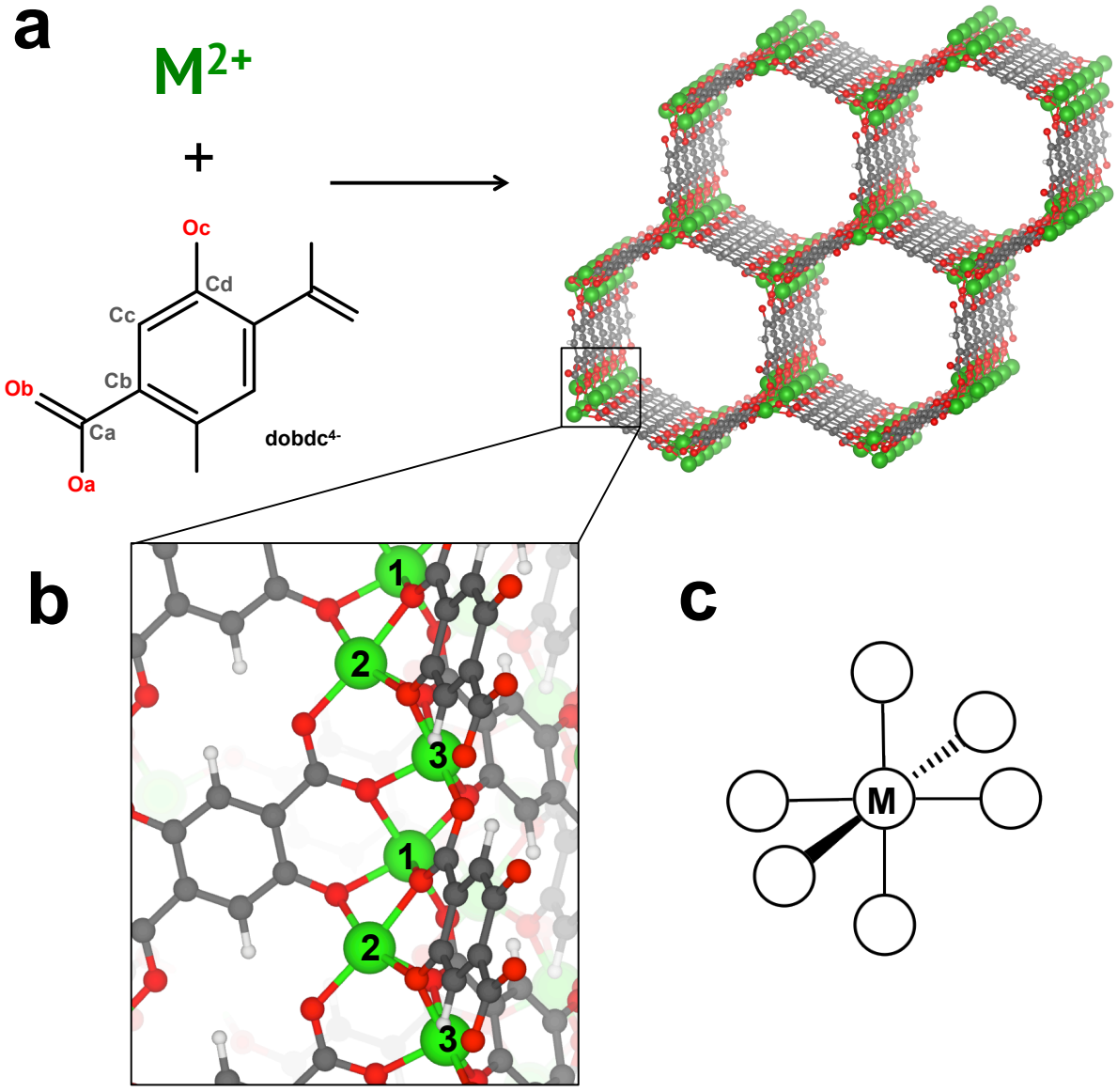

Figure 1.2: (a) A schematic showing how the dobdc^{4-} ligand and metal cations form the M-MOF-74 structure (M^{2+} = Mg, Mn, Fe, Co, Ni, Cu, Zn, Cd), which possesses one-dimensional hexagonal channels. (b) A view of the M-MOF-74 helix from inside a one-dimensional channel. Each turn of the metal helix is composed of three metals - two sets of repeating helix metals have been labeled. The helical axis points in the same direction as the one-dimensional channels. (c) A visual aid showing the octahedral coordination geometry of the metal centers. In the activated state, each metal is bound to five ligand oxygens, and one coordination site remains unoccupied. In (a) and (b), oxygen, metal, carbon and hydrogen atoms are shown in red, green, grey and white, respectively.

Computational methods are not yet able, however, to predict MOF formation independently. In the last few years, researachers have used molecular simulations to study MOF formation via molecular simulation without accurately capturing the framework coordination bond energies[42, 43, 44, 45], meaning that their observations, while insightful, cannot be easily related to experiments. Computational predictions of formation and growth would provide the MOF community with crucial insight that could help achieve the dream of designing and commercializing materials for specific applications. Predicting MOF formation is therefore a motivating factor for me to develop methods to characterize the coordination chemistry of metals in MOFs.

Among the most widely studied isoreticular series of MOFs containing open-metal sites is the M-MOF-74 series, also known as the IRMOF-74 series. The original example of a framework in this series is shown in Fig. 1.2. M-MOF-74, also known as M_2(dobdc) and CPO-27, is synthesized from dobdc^{4-} = 2,5-dioxido-1,4-benzenedicarboxylate ligands and M^{2+} metal cations, which are frequently transition metals (M^{2+} = Mg, Mn, Fe, Co, Ni, Cu, Zn, Cd)[46, 47, 48, 49, 50, 51, 52]. Multivariate versions of M-MOF-74, wherein multiple metal cations existing within the same framework, have also been synthesized[53]. The structural and coordination properties of this framework series are studied in Chapters 2 and 4 of this thesis.

Fig. 1.2a shows a view of the channels of M-MOF-74. The one-dimensional hexagonal channels point in the direction of the crystalline c-axis, while the a- and b-axes are equivalent when the crystal is described in the $R3$ and $R\overline{3}$ space groups. The crystalline axes are discussed in more detail in Chapter 2. Also pointing in the direction of the c-axis are the metal helices, the location of which is boxed with a solid black line in Fig. 1.2a. The metal helices make up the vertices of the hexagonal channels, and the linker molecules stack in the direction of the c-axis. A different view of the helix structure, from a position inside of the channel, is displayed in Fig. 1.2b. A single turn of the metal helix consists of three metals, two sets of which are labeled in Fig. 1.2b. The adjacent vertices of the hexagonal channels (vertices connected by the same row of linkers) alternate between left-handed and right-handed helices.

The coordination geometry of each metal in the structure is octahedral, an example of which is shown in Fig. 1.2c. The framework metals are thermodynamically driven to bind to six ligand atoms, but upon activation the metals form only five bonds with linker oxygens. The remaining coordination site (the open-metal site) points towards the center of a channel, allowing it to form bonds with adsorbate molecules. Several recent works have focused on modeling the strength of the coordination bond formed between the metal center and adsorbate molecules[24, 25, 54]. Chapter 4 of this thesis focuses on modeling the coordination bond between metals and linker oxygens.

1.2 Classical Modeling of Coordination Chemistry

MOFs are not the only field where coordination chemistry intersects with other fundamental sciences. Metal ions play a role in a vast number of biological systems[55, 56, 57] mainly through their interactions with proteins that contain metal cofactors. Proteins (and enzymes) that complex with metals are termed metalloproteins (and metalloenzymes). Metal ions influence the behavior of metalloproteins in a variety of ways. In some cases, the metal ions are important for the conformational dynamics of the protein[58, 57], which can regulate function by influencing the interactions of the protein with its environment. For metalloenzymes, the metal ions cofactors are essential for the catalytic function of the enzyme[59, 55].

The coordination chemistry bonds formed by metal ions in metalloproteins are most accurately described using quantum chemistry techniques, such as density functional theory (DFT). However, most systems of biological interest pose a feasibility challenge for quantum chemistry methods due to their large size. Protein systems contain hundreds of atoms, and the inclusion of explicit solvent molecules, which can be necessary to capture protein structure, makes the system size an even greater challenge[60, 61]. Until now there have been only sparse examples in the literature of DFT studies on biological systems, most of which use implicit rather than explicit solvent[62]. More progress is required before DFT will be able to make quantitative predictions of large systems of biological relevance[62].

The challenge of studying coordination chemistry as it relates to biology led to the development of new classical simulation techniques, which have the advantage of being computationally-efficient and compatible with existing classical models of proteins and solvents. Efforts dating back to the early 1990s have led to an active field within molecular simulations in which researchers attempt to capture the energetics and geometry of coordination complexes using novel models. Johan Åqvist and Arieh Warshel were the first to propose a strategy that will hereafter be referred to as the cationic dummy model (CDM)[59, 63], in which the coordination chemistry of a metal cation is captured through the use of fractional positive charges that surround the metal center, as opposed to assigning the full ionic charge to the metal center. The fractional charges are arranged to mimic the coordination geometry of the metal cation of interest, as shown by the examples in Fig. 1.3.

Fig. 1.3a shows the original cationic dummy model proposed by Åqvist and Warshel[59, 63]. In this model for octahedrally-coordinated metal cations, all dummy sites are equivalent (equidistant from the central metal site with equal charges). In recent years, several parameterizations for the dispersive interactions of the beads of this model with surroundings have appeared in literature[58, 64], but the underlying geometry and charge distribution has remained unchanged. While this model explicitly mimics six coordination bond sites, combined with appropriate van der Waals parameters it has even been able to capture the seven-coordinate geometry of Ca^{2+}, although explicit seven-coordinate models do also exist[65]. Fig. 1.3b shows a variation of the original Åqvist and Warshel model designed to capture Jahn-Teller distortions in Cu^{2+}[66]. Finally, the model shown in Fig. 1.3c was proposed by Pang[67, 68] to study tetrahedrally-coordinated Zn^{2+}.

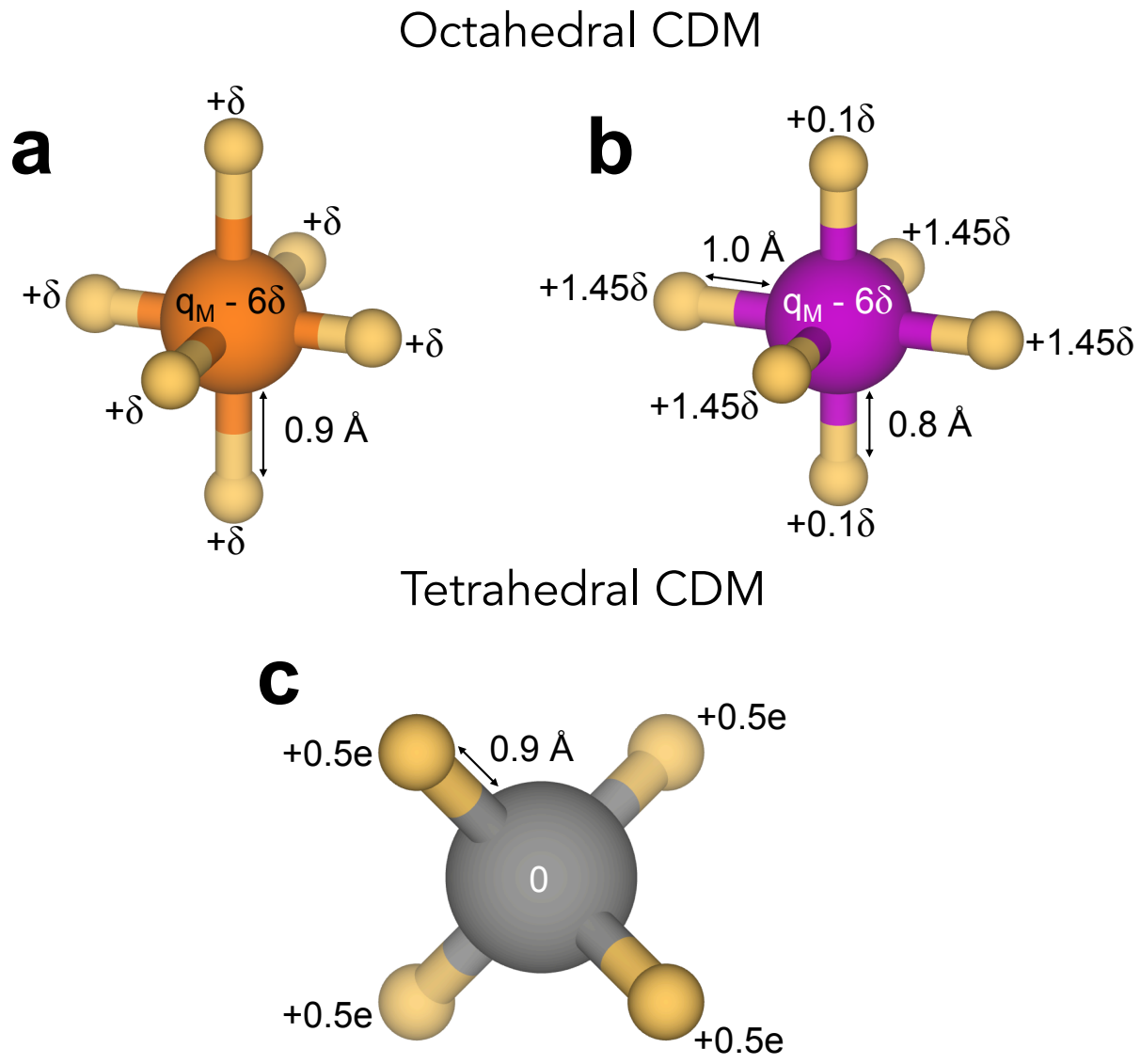

Figure 1.3: (a) and (b) show examples of octahedral CDM found in the literature, while (c) shows an example of a tetrahedral CDM from literature. Light orange beads represent dummy sites bound to a central metal site. The charge distributions of the models are marked in the figure. The octahedral CDM shown in (a) has been applied in recent years to metal cations with both $q_M = +2$[58, 64] and $q_M = +3$[66]. The value of δ in (a) depends then on the metal being studied. (b) was parameterized to capture Jahn-Teller distortions in Cu^{2+}, which is why the axial and equitorial metal-dummy bond lengths and charges are different[69]. (c) was parameterized specifically for tetrahedrally-coordinated Zn^{2+}[67, 68], and the central site has no charge.

The simplicity and proven versatility of the CDM approach makes it possible to envision deploying them as a solution in other systems where coordination bonding is important. I was motivated to incorporate CDMs into my work in order to address the unmet challenge of describing the coordination environment of metals in MOFs. As I have already mentioned, being able to study coordination bonds of MOFs with computationally efficient methods would allow us make predictions about crystal structure formation, as well study structural transitions that involve changes in the coordination geometry without the cleavage of bonds. The use of CDMs is therefore featured in the work presented in Chapter 2 and Chapter 4.

It should be noted that CDMs are not the only possible route for capturing coordination bonds with classical models. Polarizable models have also been parameterized to capture coordination bonding[70, 71]. The major drawbacks of the polarization approach are the high computational expense and extra code machinery required to be able to apply it to a large system. The polarizable transition metal models that have been parameterized thus far require evaluation of forces resulting from induced electrostatic potentials[72], which is not available as a feature in many common simulation packages. Furthermore, most tailor-made MOF models that have been developed to capture other properties are non-polarizable[25, 73]. My goal is to build and expand upon the literature such that coordination bonding properties can be predicted and used. CDMs are therefore a better choice because they are less computationally expensive and can be more seamlessly combined with existing MOF models than polarizable models.

1.3 Simulation Methods Used in this Thesis

Before discussing the simulations of MOFs presented in Chapters 2, 3, and 4, I will introduce the molecular simulation methods that are employed in this thesis. I will explain the background of each technique and describe how they are applied to the projects included in the subsequent chapters.

Grand Canonical Monte Carlo Simulations

Grand Canonical Monte Carlo (GCMC) simulations probe the thermodynamic μVT ensemble, where μ is the chemical potential of a molecule in an external reservoir, V is the volume of the system being simulated and T is the system temperature[74]. This ensemble is also known as the Grand canonical ensemble. GCMC simulations of MOFs probe the adsorption of the the reservoir molecule with chemical potential μ in the framework. We perform GCMC simulations using Markov chain Monte Carlo (MC) moves. For Markov chain MC moves, we can write the following relation[74]:

$$\frac{\mathrm{acc}(s^0 \to s^1)}{\mathrm{acc}(s^1 \to s^0)} = \frac{\alpha(s^1 \to s^0)\mathcal{N}(s^1)}{\alpha(s^0 \to s^1)\mathcal{N}(s^0)} \tag{1.1}$$

where the acceptance (acc) terms are the probability of accepting a proposed MC move forwards and backwards between an original state (s^0) and a new state (s^1), $\mathcal{N}$ terms are the probability densities of the two states, and α terms come from the transition matrix of the Markov chain. We normally design algorithms such that α is symmetric and the terms cancel out with each other. In the statistical thermodynamic context we are interested in, the $\mathcal{N}$ terms for each state can be ratios of the contributions of each state to a total partition function common to both states (both states contribute to the same partition function). Although the total partition function is usually not quantifiable, we are only interested in the ratios between the $\mathcal{N}$ terms for each state, so the total partition function will cancel out.

We are interested in three kinds of moves for simulations of adsorbate molecules in MOFs: particle insertions, particle deletions and particle translations.

Adsorbate Translation Moves

For molecule translation moves, an adsorbate molecule to displace is chosen at random, thus rendering the transition matrix symmetric such that the α terms in Eq. 1.1 cancel out. Because s^0 and s^1 have the same number of molecules N, the relevant total partition function is simply the canonical partition function, and the probability density for each state can be written as:

$$\mathcal{N}(s) = \frac{\exp^{-\beta U(s)}}{\mathrm{Q}(N)} \tag{1.2}$$

where $U(s)$ is the potential energy function evaluated at state s. Substituting the $\mathcal{N}$ terms from Eq. 1.2, for each state into Eq. 1.1, we arrive at the following acceptance ratio:

$$\frac{\mathrm{acc}(s^0 \to s^1)}{\mathrm{acc}(s^1 \to s^0)} = \frac{\exp^{-\beta U(s^N)}}{\exp^{-\beta U(s^0)}} = \exp^{-\beta(U(s^N) - U(s^0))} \tag{1.3}$$

From Eq. 1.3, we know what the ratio of acceptance moves for moving between states s^0 and s^1 must be in our simulation. To achieve this ratio, we can apply the Metropolis algorithm to arrive at the following acceptance rule[74]:

$$\mathrm{acc}(s^0 \to s^1) = \min\left(1, \exp^{-\beta(U(s^N) - U(s^0))}\right) \tag{1.4}$$

Adsorbate Insertion Moves

For molecule insertion moves, we consider two states that different numbers of adsorbate molecules: $s^0 \equiv s^N$ and $s^1 \equiv s^{N+1}$, where N and $N+1$ refer to the number of molecules in the system. Both of these states are part of a system where a MOF framework is exchanging adsorbate molecules with an external reservoir maintained at a chemical potential μ. In order to again cancel out the α term in Eq. 1.1, we attempt a molecule insertion on the s^N state with equal likelihood to a molecule deletion from the s^{N+1} state. The full derivation of

the acceptance ratio probability is lengthy and available in literature[74]. It has been shown that the acceptance ratio is:

$$\frac{\mathrm{acc}(N \to N+1)}{\mathrm{acc}(N+1 \to N)} = \frac{\mathrm{V}}{(N+1)\Lambda^3} \exp^{\beta\mu} \exp^{-\beta(U(s^{N+1}) - U(s^N))} \tag{1.5}$$

where Λ is the de Broglie thermal wavelength. This ratio leads to the following Metropolis acceptance rule:

$$\mathrm{acc}(N \to N+1) = \min\left(1, \frac{\mathrm{V}}{(N+1)\Lambda^3} \exp^{\beta\mu} \exp^{-\beta(U(s^{N+1}) - U(s^N))}\right) \tag{1.6}$$

Adsorbate Deletion Moves

Molecule deletion moves complement insertion moves. Because we attempt them with equal likelihood to insertions, the α terms in both our molecule insertion and deletion acceptance ratios cancel out. It has been shown that the acceptance ratio to move between states $s^0 \equiv s^N$ and $s^1 \equiv s^{N-1}$ is[74]:

$$\frac{\mathrm{acc}(N \to N-1)}{\mathrm{acc}(N-1 \to N)} = \frac{N\Lambda^3}{\mathrm{V}} \exp^{-\beta\mu} \exp^{-\beta(U(s^{N-1}) - U(s^N))} \tag{1.7}$$

This ratio leads to the following Metropolis acceptance rule:

$$\mathrm{acc}(N \to N-1) = \min\left(1, \frac{N\Lambda^3}{\mathrm{V}} \exp^{-\beta\mu} \exp^{-\beta(U(s^{N-1}) - U(s^N))}\right) \tag{1.8}$$

GCMC simulations have been applied in Chapter 2 to study the role of the long-range argon interactions on adsorption isotherms in a microporous MOF, and in Chapter 3 to determine the liquid-phase loading of xylene isomers in MOF-5. The chemical potentials of argon and xylene isomers are determined by the ideal gas law and, as for xylene the pressure of interest are outside the pressure range for which the ideal gas law holds, the Peng-Robinson equation of state, respectively.

Molecular Dynamics Simulations

Molecular Dynamics (MD) is a simulation method that produces trajectories of system coordinates and velocities. When MD is applied to atomistic scale systems, such as MOFs, the resulting trajectories can be used to extract molecular-level insight into the mechanisms, energetics and driving forces of adsorbate dynamics and framework behavior, both with and without the presence of adsorbate molecules. We are accustomed to Newton's Law, which defines the dynamics of all atoms i in a molecular system:

$$F_i(t) = m_i \frac{d^2 r_i(t)}{dt} \tag{1.9}$$

where the force F_i on atom i is given by:

$$F_i(t) = -\frac{\partial U(r^N(t))}{\partial r_i} \tag{1.10}$$

where $U(r^N(t))$ is the potential energy function evaluated based on all atoms $i = [1...N]$ at their respective positions at instantaneous time t.

In order to integrate the motion of a given simulation system in time, we use the velocity-verlet algorithm, which requires us to store in computer memory the value of the atomic positions r_i and velocities v_i at the same moment in time t[75, 76]:

$$\begin{aligned} r_i(t + \Delta t) &= r_i(t) + v_i(t)\Delta t + \frac{\Delta t^2}{2m_i} F_i(t) \\ v_i(t + \Delta t) &= v_i(t) + \frac{\Delta t}{2m}(F_i(t) + F_i(t + \Delta t)) \end{aligned} \tag{1.11}$$

Integrating the above equations produces dynamics in the the thermodynamic NVE ensemble, also known as the microcanonical ensemble. If we wish to see Eq. 1.9 and Eq. 1.10 according to Hamiltonian convention, we can write[75, 76]:

$$\dot{r_i} = \frac{p_i}{m_i} \tag{1.12}$$

where p_i is the momentum of atom i and $\dot{p_i}$ is equivalent to the force (Eq. 1.11):

$$\dot{p_i} = -\frac{\partial U(r^N(t))}{\partial r_i} \tag{1.13}$$

The Hamiltonian convention of writing the equations of motion is convenient as we move to the NVT and NPT ensembles. In the NVT ensemble, also known as the canonical ensemble, the temperature of the system is kept constant while the energy varies. In order to keep the system temperature constant, we must apply a thermostat. Maintaining a constant temperature while producing a canonical distribution of velocities and configurations is non-trivial[77]. In the NVT ensemble MD simulations presented in Chapters 2, 3 and 4, we have used the Nosé-Hoover thermostat[78, 79], in which the definition of $\dot{p_i}$ is replaced[75, 76]:

$$\dot{p_i} = -\frac{\partial U(r^N(t))}{\partial r_i} - \xi p_i \tag{1.14}$$

The Nosé-Hoover thermostat introduces an extra degree of freedom that acts as a thermal reservoir, and results in the second term containing ξ in Eq. 1.14. The dynamics of ξ are as follows[75, 76]:

$$\dot{\xi} = \frac{1}{Q}(\sum_i \frac{p_i^2}{m_i} - \frac{(g+1)}{\beta}) \tag{1.15}$$

where $g = 3N$, relating to the degrees of freedom of the system as N is the number of atoms, and Q is a fictitious mass that determines the strength of the thermostat coupling. The

target temperature for the NVT ensemble simulation is used to compute the value of β. Eq. 1.13, Eq. 1.14 and Eq. 1.15 form a closed set of equations[75, 76] that can be used to deterministically integrate motion while sampling a target temperature range.

In the NPT ensemble, also known as the isothermal-isobaric ensemble, the temperature and pressure of the system are kept constant while both the energy and the volume are allowed to fluctuate. Several methods to change the simulation unit cell volume to maintain the correct pressure exist in literature[74, 75], but the most appropriate technique for crystal structures is the Parrinello-Rahman barostat, which was used in the NPT ensemble simulations presented in Chapter 2[80, 81, 82]. Parrinello and Rahman proposed a method that allows the components of the simulation cell vectors to change, meaning that simulated crystal structures can deform in response to the chosen interatomic potential. The Parrinello-Rahman strain energy can be formulated in a Hamiltonian convention and combined with the thermal reservoir variable of Nosé, yielding NPT dynamics.

The simulation volume is fully described by the $3x3$ matrix h, where $h = (\vec{a}, \vec{b}, \vec{c})$ and $\vec{a}$, $\vec{b}$ and $\vec{c}$ are the box vectors of the three-dimensional simulation cell. The resulting equations of motion for the atomic positions and momenta are[83]:

$$\begin{aligned} \dot{r_i} &= \frac{p_i}{m_i} + \frac{p_b}{W} r_i \\ \dot{p_i} &= -\frac{\partial U(r^N(t))}{\partial r_i} - \frac{p_b}{W} p_i - \frac{1}{g} \frac{\mathrm{Tr}(p_b)}{W} p_i - \frac{p_\eta}{Q} p_i \end{aligned} \tag{1.16}$$

The resulting equations of motion for simulation cell matrix h and a related momentum are[83]:

$$\begin{aligned} \dot{h} &= \frac{p_b h}{W} \\ \dot{p_b} &= (P_{int} - P_{ext} I) \det h + \frac{1}{g} (\sum_i \frac{p_i^2}{m_i}) I - \frac{p_\eta}{Q} p_b \end{aligned} \tag{1.17}$$

where W is a fictitious mass that determines the strength of the barostat coupling, P_{ext} is the applied external pressure and P_{int} is the pressure tensor of the simulated system. The resulting equations of motion for the extra thermal variable, termed η here to distinguish from the case of Nosé-Hoover NVT dynamics, and its momentum are[83]:

$$\begin{aligned} \dot{\eta} &= \frac{p_\eta}{Q} \\ \dot{p_\eta} &= \sum_i \frac{p_i^2}{m_i} + \frac{\mathrm{Tr}(p_b^T p_b)}{W} - \frac{(g + d^2)}{\beta} \end{aligned} \tag{1.18}$$

where d is the dimensionality of the system[83].

Force Fields

In both GCMC and MD simulations, the interatomic potential evaluated at a given system configuration $U(r^N)$ drives and, in the case of MD, determines the results of the simulation. In classical molecular simulations, all interatomic interactions are defined by functions that depend on geometric properties of the system. These interactions can be split into three main subgroupings:

$$U(r^N) = U_{\text{VdW}}(r^N) + U_{\text{Bonded}}(r^N) + U_{\text{Coulombic}}(r^N) \tag{1.19}$$

Interactions contributing to $U_{Bonded}(r^N)$ are invoked by, for example, pairs of atoms in the same covalently bonded molecule. In this case, the distances between neighboring bonded atoms or the angle shared by a set of three atoms may be linked to a potential energy function such that deviations from a prescribed geometry are penalized. In this thesis, two different force fields are used to describe intramolecular covalent bonds and their associated higher order terms: the Consistent Valence Force Field (CVFF)[84] and the DREIDING Force Field[85].

Contributions to $U_{\text{VdW}}(r^N)$ and $U_{\text{Coulombic}}(r^N)$ are usually invoked between pairs of atoms that are not already contributing to $U_{\text{Bonded}}(r^N)$. $U_{\text{Coulombic}}(r^N)$ takes a predictable functional form based on Coulomb's law. For any pair of charged atoms i and j, their contributions to $U_{\text{Coulombic}}(r^N)$ is as follows:

$$U_{ij}^{\text{Coulombic}} = \frac{q_i q_j}{4\pi\epsilon_0 r_{ij}} \tag{1.20}$$

where q_i and q_j are the atomic charges, ϵ_0 is the permittivity of free space and r_{ij} is the distance between the atom pair.

Three different functional forms are used to describe contributions to $U_{VdW}(r^N)$:

$$U_{ij}^{\text{Lennard-Jones}} = 4\epsilon_{ij}((\frac{\sigma_{ij}}{r_{ij}})^{12} - (\frac{\sigma_{ij}}{r_{ij}})^{6}) \tag{1.21}$$

$$U_{ij}^{\text{Buckingham}} = A_{ij}e^{-B_{ij}r_{ij}} - \frac{C_{ij}}{{r_{ij}}^6} \tag{1.22}$$

$$U_{ij}^{\text{Born-Mayer-Huggins}} = A_{ij}e^{B_{ij}(\sigma - r_{ij})} - \frac{C_{ij}}{{r_{ij}}^6} \tag{1.23}$$

The non-mathematical terms in Eq. 1.21, Eq. 1.22 and Eq. 1.23 other than the interatomic distance r_{ij} are fitted parameters specific to the pair for which the potential is being evaluated. Prior research works have studied how to best apply the Lennard-Jones potential (Eq. 1.21) and Buckingham potential (Eq. 1.22) to capture adsorbate-framework interactions in the M-MOF-74 series[54, 24, 25]. In Chapter 4, I discuss how to best apply the Born-Mayer-Huggins potential (Eq. 1.23) to capture metal coordination chemistry in the same series of frameworks.

Chapter 2

Adsorbate-Induced Lattice Deformation in M-MOF-74 Series

In this work, we study the unique framework deformation that can occur as a result of low-temperature gas adsorption in the M-MOF-74 series. M-MOF-74 analogs are among the most widely studied MOFs for adsorption applications because of their one-dimensional channels and high metal density. Most studies involving the M-MOF-74 series assume that the crystal lattice is rigid. This assumption guides the interpretation of experimental data, as changes in the crystal symmetry have never been reported and are in general ignored as a possibility in the literature. Here, we report a deformation pattern, induced by the adsorption of argon, for an extended Mg-MOF-74 analog where the 2,5-dioxido-1,4-benzenedicarboxylate (dobdc) ligand has five aromatic rings rather than the usual single ring. This framework will henceforth be referred to as IRMOF-74-V. This work has two main implications. First, we use molecular simulations to demonstrate that IRMOF-74-V undergoes a deformation that is similar to the mechanism behind breathing MOFs, but is unique because the deformation pattern extends beyond a single unit cell of the original structure. Second, we provide an alternative interpretation of experimental small-angle X-ray scattering profiles of these systems, which changes how we view the fundamentals of adsorption in this MOF series.

This chapter is based on material from the following publication:

S. Jawahery, C. M. Simon, E. Braun, M. Witman, D. Tiana, B. Vlaisavljevich, B. Smit. Adsorbate-Induced Lattice Deformation in IRMOF-74 Series. *Nature Communications*, **2017**.

2.1 Introduction

Effective optimization of MOFs for adsorption-based applications depends on our ability to engineer their chemistry to modulate their selectivity and capacity for different gas molecules. A fundamental understanding of the mechanisms of adsorption in MOFs and their response to gas adsorption is therefore crucial.

Several MOFs whose crystal structures respond to adsorbing gas molecules by undergoing reversible, structural transitions have been reported in the literature[86] and studied theoretically[87, 88, 89]. Adsorbate-induced deformations of MOFs can cause dramatic changes in unit cell parameters, as in the cases of breathing or swelling MOFs. Swelling mechanisms that allow MOFs to expand as pores fill with adsorbates have been identified[90]. More complex breathing mechanisms have also been observed where, upon insertion of some adsorbates at low gas phase pressures, the MOF exhibits a transition from an expanded, porous state to a more collapsed state, before expanding yet again to the porous state at higher gas phase pressures[91, 92, 93]. The structural transitions can also be more subtle, as in the case of MOFs whose ligands undergo a rotation upon gas adsorption to accommodate more molecules yet maintain an approximately rigid unit cell[94]. Recently, a rare negative gas adsorption phenomenon was observed in a MOF and directly connected to the cooperative motion of many atoms across a large unit cell[95]. The crystal structure of a MOF at a given set of conditions is determined by trade-offs between intrahost, host-adsorbate, and adsorbate-adsorbate energies, as well as the mechanical stress induced by the pressure of the gas[96]. Deformation of the framework raises its energy in the absence of gas, but is often compensated for by more favorable host-adsorbate and/or adsorbate-adsorbate interactions.

Adsorption-induced deformation is a well-documented example of how adsorption can deviate from what is expected in perfect, rigid crystals. By contrast, adsorption in rigid lattices is known to be energetically driven only by host-adsorbate and adsorbate-adsorbate interactions. Logically, these interactions should be of a length scale associated with the adsorbate molecule. For example, water adsorbates may feel interactions on a long length scale because of water's unique hydrogen-bonding pattern[97], while noble gas adsorbates, which interact primarily through dispersion forces, feel no such effect and the length scale of their interactions is typically limited to the scale of their atomic radius. Within MOFs, unique adsorption mechanisms such as cooperative phenomena have previously been identified along with the system-specific interactions that drive them[98].

In this context, recent work by Cho *et al.* stands out in suggesting that adsorbate-adsorbate interactions across channel walls can drive adsorption in MOFs[99]. Cho *et al.* studied the behavior of different adsorbates in the IRMOF-74 series and presented *in situ* small-angle X-ray scattering (SAXS) data. The data for argon adsorption show evidence for the formation of extra argon adsorption domains in IRMOF-74-V-hex. The proposed extra argon adsorption domains take the form of a periodic superlattice, the dimensions of which extend beyond the size of a single channel (see Fig. 2.1, pink lines). The four corners of a proposed superlattice unit cell, shown explicitly in Fig. 2.2, represent channels with high argon density relative to the six adjacent channels. Cho *et al.* explain the superlattice by

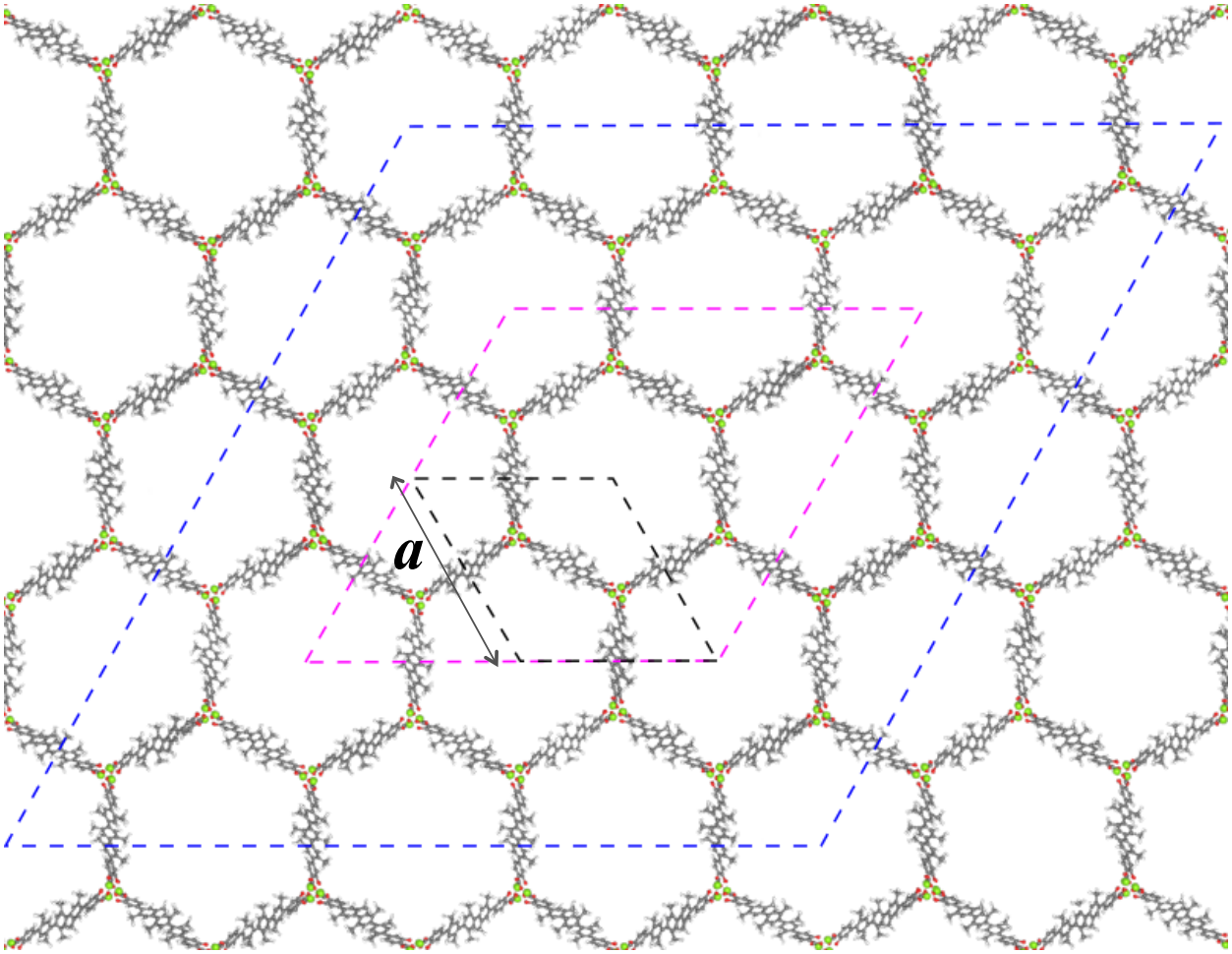

Figure 2.1: Different unit cells of the IRMOF-74-V lattice that are relevant to this study. The primitive unit cell used for DFT structure relaxation is marked in black, the simulation box used in *NPT* simulations is marked in blue and the superlattice dimension proposed by Cho *et al.* is marked in pink. Cho *et al.* propose that the corners of the superlattice represent regions of high loading. Unit cell parameter a is marked in black next to the primitive unit cell. Magnesium, oxygen, carbon and hydrogen atoms are marked in lime green, red, grey and white, respectively.

proposing a new mechanism in which cross-channel interactions of argon at 87 K stabilize the extra adsorption domains. Cho *et al.* further speculate that this is induced by a contraction of the unit cell.

The work by Cho *et al.* is the first report of an adsorption mechanism that involves cross-channel adsorbate interactions in a MOF. We therefore found it useful to use molecular simulation techniques to further quantify the importance of these cross-channel argon interactions. Unlike the experimental system, we can tune interactions in our simulations

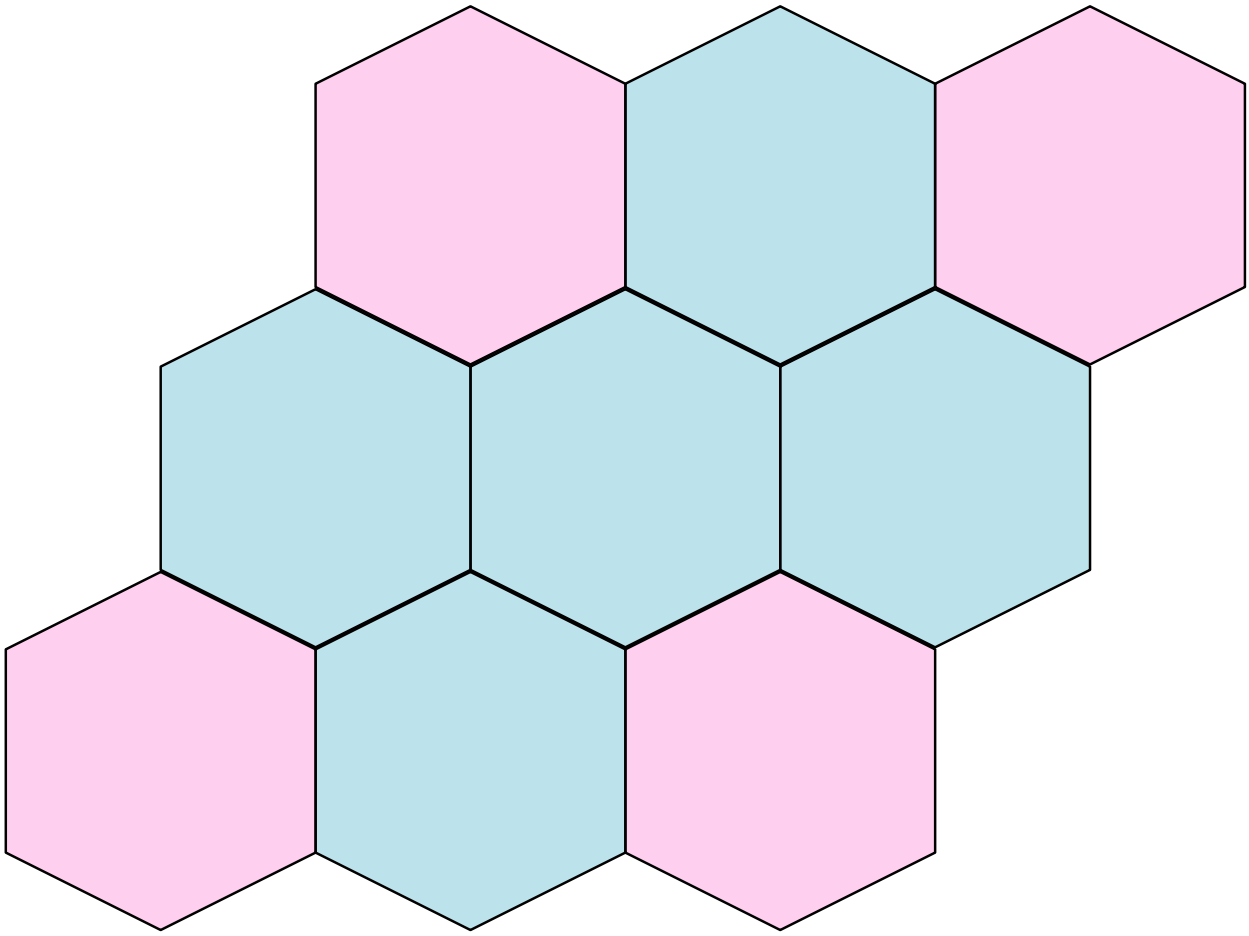

Figure 2.2: The shape of the argon superlattice proposed by Cho *et al.* The pink hexagons show proposed regions of high argon loading, and the blue regions show proposed regions of low argon loading. The hexagons have diameters of approximately 40 Å.

to directly compare a system in which argon-argon interactions are restricted to act only within a single channel with a system in which cross-channel interactions are allowed. Our simulations on argon adsorption in IRMOF-74-V, a MOF composed of Mg^{2+} atoms and expanded 2,5-dioxido-1,4-benzenedicarboxylate ($dobdc^{4-}$) ligands that include five aromatic rings[100], show, however, that cross-channel argon interactions have only a minor effect on the adsorption isotherm and do not lead to the argon superlattice described by Cho *et al.* We did discover that argon adsorption induces a deformation of the crystal lattice, and we demonstrate that this deformation can account for the signatures observed in the X-ray pattern measured by Cho *et al.*

2.2 Simulation Models

DFT calculations were necessary in order to generate charges and relax the crystal structures of IRMOF-74-V and IRMOF-74-V-hex, which were used for GCMC simulations and as starting structures for MD simulations throughout this work. All DFT calculations were performed with VASP[101] version 5.3.5, using projector augmented wave method (PAW) potentials[102, 103, 104]. We used a revised version of the van der Waals dispersion-corrected density functional (rev-vdW-DF2)[105] that was implemented in VASP by Klimeš *et al.*[106] using the algorithm of Román-Pérez *et al*[107].

We relaxed the experimental crystal structure via DFT calculations using a procedure that has been shown to lead to reasonable lattice constants and bond lengths in M-MOF-74[108]. The resulting relaxed unit cell was a starting point for all MC and MD simulations. Periodic DFT optimizations of the IRMOF-74-V and IRMOF-74-V-hex structures were done starting from respective 228-atom and 318-atom triclinic primitive unit cells obtained after removing solvent and reducing the symmetry of the experimental structure[100]. Integration over the Brillouin zone was carried out using Γ-point sampling. The plane-wave basis set was cutoff at 600 eV, and the wave function energy convergence criterion was set to 10^{-5}eV. The atomic positions were optimized until all forces were smaller than 0.05 eV/Å. Point charges were then assigned to the framework atoms using the REPEAT scheme[109] with the electrostatic potential generated from the structural relaxation.

We developed a flexible framework model inspired by the work of Greathouse *et al.*, which demonstrated that modeling metal-linker bonds classically using only non-bonded interactions can give a realistic description of the flexibility and coordination environment changes experienced by MOF-5 upon adsorption of water[110]. The use of non-bonded interactions to model metal-linker bonds allows us to study changes in the geometry at the coordination centers of IRMOF-74-V, while simultaneously avoiding the problem of modeling the complex metal-oxygen bonding environment with fixed harmonic potentials. The IRMOF-74-V superlattice used in all MD simulations consisted of 16 channels (4 channels x 4 channels).

In our model for IRMOF-74-V, bond, angle, dihedral and torsion parameters for linker molecules were taken from the Consistent Valence Force Field (CVFF)[84]. This choice was made because CVFF is known to accurately model small organic molecules and is consistent with the work of Greathouse *et al.* The metal model is adapted from CDM parameters developed by Duarte *et al.* which delocalize charge and specifically model M^{2+} ions in an octahedral coordination environment[58]. In the metal force field developed by Duarte *et al.*, the charge distribution on the central metal bead and six dummy beads sums up to a full 2+ charge on the metal ion. As we determined by using the REPEAT charge equilibration scheme, the magnesium atoms in IRMOF-74-V and IRMOF-74-V-hex do not have full 2+ charges. Therefore, to adapt the force field by Duarte *et al.* we scaled the charges on both the central metal bead and the six dummy beads accordingly so that the total charge on the metal complex would be equal to the REPEAT charge.

Lennard-Jones parameters taken from CVFF for linker atoms and from Duarte *et al.* for metal atoms were used with geometric mixing rules to compute non-bonded framework-

Table 2.1: IRMOF-74-V unit cell parameters predicted by DFT and the force field at 0 K.

Parameter ($p3-$plane group)	DFT	Force Field	% Difference
a or b (Å)	38.4122	38.2597	0.657%
c (Å)	6.8185	6.7737	-0.397%
α (°)	119.653	119.640	-0.011%
β or γ (°)	93.3921	93.3799	-0.013

framework interactions. Implementation of this force field and unit cell relaxation led to good agreement with the DFT energy-minimized structure (less than 1% difference of any unit cell parameter, shown in (Table 2.1).

For our models of argon-argon and argon-MOF interactions, Lennard-Jones parameters for argon were taken from work by Brown *et al*[111]. Non-bonded interactions between argon, linker and metal atoms were calculated by using geometric mixing rules with Lennard-Jones parameters from Brown *et al.*[111], CVFF[84] and Duarte *et al.*[58], respectively, as was similarly done by Macedonia *et al.* to calculate interactions of argon with zeolites[112]. Lennard-Jones interactions and short-range (real space) coulombic interactions were truncated at 10 Å, and Ewald summations were used to calculate long-range coulombic interactions.

Ab initio derived parameters were used for simulation of CO_2 in IRMOF-74-V. Buckingham parameters modeling the interactions of CO_2 with the framework were adapted directly from the work of Mercado *et al.*[25], which was made for use with the original dobdc^{4-} ligand and containing only one aromatic ring. The additional aromatic atoms were treated in the same way that Mercado *et al.* treated the dobpdc^{4-} = 4,4-dioxidobiphenyl-3,3-dicarboxylate ligand containing two aromatic rings: additional aromatic carbons were classified based on whether or not they were bound to an aromatic hydrogen. The TraPPE force field was used to model N_2-N_2 interactions[113] and the EPM2 force field was used to model CO_2-CO_2 interactions[114]. Non-bonded interactions between N_2 and framework atoms were calculated using Lorenz-Berthelot mixing rules with the TraPPE force field for N_2 and the CVFF and Duarte *et al.* force field described above for the framework.

Simulations of argon adsorbing in IRMOF-74-III and IRMOF-74-VII used the same force field as argon adsorbing in IRMOF-74-V, but we started with DFT-optimized lattices and atomic charges available in literature[37].

2.3 Adsorption Isotherms

We used GCMC simulations to compute argon adsorption isotherms in IRMOF-74-V. The DFT optimized unit cells were used to simulate adsorption isotherms in the standard lattice discussed below. In these simulations we used as trial moves insertions at a random argon position, deletions, and translations with equal probability using the intermolecular potentials described in the Simulation Models section. We used the ideal gas law to relate the chemical potential μ_{ig} of argon to the pressure in the experiment. The use of the ideal

gas law allows us to simplify the GCMC acceptance rule such that the de Broglie thermal wavelength disappears. For an ideal gas,

$$\beta\mu_{ig} = \ln \Lambda^3 \frac{N}{V} = \ln \Lambda^3 \beta \mathrm{P}_{ig} \tag{2.1}$$

$$\mu_{ig} = \frac{1}{\beta} \ln \Lambda^3 + \frac{1}{\beta} \ln \beta \mathrm{P}_{ig} \tag{2.2}$$

Substituting μ_{ig} from Eq. 2.2 into our acceptance ratio formula for insertion of an adsorbate molecule, we can begin to simplify:

$$\frac{\mathrm{acc}(N \to N+1)}{\mathrm{acc}(N+1 \to N)} = \frac{\mathrm{V}}{(N+1)\Lambda^3} \exp^{(\ln \Lambda^3 + \ln \beta \mathrm{P}_{ig})} \exp^{-\beta(U(s^{N+1}) - U(s^N))} \tag{2.3}$$

$$\frac{\mathrm{acc}(N \to N+1)}{\mathrm{acc}(N+1 \to N)} = \frac{\mathrm{V}\beta \mathrm{P}_{ig}}{(N+1)} \exp^{-\beta(U(s^{N+1}) - U(s^N))} \tag{2.4}$$

Following a similar set of steps for the removal of an adsorbate molecule, we can show the following:

$$\frac{\mathrm{acc}(N \to N-1)}{\mathrm{acc}(N-1 \to N)} = \frac{N}{\mathrm{V}\beta \mathrm{P}_{ig}} \exp^{-\beta(U(s^{N-1}) - U(s^N))} \tag{2.5}$$

Thus, the Metropolis acceptance rules become:

$$\mathrm{acc}(N \to N+1) = \min(1, \frac{\mathrm{V}\beta \mathrm{P}_{ig}}{(N+1)} \exp^{-\beta(U(s^{N+1}) - U(s^N))}) \tag{2.6}$$

and

$$\mathrm{acc}(N \to N-1) = \min(1, \frac{N}{\mathrm{V}\beta \mathrm{P}_{ig}} \exp^{-\beta(U(s^{N-1}) - U(s^N))}) \tag{2.7}$$

Starting at the lowest ideal gas pressure, we simulated the argon adsorption successively by initiating the simulation with the adsorbate positions stored at the end of the previous simulation. Hysteresis is monitored by performing these GCMC calculations both with increasing and decreasing pressures. We utilized 75,000 equilibrium cycles and 30,000 sampling cycles, where a cycle is defined as $\max(20, n)$ Markov chain transition proposals, where n is the number of adsorbates currently in the system. We replicated the IRMOF-74-V crystal structure three times along the axis of the metal helices to prevent atoms from interacting with their own image.

In Fig. 2.3a we compare our isotherms with the isotherm measured by Cho *et al.* The snapshots in Fig. 2.3b illustrate that argon adsorbs in layers on channel walls: at 0.001 bar, there is a single layer of argon atoms in the channel, followed by a second layer at 0.10 bar.

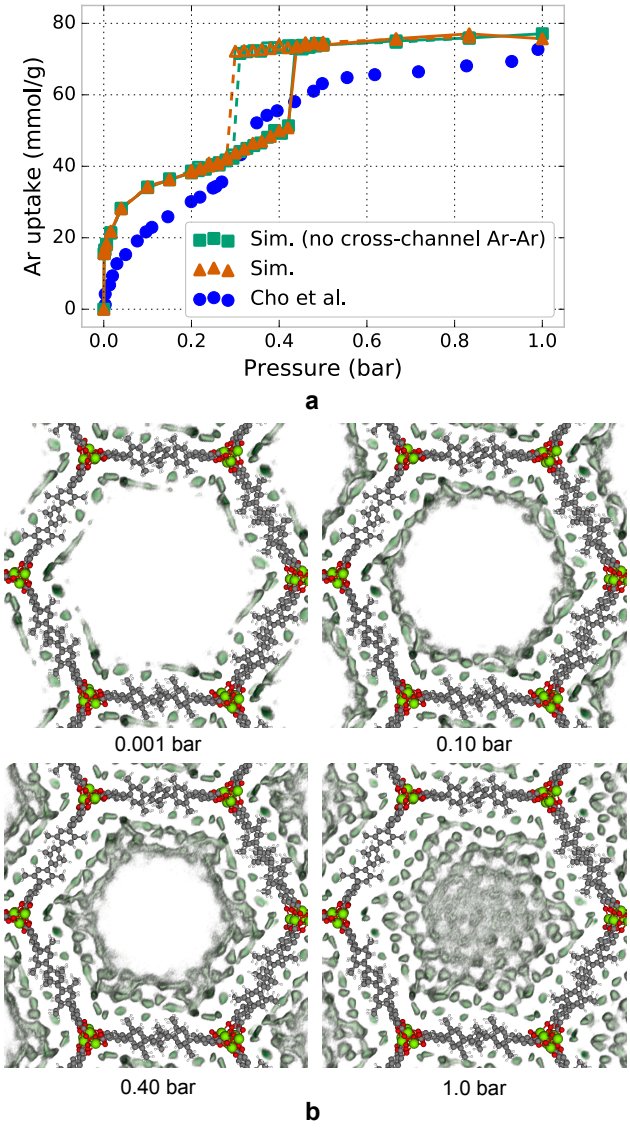

Figure 2.3: Characteristics of argon adsorption in a rigid lattice model. Simulated and experimental argon adsorption isotherms in IRMOF-74-V at 87 K are shown in (a) and snapshots of argon loading at select pressures are shown in (b). In the snapshots, argon density is colored in dark green and the rigid lattice model is also shown. The teal curve in (a) is a simulated argon isotherm. The orange curve in (a) is a simulated argon isotherm where argon-argon interactions across channels are artificially turned off, i.e., argon adsorbates interact with each other within the same hexagonal channel, but two argon atoms in different channels do not interact. Adsorption and desorption portions of the simulated isotherms are marked with closed and open markers, respectively. The blue points in (a) are the experimental isotherm measured by Cho *et al.*

The pore completely fills a little beyond 0.40 bar. A comparison of the snapshots in Fig. 2.3b and the isotherm in Fig. 2.3a shows that the jump in the isotherm occurs exactly before the pores flood with argon. The jump in the isotherms indicates capillary condensation in the pores[115], which have an approximate diameter of 40 Å. The hysteresis that we observe upon desorption is further evidence for capillary condensation and is a well known phenomenon in structures containing mesopores[116]. Our simulations are in good qualitative agreement with the experimentally measured isotherm, capturing the inflection point in argon uptake in the range of 35 to 45 kPa. Cho *et al.* also reported hysteresis in their experimental isotherm but over a smaller pressure window. The large simulated Henry coefficient, apparent in the overestimation of loading at low pressures, can be attributed to inaccuracies in the force field description of noble gas-MOF interactions, and is in similar agreement compared with other studies on noble gas adsorption in MOFs[117]. At intermediate and high loadings, the quantitative differences between the experimental and simulated isotherms may be related to the fact that we use a rigid lattice model for all simulations and assume a perfect crystal structure, which is experimentally impossible to synthesize.

The shape of the argon adsorption isotherm was presented by Cho *et al.* as a piece of evidence in support of cross-channel interaction induced argon ordering as the inflection point in the isotherm was attributed to the formation of extra adsorption domains. To study the effect of cross-channel interactions we compared GCMC simulations of a system in which argon can interact across channels with a system in which we (artificially) restricted argon-argon interactions to contribute only if the argon atoms are in the same channel. This was accomplished by determining whether or not each pair of argon atoms within the Lennard-Jones cutoff distance were in the same channel, and only including contributions to the energy used for the GCMC acceptance rules given in Eq. 2.6 and Eq. 2.7 if both argons were in the same channel. The algorithm used for this is visually explained in Fig. 2.4. Based on our knowledge of the positions of the vertices (metal helices), shown as red circles in Fig. 2.4a, we are able to define the boundaries of each channel. If two argon atoms fulfill the requirements described in the Fig. 2.4 caption for all boundaries of a given channel, their interaction potential was included in the system energy U of Eq. 2.6 and Eq. 2.7. The adsorption mechanism proposed by Cho *et al.* suggests that by artificially turning off interactions between argon atoms that are not in the same channel, we should obtain a qualitatively different adsorption behavior. A comparison of the two simulated isotherms in Fig. 2.3a reveals that cross-channel argon-argon interactions have little to no effect on the isotherm. Argon atoms in different channels are too far apart to interact significantly.

2.4 Lattice Deformation

An important difference between our GCMC simulations for which isotherms are presented in Fig. 2.3a and experiments is that we assume a rigid crystal structure, while experimental data shows that the unit cell parameter a, shown in Fig. 2.1, does change upon adsorption. To study the effect of argon adsorption on the crystal structure of IRMOF-74-V, we use

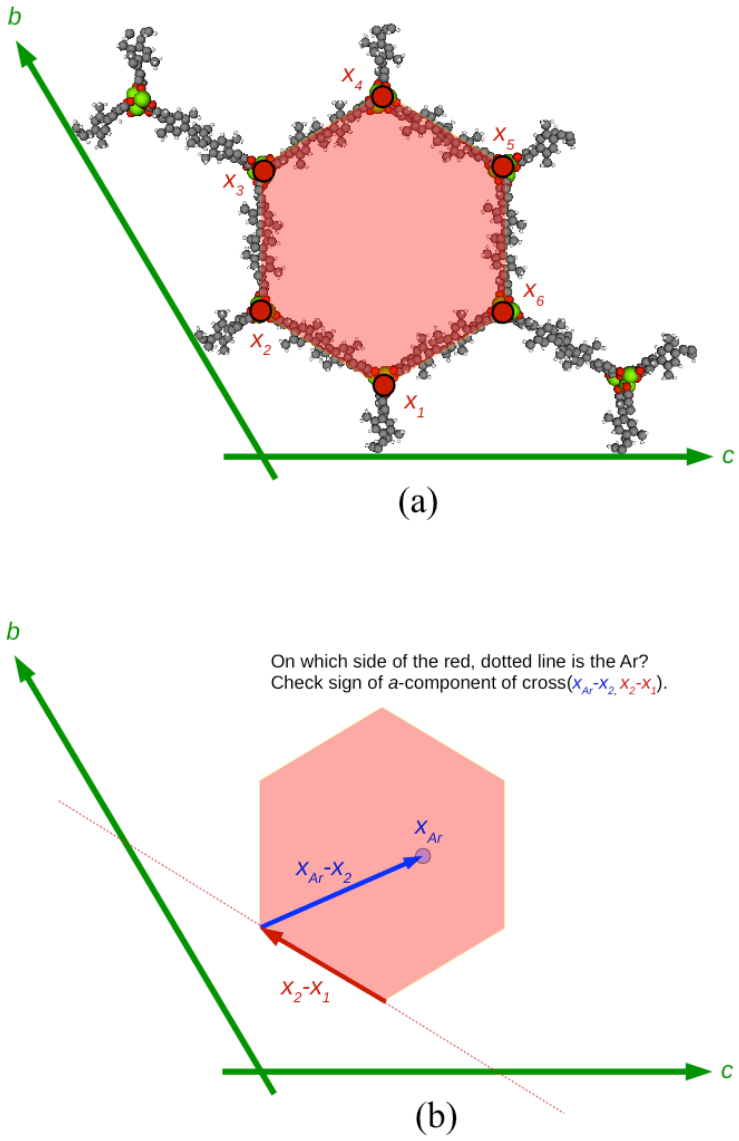

Figure 2.4: Classifying an argon as belonging or not belonging to the home channel. (a) The home channel is defined by the hexagon in the $b-c$ plane shown filled in red. The vertices x_i are labeled. (b) Consider our algorithm for $i = 2$. Shown are the two vectors of interest, $x_2 - x_1$ and $x_{Ar} - x_2$ in red and blue, respectively. The line that passes through x_1 and x_2 is shown as the red, dotted line. If the argon belongs to the home channel, then x_{Ar} lies above this line. To determine whether x_{Ar} is above or below the line, we check the sign of the $a-$component of the cross product of $x_{Ar} - x_2$ and $x_2 - x_1$ after we extend them to three dimensions by defining the a-component to be zero.

flexible lattice simulations. In these simulations, we use for each channel a fixed loading given by the pressure of the simulated isotherms (Fig. 2.3a) and monitor the change of the IRMOF-74-V structure in terms of the lattice parameter as a function of pressure.

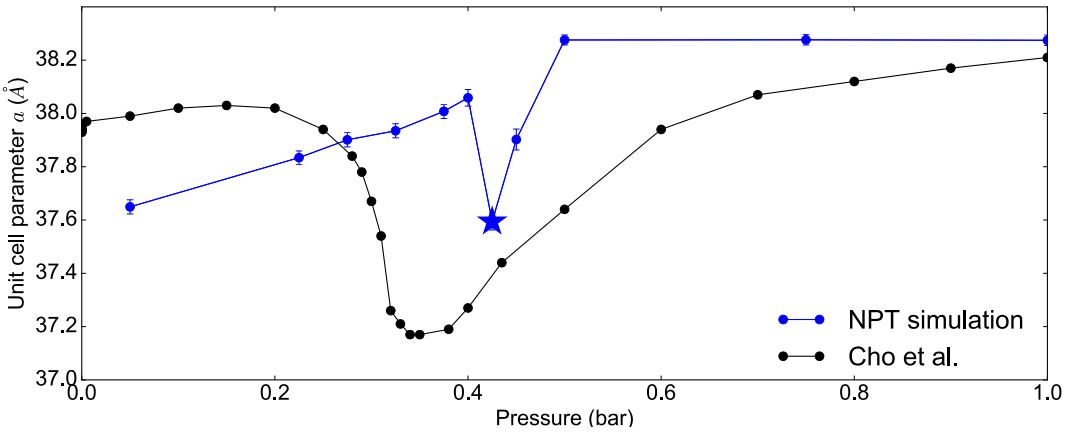

Figure 2.5: Unit cell parameter a of IRMOF-74-V as a function of pressure. Unit cell parameter a is denoted as a double-headed black arrow next to the primitive unit cell in Fig. 2.1. NPT simulation data is shown in blue and the experimental data of Cho *et al.* is shown in black. Simulation data points are averages and error bars show the standard deviation. The loadings imposed in the *NPT* simulation are commensurate with the simulated standard lattice adsorption at that pressure. Stars represent conditions at which lattice deformation was observed, as shown in Fig. 2.6.

Changes in the lattice of IRMOF-74-V as a function of loading were simulated using MD simulations in the *NVT* and *NPT* ensembles using the LAMMPS molecular software package[118]. Using the observations of Cho *et al.* as a guiding reference, we first slowly decreased the unit cell parameter a of IRMOF-74-V loaded with argon by 90% while simulating the lattice in the *NVT* ensemble. The scaled lattice was then allowed to relax to its equilibrium unit cell parameter a in the *NPT* ensemble. Each lattice was simulated for a total of 2.5 nanoseconds with a timestep of one femtosecond using a Nosé-Hoover thermostat and a Parrinello-Rahman barostat.

Fig. 2.5 shows that our simulations agree well with the experimentally observed behavior in the lattice parameter. Similar to the experiments, we observe at low pressures that the crystal swells when the pressure and loading are increased. At intermediate pressures, however, we see a dip in the lattice parameter, while at high pressures the crystal swells again. Upon further inspection of the lattice at 0.425 bar, we discover that the unit cell parameter a does not only shrink but the lattice also deforms (see Fig. 2.6) such that it is no longer represented by the crystal structure shown in Fig. 2.1.

The standard lattice of the IRMOF-74 series is composed of channels in the shape of regular hexagons. Four distinct types of channels exist in the deformed lattice and are shown

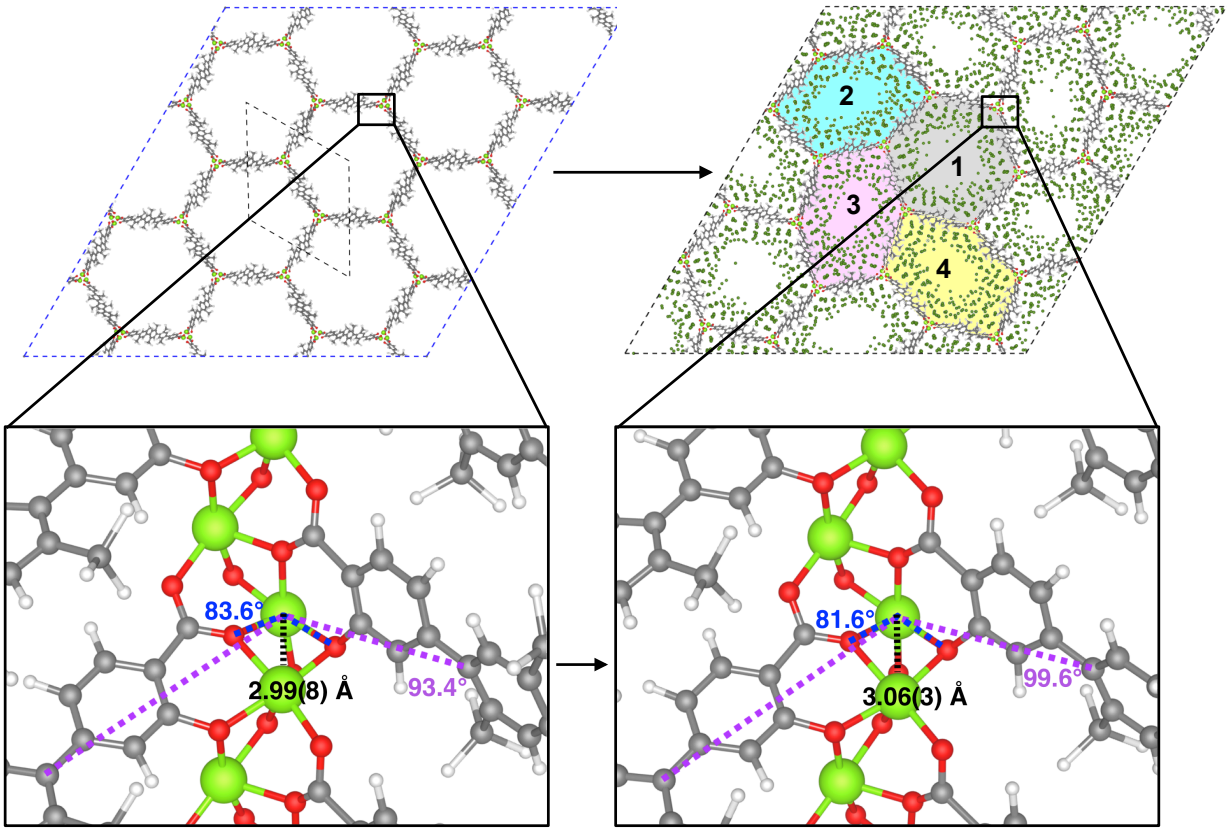

Figure 2.6: Representations of lattice deformation. Black dotted lines represent the unit cell of standard and deformed crystal lattices. The deformed lattice shows Channel 1 in grey, Channel 2 in blue, Channel 3 in pink and Channel 4 in yellow. The views of of a standard right-handed metal helix from inside a standard and irregular channel are also shown. Magnesium, oxygen, carbon, hydrogen and argon atoms are marked in lime green, red, grey, white and dark green, respectively. The distance between metal atoms is larger in the deformed helix, indicating that the helix becomes wider. Angles between atoms on neighboring linkers change accordingly.

in Fig. 2.6. The central Channel 1 resembles a channel in the standard lattice. Channels 2, 3 and 4 are irregular hexagons that have a smaller volume than Channel 1 and form a spiral shape around the central, regular channel. Two irregular channels of the same type are always found directly across the regular channel from each other. This pattern imposes a geometric constraint that causes the observed deformation to be coherent and crystalline. If one channel deforms, the lattice must deform as well to prevent massive strain.

The observed deformation is associated with a subtle change in geometry of some metal helices. Fig. 2.6 shows two views of right-handed metal helices from the interior of a regular channel in a standard lattice and an irregular channel (Channel 2, 3 or 4) in a deformed lattice. Metal helices are deformed if they join Channel 1 hexagons with two irregular channels. The deformed metal helix is slightly wider than the standard metal helix, as shown by the larger distance between metals. To maintain an appropriately square pyramidal coordination geometry, metal-bound oxygen atoms shift their positions. This rearrangement of atoms is propagated along the flexible linkers and causes a change in the vertex angle of the irregular channels.

In the GCMC simulations that we have already presented, we have used only a rigid standard IRMOF-74-V lattice. It is therefore important to determine whether a rigid deformed lattice can lead to a qualitatively different isotherm. To accomplish this we investigated the adsorption properties of Channels 1, 2, 3 and 4 in the deformed lattice separately. Framework coordinates from a snapshot of an MD simulation were used as a host material structure to make adsorption isotherms of a deformed lattice. Fig. 2.7a shows that while the argon uptake in all four channels is similar at low pressures, Channels 2, 3 and 4 all adsorb less argon than Channel 1 at high pressures. The difference in loading at high pressures is easily rationalized by the difference in volume between channels.

The individual channel isotherms demonstrate that Channels 2, 3 and 4 all experience a jump in loading at a lower pressure than Channel 1. The difference in pore filling pressures across the channels is in agreement with the expectation that capillary condensation occurs at lower pressures in smaller channels[119]. Therefore, in the very narrow pressure window between 0.40 and 0.425 bar, the smaller deformed channels actually adsorb a higher density of argon than Channel 1. A comparison of Fig. 2.7 with Fig. 2.5 shows that this narrow pressure window corresponds with the pressure at which the deformed lattice was observed. The composite deformed lattice isotherm in Fig. 2.7b was made by averaging together the four individual channel isotherms shown in Fig. 2.7a. The effect of lattice deformation can be seen by comparing the deformed composite isotherm to the Channel 1 isotherm, which resembles a channel in a standard lattice. The Channel 1 isotherm shown in Fig. 2.7 and rigid lattice isotherm shown in Fig. 2.3a are different. The rigid lattice used in Fig. 2.3a is the DFT-optimized structure, whereas the deformed lattice and individual channel structures result from molecular simulations and are governed by the force field, which means that the two structures vary and have slightly different sizes and linker orientations. For this reason, Channel 1 should be compared with the deformed channels and lattice rather than the DFT-optimized structure. In the pressure range where the deformed lattice was observed (near 0.425 bar), the effect of lattice deformation is to cause a more smooth increase in loading as

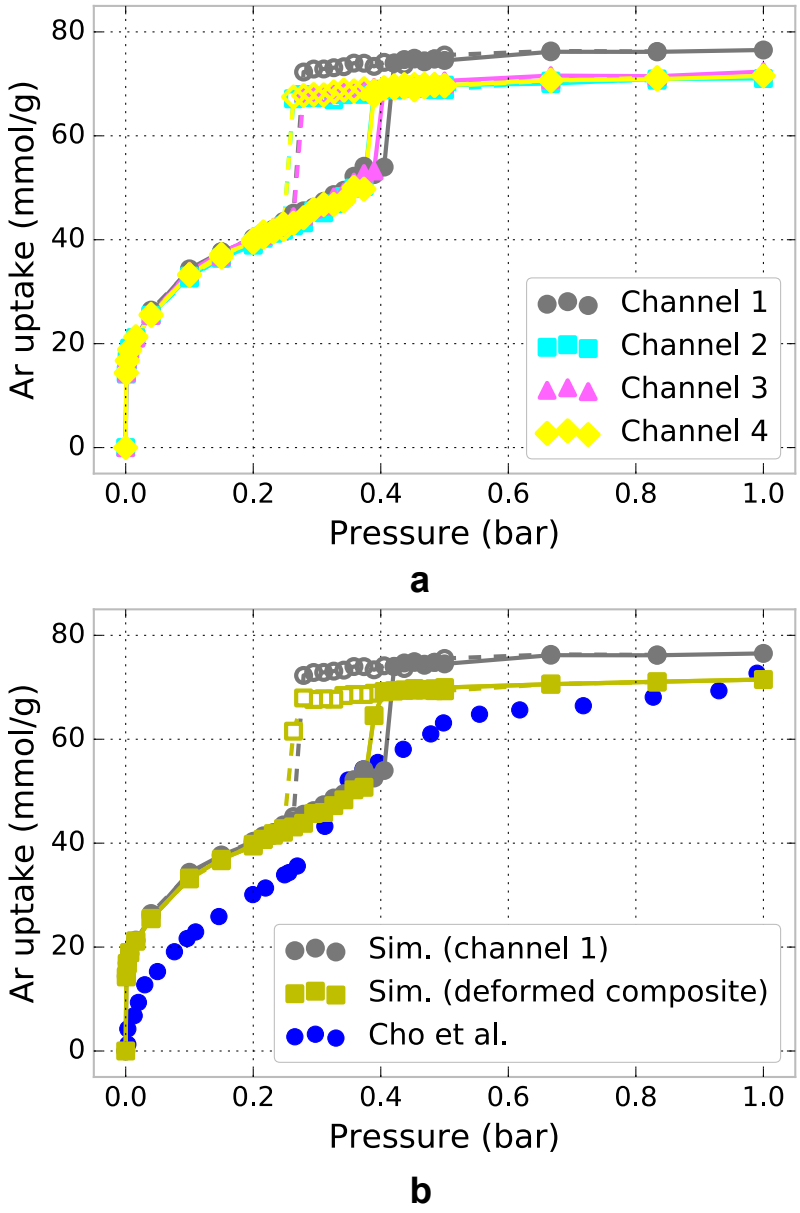

Figure 2.7: Argon adsorption isotherms in the deformed lattice. Adsorption isotherms for each of the four channels of the deformed lattice, as shown in Fig. 2.6, are shown in (a) and match the color code shown in Fig. 2.6. The yellow curve in (b) is the deformed lattice composite isotherm obtained by averaging together the isotherms for the four different channels. Adsorption and desorption portions of the simulated isotherms are marked with closed and open markers, respectively. The blue points in (b) are the experimental isotherm measured by Cho *et al.*

each of the channels will fill at a slightly different pressure in the deformed lattice.

2.5 X-ray Spectra

In our simulations, we find no evidence to support the cross-channel interaction mechanism or adsorbate superlattice proposed by Cho *et al.* At this point, it is important to note that Cho *et al.* assumed that for all pressures, the IRMOF-74 lattice maintains its crystal structure and does not deform. Indeed, it was reasonable to make this assumption because several previous studies of IRMOF-74 have suggested that the metal-oxygen nodes are relatively rigid[120, 121]. It is therefore important to investigate the impact of the observed deformation on the X-ray pattern of the system. We compare the X-ray signature associated with our deformed lattice with the experimental X-ray data.

Powder X-ray diffraction (PXRD) patterns of the MOF lattice and small-angle X-ray scattering (SAXS) profiles of adsorbing argon are calculated directly from atomic coordinates[122, 123].

According to Bragg's Law, peaks of scattered intensity appear when the pathlength difference between scattered waves is an integer multiple of the X-ray wavelength:

$$n\lambda = 2d\sin(\theta) \tag{2.8}$$

where θ is the equivalent angle of incidence and scattering, and $2d\sin(\theta)$ is the pathlength difference. The scattering vector q is defined as:

$$q = \frac{4\pi\sin(\theta)}{\lambda} \tag{2.9}$$

Substituting the variables in Eq. 2.8 into Eq. 2.9 and solving for q yields:

$$q = \frac{2\pi n}{d} \tag{2.10}$$

where d is interplanar spacing. The q-axis of all subsequent X-ray plots is given by Eq. 2.9 and Eq. 2.10. The Debye equation is used to calculate the simulated SAXS profile:

$$I(q) = \sum_i \sum_j f_i f_j \frac{\sin(qr_{ij})}{qr_{ij}} \tag{2.11}$$

where r_{ij} is the distance vector between a pair of atoms i, j, and f_i is the form factor of atom i.

The experimental samples used by Cho *et al.* were powder and therefore simulated PXRD peaks can be compared to peaks in the experimental SAXS profile. For the simulated SAXS profiles shown in Fig. 2.8b, argon positions are extracted from both a deformed lattice with a loading commensurate with the adsorption isotherm at 0.425 bar and a standard lattice artificially loaded with a number of atoms corresponding to 0.425 bar.

The simulated deformed X-ray pattern shown in Fig. 2.8a is intriguingly similar to the experimental SAXS profiles. Cho *et al.* observed the appearance of peaks at $q = 0.25$ Å^{-1} and $q = 0.42$ Å^{-1} during argon adsorption in one of the IRMOF-74 analogs studied, IRMOF-74-V-hex, at intermediate pressure and loading conditions. Cho *et al.* also observed broad peaks at $q = 0.10$ Å^{-1} for all IRMOF-74 analogs studied. Experimentally, peaks associated with the standard lattice did not disappear in any of the IRMOF-74 analogs studied, a fact that was specifically interpreted by Cho *et al.* to mean that the lattice was not deforming[99]. As we show in Fig. 2.8a, deformation of the IRMOF-74-V lattice produces new X-ray peaks at all of the q-values that were experimentally noted without causing the standard lattice peaks to disappear. Although Cho *et al.* attributed the additional peaks in their SAXS profiles to long-range ordering of argon atoms, we believe that framework deformation is a more likely physical origin of this signal.

As is observed in the experimental data, the standard lattice peaks are preserved in the deformed lattice X-ray pattern, but not because the lattice maintains its structure. The standard lattice of IRMOF-74-V exhbits peaks in the X-ray pattern at q-values near 0.20 Å^{-1} and 0.33 Å^{-1}, marked in red and blue in Fig. 2.8a. These peaks are associated with two independent crystallographic spacings, the $hk = 10$ and 11 Miller face spacings, marked in red and blue respectively in Fig. 2.8c. The deformed lattice X-ray pattern exhibits peaks of similar magnitude in similar positions as the standard lattice, also marked in red and blue in Fig. 2.8a. The standard peaks appear in the deformed X-ray pattern because the deformed lattice includes crystallographic spacings that are geometrically similar to those in the standard lattice, the $hk = 42$ and 72 Miller face spacings shown in red and blue in Fig. 2.8d. The peaks in the deformed X-ray pattern that are related to the standard peaks are shifted slightly to the right. This is a consquence of the overall decrease in unit cell parameter. The apparently larger shift associated with the $hk = 11$ compared to the $hk = 10$ Miller face spacing does not indicate a larger change in interplanar spacing. Rather, the q-value at which an interplanar spacing appears is more sensitive at smaller spacings.

New peaks observed by Cho *et al.* can be explained by the increased number of crystallographic spacings in the deformed lattice. The peak observed experimentally at $q = 0.25$ Å^{-1} corresponds to the $hk = 51$ Miller face spacing in the deformed lattice, marked in purple in Fig. 2.8d. The peak observed experimentally at $q = 0.42$ Å^{-1} corresponds to the $hk = 81$ Miller face spacings in the deformed lattice, marked in orange in Fig. 2.8d. These two peaks are related to expansion and compression of the $hk = 11$ Miller face spacing of the standard lattice, respectively. The broad peak experimentally observed at $q = 0.10$ Å^{-1} appears at the same q-value as the peak associated with the $hk = 21$ Miller face spacing in the deformed lattice, marked in maroon in Fig. 2.8d. The $hk = 21$ Miller face spacing in the deformed lattice is unique because it spans the length of more than one hexagon.

Simulated SAXS profiles that account only for argon light scattering are shown in Fig. 2.8b. This figure demonstrates that argon does not organize differently across channels as a result of deformation. In both cases, peaks appear in the SAXS profiles at q-values that correspond to peaks in the powder X-ray diffraction (PXRD) pattern of the respective lattice. This feature is due to the fact that argon is adsorbing on the walls of the channel, as shown

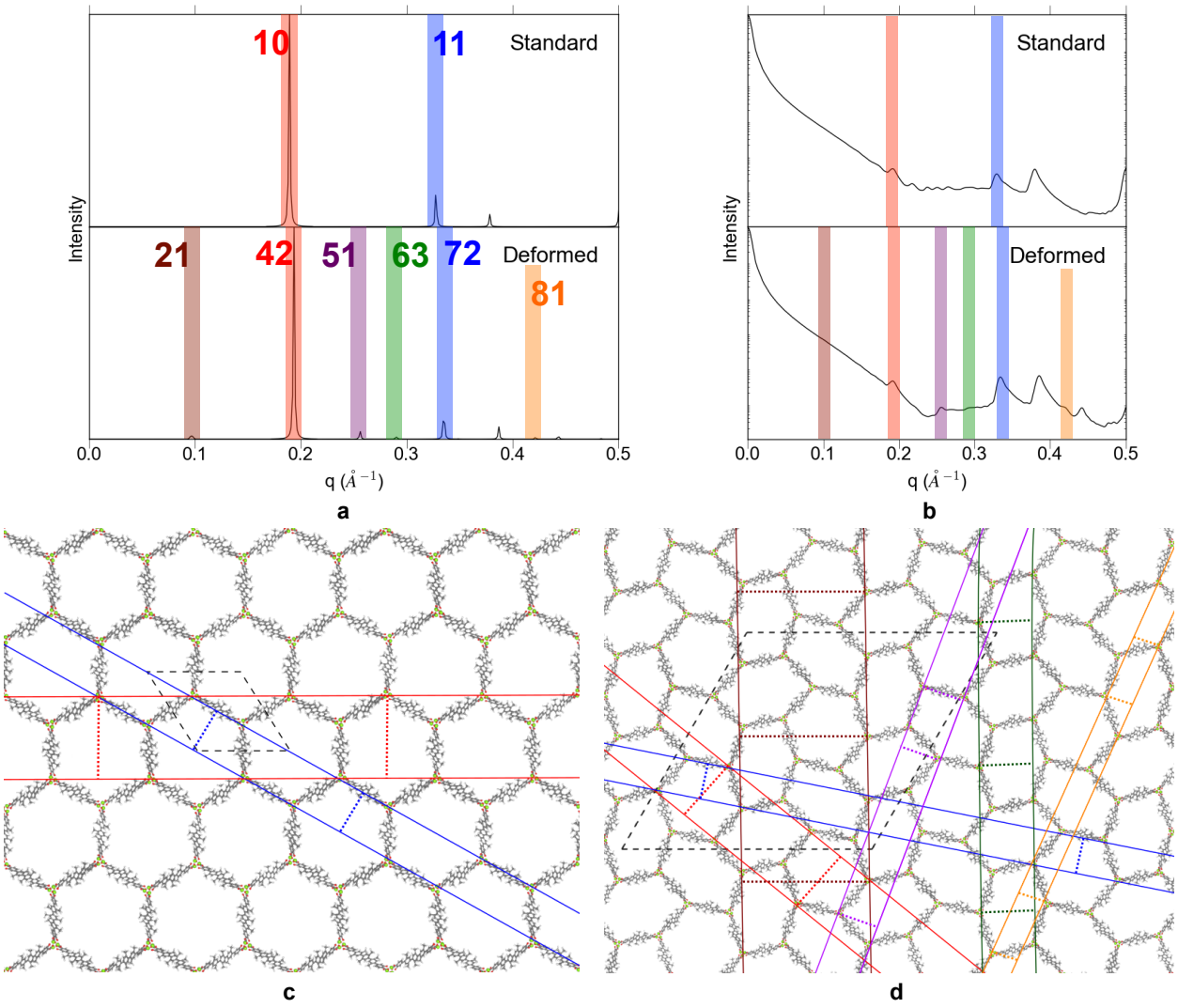

Figure 2.8: Simulated X-ray spectra and associated standard and deformed IRMOF-74-V lattices. X-ray patterns for the MOF are shown in (a) and SAXS profiles for the argon are shown in (b). In the X-ray patterns, the standard lattice corresponds to vacuum and the deformed lattice to a pressure of 0.425 bar and loading commensurate with the adsorption isotherm. In the SAXS profiles, the deformed lattice and loading correspond to a pressure of 0.425 bar, but a standard lattice is artificially given a loading corresponding to 0.425 bar. Peaks in the patterns are marked with a color-code that corresponds to the crystallographic spacings shown in (c) and (d), which are labeled snaphots of standard (c) and deformed (d) lattices. Red and blue lines in (c) represent hk = 10 and 11 Miller faces, respectively. The red, blue, orange, green, purple and maroon lines in (d) represent the hk = 42, 72, 81, 63, 51, and 21 Miller faces, respectively.

in Fig. 2.3b, and the SAXS profile peaks are a reflection of the bounding lattice.

There are some discrepancies between the X-ray peaks shown in Fig. 2.8a and the SAXS profile measured by Cho *et al.*, but these differences can be explained. The standard peaks in the simulated X-ray pattern associated with the $hk = 10$ and $hk = 11$ Miller face spacings do not shift as noticeably in the work by Cho *et al.* We attribute this to finite-size effects in our simulation, as the necessarily small size of our simulation superlattice (4 channels x 4 channels) imposes a uniform deformation on opposite sides of the simulation box via periodic boundary conditions. A larger superlattice approaching the size of the experimentally-realized system would experience less perfect and perhaps less widespread deformation, reducing the overall effect on interplanar spacing. In addition, the small peak we observe at $q = 0.28$ Å^{-1}, associated with the $hk = 63$ Miller face spacing in the deformed lattice, is not noted by Cho *et al.*, but we believe this peak may be indistinguishable from the much more intense standard peak near $q = 0.33$ Å^{-1} in the experimental SAXS data[99].

2.6 Additional Adsorbates and Analogs

The arguments we have presented suggest that the observed deformation is not limited to argon adsorbing in IRMOF-74-V, but can also occur in other adsorbate-framework systems within the IRMOF-74 series. In Fig. 2.9, we show that the same deformation indeed can occur with other adsorbates and IRMOF-74 analogs. Fig. 2.9 demonstrates that the adsorbate identity affects the extent of deformation.

We investigated lattice deformation in the aformentioned additional systems by imposing a dip in the unit cell parameter rather than relying on *NPT* simulations. Fig. 2.9a and Fig. 2.9b show deformed lattices of IRMOF-74-V loaded with N_2 and CO_2 gas, respectively, and Fig. 2.9c shows a deformed lattice of IRMOF-74-V-hex loaded with argon. These systems were chosen because they were also studied by Cho *et al.* We decreased the unit cell parameter of IRMOF-74-V and IRMOF-74-V-hex by 90%, and then increased the unit cell parameter again to the experimentally observed minimum value, at which point we let the system equilibrate in the *NVT* ensemble. Throughout the simulation, the lattices were loaded with the number of adsorbates commensurate with the isotherms measured by Cho *et al.* N_2, CO_2 and argon adsorbate systems were simulated at 77 K, 194 K and 87 K, respectively.

To assess the extent of deformation induced in IRMOF-74-V by the three adsorbates studied (Ar, N_2 and CO_2) we collected statistics on the vertex angles of each of the hexagonal channels in the deformed lattices. Fig. 2.10 shows the differences between the vertex angle distributions of the lattices deformed by Ar, N_2 and CO_2 and the standard lattices at their respective temperature, where adsorbate identity and temperature are shown in the upper right quadrant of each graph. By comparison of the solid lines in the three panels, it is apparent that the range of the vertex angle distribution in the standard lattice does not change significantly over the temperature range considered in this study.

In the Ar-deformed lattice, the new vertex angles sampled appear clearly as new peaks, and the total distribution spans the range from 100° to 140°. The lattices deformed by the

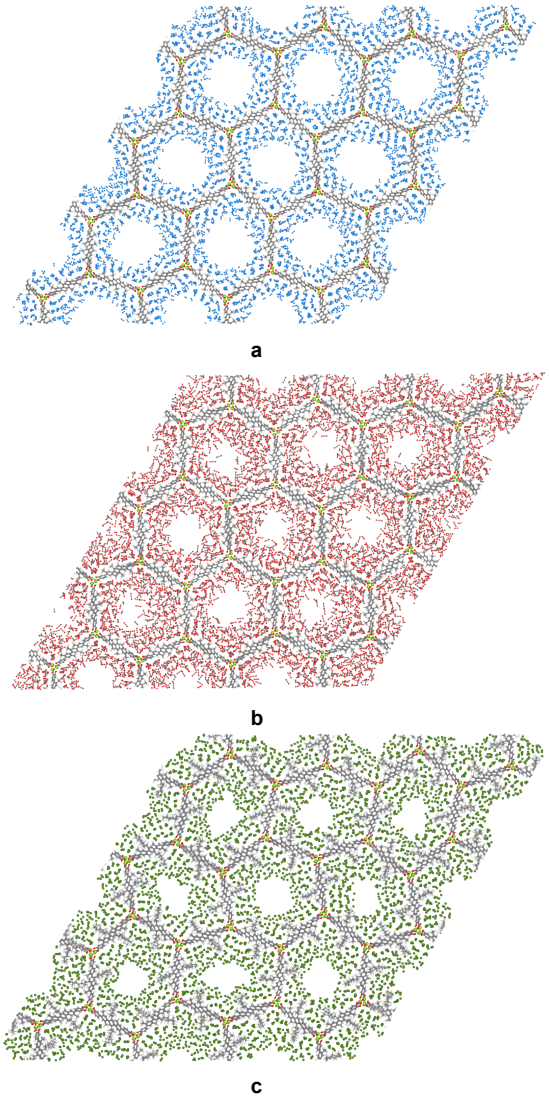

Figure 2.9: Snapshots of deformed lattices of other adsorbate-framework systems. IRMOF-74-V lattices loaded with N_2 and CO_2 are shown in (a) and (b), respectively, and an IRMOF-74-V-hex lattice loaded with argon is shown in (c). We accessed deformation in these systems by imposing the minimum unit cell parameter a reported by Cho *et al.* during the adsorption process, and by loading the lattice with the commensurate number of adsorbate molecules. The systems were then simulated in the NVT ensemble at temperatures corresponding to the measurements by Cho *et al.* (77 K for N_2, 194 K for CO_2 and 87 K for argon). Nitrogen, carbon, oxygen and argon atoms are marked in blue, grey, red and dark green, respectively.

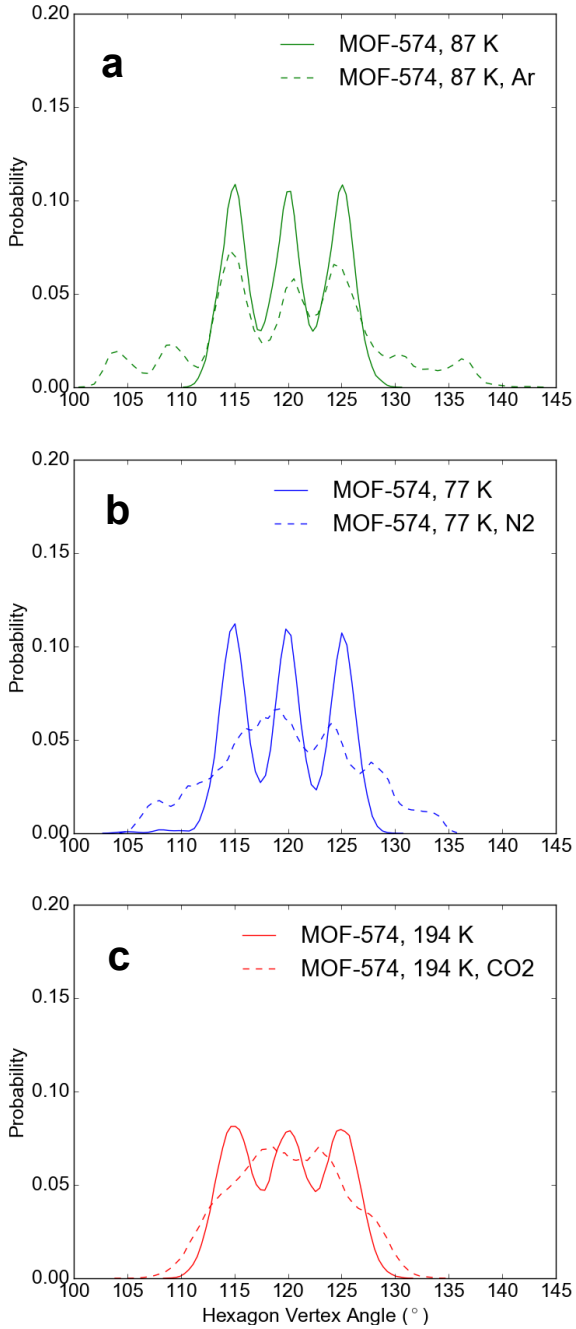

Figure 2.10: Hexagon vertex angle distributions in standard and deformed IRMOF-74-V lattices. The differences between the vertex angle distributions (hexagonal channels) of the lattices deformed by Ar, N_2 and CO_2 and the standard lattices at their respective temperature. The range of the deformed distributions shows the following order of extent of deformation (from most to least): Ar at 87 K > N_2 at 77 K > CO_2 at 194 K.

more complex adsorbates (N_2 and CO_2) fluctuate more and their peaks are more difficult to distinguish, especially in the case of CO2. However, a comparison of the range of these three distributions yields information about the extent of deformation. The N_2 distribution spans a smaller range than the argon distribution, from 105° to 135°, while the CO2 distribution spans an even smaller range from approximately 106° to 133°. From this we infer that from most to least deformation, the order of the systems studied is as follows: Ar at 87 K > N_2 at 77 K > CO_2 at 194 K.

We also modeled argon adsorbing in IRMOF-74-III and IRMOF-74-VII, but we did not access deformation in these structures when performing simulations with the same methodology carried out for IRMOF-74-V. This suggests a sensitive pore size dependence, wherein argon stabilizes deformation more in pores that are on the scale of 40 Å compared to pores that are 15 Å smaller or larger.

2.7 Conclusion

Using classical simulations, we predicted that the IRMOF-74 series can undergo an adsorbate-induced deformation. The deformed framework reproduces key features that were experimentally observed during argon adsorption by Cho *et al.*, namely changes in the lattice parameter and X-ray pattern. We therefore propose the deformation as an alternative hypothesis to a superlattice of different argon densities in neighboring channels. As both interpretations can explain the additional X-ray peaks, it would therefore be interesting to see whether additional experiments can confirm our proposed deformation.

The appearance at intermediate pressures and disappearance at high pressures of adsorbate-induced deformation provides us with insight into how the deformation of IRMOF-74-V is stabilized. By comparing Fig. 2.5 with the adsorption isotherms, we note that the deformation is observed before the channels are filled and disappears as the lattice saturates with argon. As the channels fill, adsorbate-adsorbate forces in the dense argon environment destabilize the deformation and force the lattice to return to its standard size and structure, potentially to accommodate more adsorbates. Although we do not characterize IRMOF-74-V as a breathing MOF, this observation allows us to draw a parallel between this system and breathing MOFs, which collapse at intermediate loadings to improve adsorbate interactions and expand at high loadings to allow adsorbates to occupy more space[91].

GCMC simulations showed no evidence of the argon adsorbate superlattice in a rigid framework as proposed by Cho *et al.* However, GCMC simulations did demonstrate that, in a very narrow pressure range, irregular hexagonal channels in the deformed lattice can adsorb more argon compared to regular hexagonal channels. This implies the opposite conclusion of Cho *et al.*, who proposed small regions of high loading separated by large regions of low loading. Our GCMC simulations of individual hexagonal channels suggest that regions of low loading can be surrounded and separated in space by regions of high loading.

Our simulations show that the observed breathing effect is a subtle balance between the energetics of the deformation of the lattice and interactions of argon atoms. For example,

Cho *et al.* observed that a dip in the lattice parameter occurs over a very narrow pressure range in IRMOF-74-V-hex and over a less narrow pressure range in IRMOF-74-V. A possible explanation is that the presence of the side group in IRMOF-74-V-hex makes it more difficult to deform the lattice. However, further work is needed in refining our model to reliably study the effects of these subtle differences.

The appearance and disappearance of the observed deformation is similar to the phase transitions of a conventional breathing MOF, where the flexible unit cell is open in vacuum, closes to become narrow upon gas adsorption, then opens again as the pores saturate. The deformation we observe, however, is unique because it cannot be described with a single unit cell of the original structure. Unlike conventional breathing MOFs in which neighboring pores simultaneously close at intermediate pressures and open at high pressure, neighboring pores in the IRMOF-74 series necessarily deform differently and form a repeating, crystalline pattern. The length scale required to study this deformation is therefore much larger than a single unit cell of the material.

Chapter 3

Xylene Dynamics in MOF-5

In this work, results from MD simulations are compared with results from nuclear magnetic resonance (NMR) experiments to study *para*-, *meta*- and *ortho*-xylene behavior in MOF-5, probing the effects of adsorbate geometry in a weakly interacting isotropic MOF system. We study the effect that adsorbate geometry has on both translational and rotational xylene dynamics in this canonical framework. Simulation and experimental findings corroborate each other, and the findings suggest that while *para*-xylene has the lowest free energy barrier for moving translationally between MOF cages, its shape causes it to have the slowest in-plane rotational dynamics.

This chapter is adapted from the following publication:

V. J. Witherspoon, L. M. Yu, S. Jawahery, E. Braun, S. M. Moosavi, S. K. Schnell, B. Smit, J. A. Reimer. Translational and Rotational Motion of C8 Aromatics Adsorbed in Isotropic Porous Media (MOF-5): NMR Studies and MD Simulations. *The Journal of Physical Chemistry C*, **2017**.

3.1 Introduction

The separation of xylene isomers poses a lucrative scientific challenge, as distillation of these isomers accounts for a significant amount of global energy consumption[124]. Composed of a conjugated ring perturbated by two methyl groups (see Fig. 3.1 for a visual aid), xylene isomers have similar kinetic diameters (1 Å difference) and similar chemical properties, including host-guest interaction energies, which make the design of a selective adsorbent extremely difficult. Several classes of materials have been investigated for their xylene separation potential, including MOFs, zeolites, molecular sieves and quantum dots[125]. MOFs in particular have demonstrated promimse for this application[125]. Given that the discov-

ery of a solid sorbent capable of efficient xylene separation has the potential to make a dent in a 50 gigawatt per year global expenditure[124], further investigation of selective xylene dynamics in MOF adsorbents is warranted.

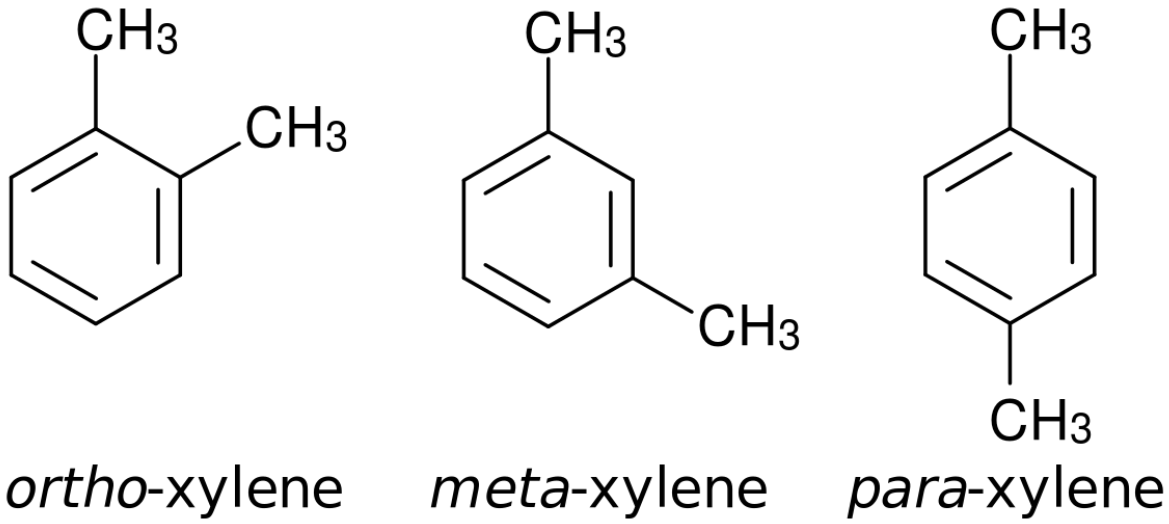

Figure 3.1: Xylene (C_8H_{10}) isomers studied in this work. *Ortho*-, *meta*- and *para*-xylene have kinetic diameters of 6.8, 6.8 and 5.8 Å, respectively[126].

To determine the suitability of MOFs for particular separation applications, transport phenomena are commonly investigated by performing macroscopic measurements (e.g. breakthrough measurements) that characterize effective mass transport values containing contributions from both intercrystalline and the intracrystalline regimes[127]. To gain insight into the mechanisms that determine these macroscopic measurements, molecular-scale interactions need to be measured. In particular, MOFs offer the nanoporous media community a unique opportunity to improve our understanding of how adsorbed molecules move in a confined spaces since both the topology and the chemical affinity are well-defined[128]. NMR-based techniques have been previously been employed to quantify self-diffusion coefficients in an effort to understand translational motion. Most studies thus far have focused on determining differences between strongly and weakly adsorbed molecules, where large differences in the observed diffusive properties are used to understand motion and selectivity[129, 130]. This scenario is in stark contrast to the case of xylene separation, where strength of adsorption is generally nearly identical across the series of isomers.

The selectivity of certain MOFs such as MIL-47[131, 132, 133] and MIL-53 [134, 135, 136, 137] for xylene separation has been studied. π-π stacking between linker molecules and the aromatic ring on the xylene isomers was identified as the dominant type of host-guest interaction, and the selectivity of these one-dimensional channel type MOFs was attributed to the anisotropy of linker arrangements. Macroscopic breakthrough measurements at high temper-

ature (553 K) and pressure (1.2 bar) have been used to determine transport intracrystalline diffusivities of xylenes in MOF-5 and showed that the vapor phase *para*-xylene diffused two times slower than the other isomers. This implies that the geometry of the adsorbate plays a role in modulating dynamics[138]. Previous descriptions of how C8 aromatics diffuse in porous environments postulate that entropy may play a role in determining the molecular mobility[139, 140, 141, 142], yet present very little systematic evidence.

We have performed MD simulations in order to quantify diffusion while gaining a molecular-level understanding of liquid-phase xylene isomer dynamics in a confined MOF system: the canonical MOF-5 framework (shown in Fig. 3.2). We compare the results of our simulations to NMR results, which probe translational motion by measuring self-diffusion coefficients and probe rotational motion by measuring longitudinal relaxation times (T_1, and its related rate $R_1 = 1/T_1$)[143, 144, 145, 130, 129]. Our simulations allow us to analyze the interplay between rotational and translational motion as well as characterize the spatial probability distributions and relative orientations of the different xylene isomers when adsorbed in the pores of MOF-5. Taken as corrobation of self-diffusion coefficient and longitudinal relaxation rate measurements from NMR experiments performed at similar liquid-phase conditions, we are able to better understand and speculate about how the geometric properties of xylene isomers can influence the observed separation performance of MOF adsorbents.

3.2 Simulation Models

MD simulations of xylene isomer dynamics in MOF-5 used a combination of force fields. The Lennard-Jones potential, shifted and truncated at 12.0 Å, was used to describe dispersive interactions. MOF-5 framework atoms were modeled using the Dubbeldam force field[73], and the framework was assumed to be rigid (framework atoms were kept fixed during the simulation) since it has been shown that framework flexibility does not have an effect on adsorbate diffusion in MOF-5[146]. The experimental crystal structure was used for the fixed positions of the framework atoms. Interactions between adsorbed xylene molecules were calculated directly from the parameters given by the TraPPE force field[147], and Lorenz-Berthelot mixing rules were used to calculate interactions between framework atoms and adsorbate atoms. This Dubbeldam + TraPPE force field has been shown to provide good agreement with experimental diffusion coefficients of small aromatic molecules in MOF-5[73]. As the TraPPE models do not have partial charges, Coulombic interactions were not calculated.

To prepare simulation systems comparable to experimental liquid-phase conditions, the MOF-5 framework (see Fig. 3.2) was loaded with guest molecules at densities corresponding to the saturated liquid densities at four different temperatures within the range of experimental interest. These liquid loadings were calculated from GCMC simulations in a previous work[148]. A comparison of the isotherm predicted by this force field to the experimental isotherm at 298 K is shown in Fig. 3.3. The GCMC simulated isotherms saturate at lower pressures than the experimental isotherm, but the shape and step pressure of the isotherms

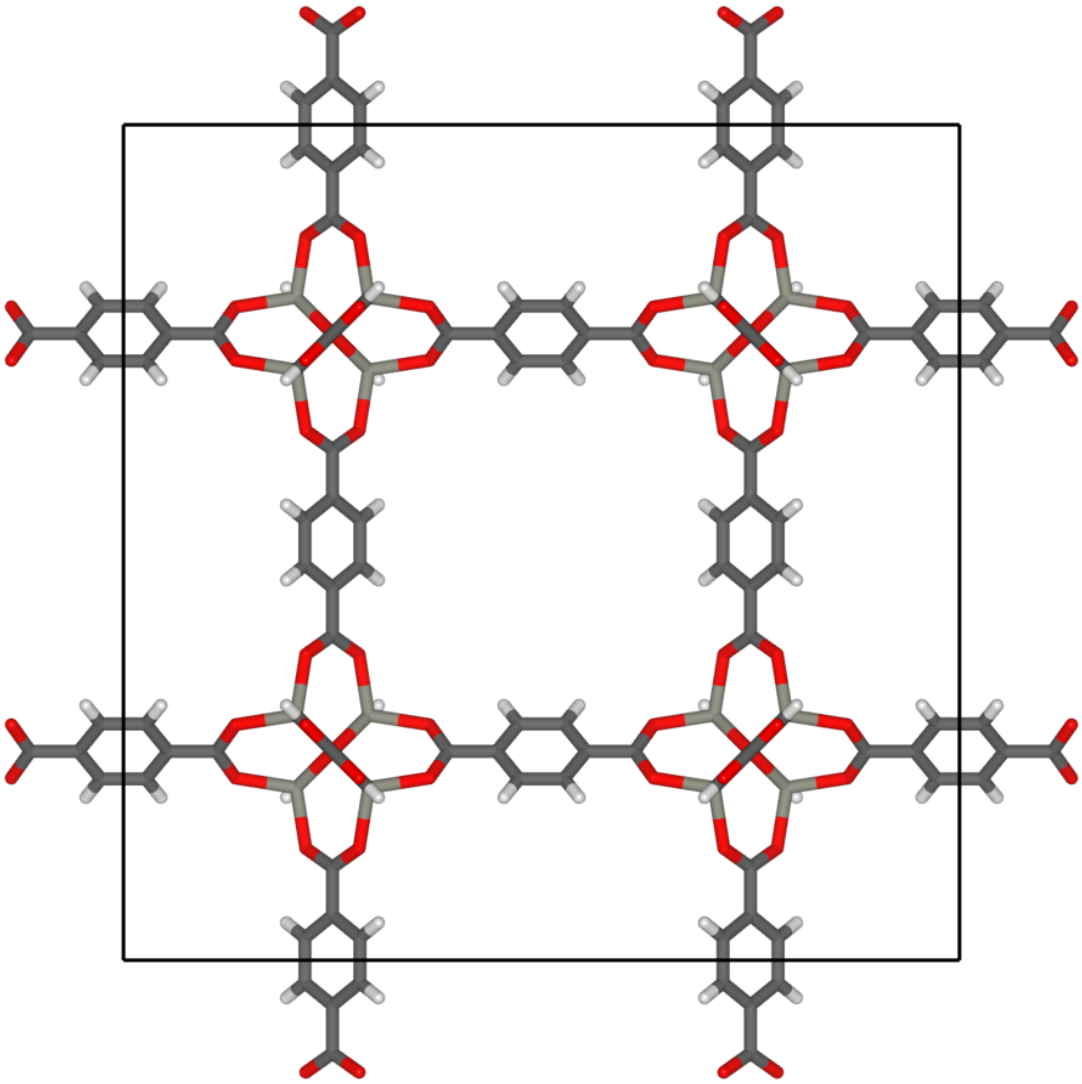

Figure 3.2: Crystal structure of the canonical MOF-5 (IRMOF-1) crystal, which was used as the isotropic adsorbent material in this work. Zinc, carbon, oxygen and hydrogen are shown in dark grey, light grey, red and white, respectively. Zinc atoms are located in Zn_4O tetrahedral units and are connected by the 1,4-benzenedicarboxylate (BDC) linkers such that a cubic crystal lattice is formed[5].

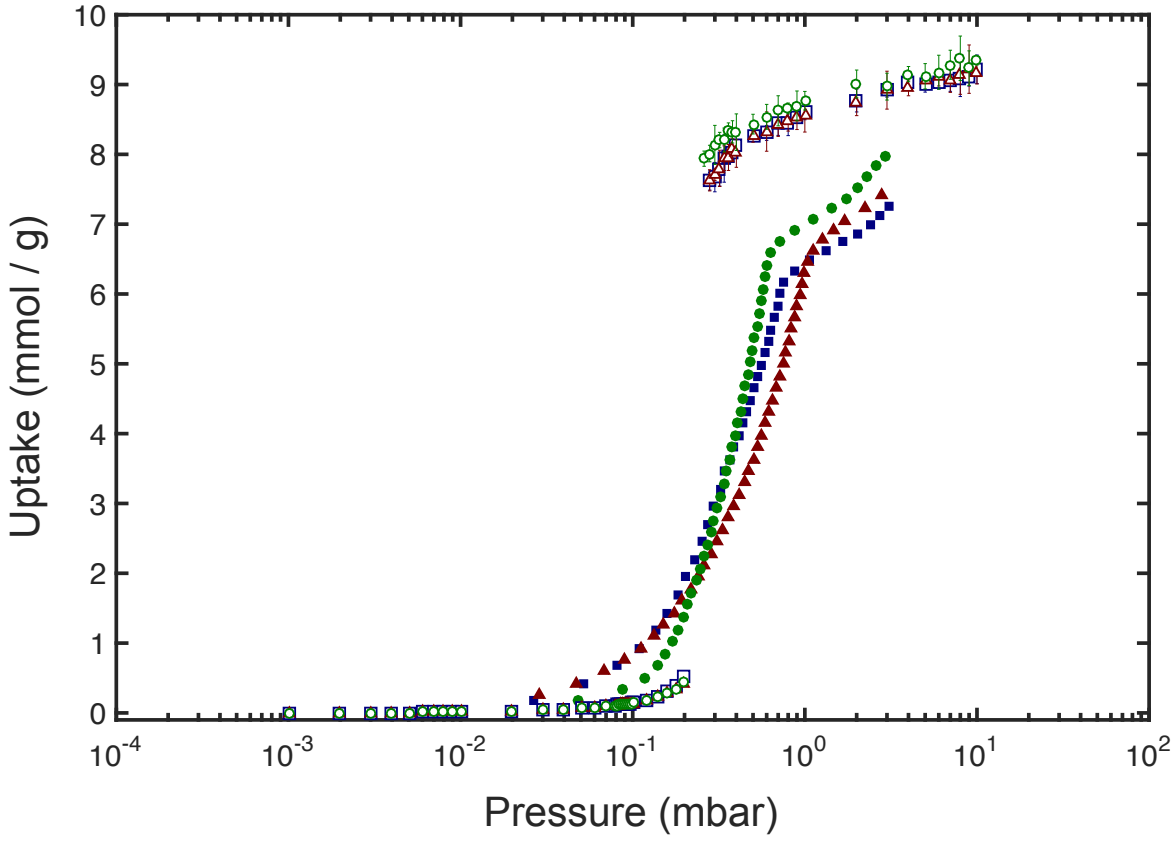

Figure 3.3: Experimental (para ■, ortho ●, meta ▲) and simulated (para □, ortho ○, meta △) pure-component adsorption isotherms of the three xylene isomers in MOF-5, taken at 298 K. Simulated adsorption isotherms were obtained with GCMC simulations using the same force field as was used in the MD simulations. Data were collected over 1,000,000 production cycles following 1,000,000 equilibration cycles. The simulation box consisted of 1 unit cell of MOF-5.

are generally in very good agreement.

Table 3.1: Loadings used in MD simulations in units of molecules per unit cell.

Temperature (K)	*ortho*-xylene	*meta*-xylene	*para*-xylene
270	54	53	53
280	53	53	53
290	53	51	51
300	52	50	50

Molecular dynamics simulations were conducted with LAMMPS[118] in the NVT ensemble using a timestep of 0.5 fs, the Nosé-Hoover chain thermostat[78, 79] and a rigid-body time integrator[149].

3.3 Translational Motion

To calculate diffusive properties of liquid-phase xylenes in MOF-5, MD simulations were equilibrated for 5 ns, followed by a production period of at least 100 ns, which was found to be sufficiently long for the mean squared displacement (MSD) to become a linear function of time, as verified by measuring the slope of the MSD plot on a log-log scale. MSD as a function of elapsed time τ is defined as:

$$MSD(t) = \left\langle \Delta r(\tau)^2 \right\rangle = \left\langle [r(t+\tau) - r(t)]^2 \right\rangle \tag{3.1}$$

where r is the instantaneous position of the center-of-mass of a xylene molecule. Self-diffusion coefficents were obtained by fitting the Einstein relation:

$$D_S = \frac{1}{6} \lim_{t\to\infty} \frac{d}{dt} \left\langle [r(t) - r(0)]^2 \right\rangle \tag{3.2}$$

to the linear portion of the MSD versus time plot, using the order-n algorithm[74, 150] to collect MSD data.

According to both simulations and experiment, *para*-xylene displays the fastest self-diffusion coefficient at all temperatures (Fig. 3.4) and the lowest experimental calculated activation energy for translational motion (Table 3.2). *Para*-xylene translational motion in MOF-5 deviates from bulk isomer behavioral trends[151] by exhibiting the smallest Arrhenius pre-exponential factor; this is surprising because when measured in bulk it has the largest[152]. The simulation self-diffusion coefficients are on the same order of magnitude as the experiment and display the same ordering between isomers.

The simulated and experimental temperature dependence of *para*-xylene self-diffusion are in extremely good agreement. As shown in Table 3.2, the activation energies of motion obtained from Arrhenius fits are identical. The simulated and experimental temperature

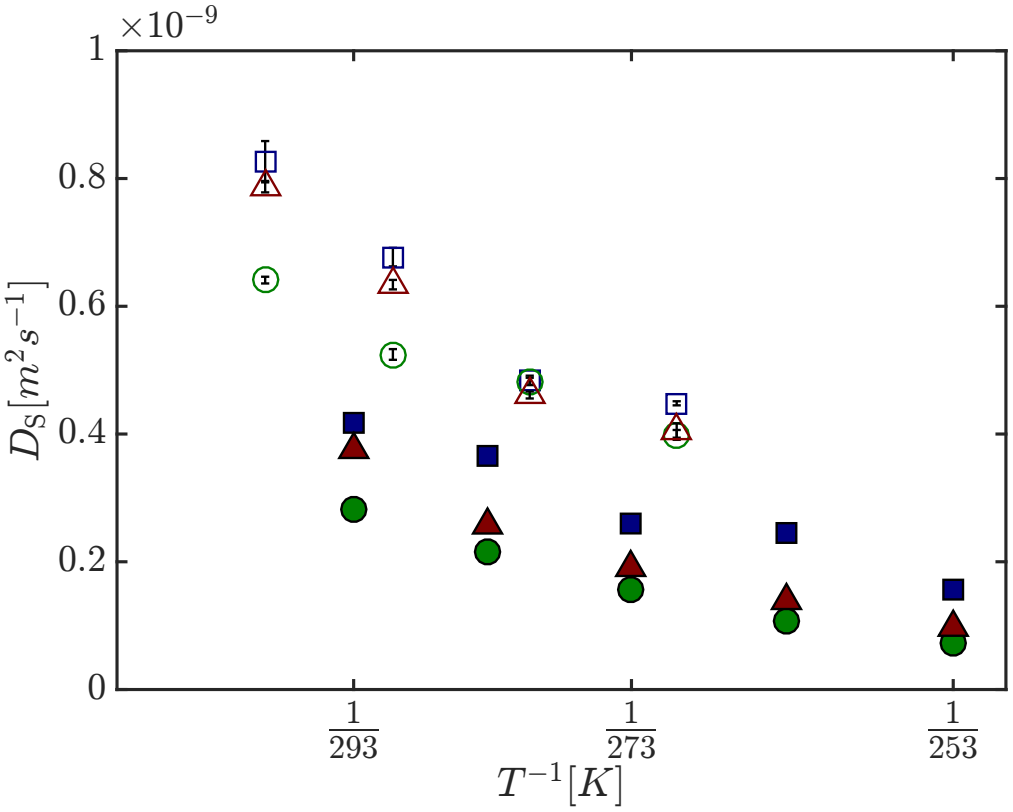

Figure 3.4: The experimental inverse temperature dependence of the self-diffusion coefficient for each xylene (para ■, ortho ●, meta ▲), and the simulated self-diffusion coefficients (para □, ortho ○, meta △). Error bars denote standard deviations.

dependence of *meta*- and, in particular, *ortho*-xylene are in less close agreement. This could be a result of the temperature-dependence being very sensitive to adsorbate loadings.

We further explored the guest molecule configurations by considering the spatial probability distributions from the MD simulations. Spatial density distributions of xylenes (Fig. 3.5) were generated with data from MD simulations where the center-of-mass of each xylene molecule was recorded every 5 fs and binned into a $100 \times 100 \times 100$ grid overlaid on the MOF-5 structure. As MOF-5 is cubic, the three-dimensional grid was reduced to a two-dimensional grid by averaging together all slices in one of the dimensions. These figures reveal the preferential adsorption sites of each xylene isomer. *Meta*-xylene prefers to adsorb in the center of the pore, while *ortho*-xylene prefers adsorption closer to the metal clusters that are located at the corners of the pore (Fig. 3.5A-B, darker shaded areas). *Para*-xylene, by contrast, shows a more uniform distribution throughout the pore (Fig. 3.5C). The presence of multiple and proximal preferential adsorption sites for *ortho*-xylene and *meta*-xylene

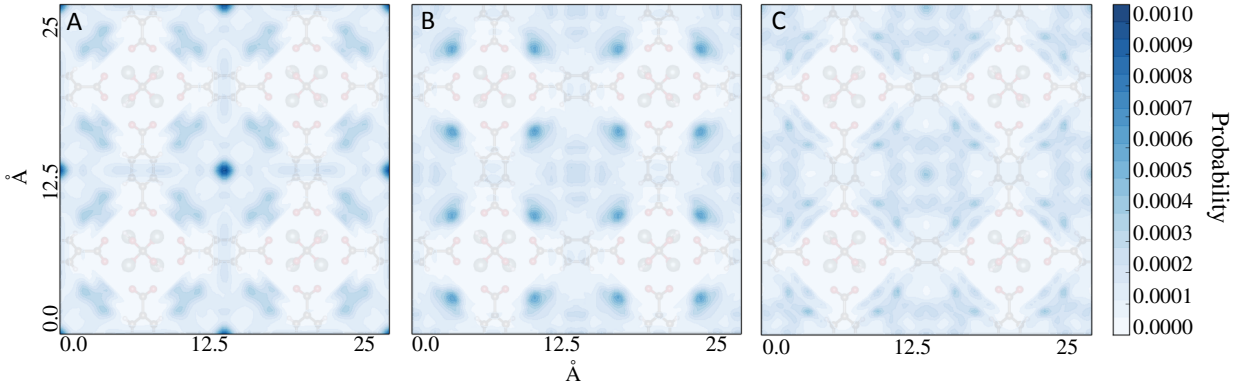

Figure 3.5: Results of the MD simulations at 280 K and loadings as shown in Table 3.1 displaying the spatial probability distribution of liquid phase xylene molecules in the MOF-5 structure: (A) *meta*-xylene, (B) *ortho*-xylene, (C) *para*-xylene.

Table 3.2: $E_{a,trans}$ calculated from an Arrhenius fit to the experimental data and simulated data from Fig. 3.4. The actual $D_{0,trans}$ were taken from the intercept of the linear fit with inverse temperature.

	para-xylene	*meta*-xylene	*ortho*-xylene
	Experimental		
$E_{a,trans}$ (kJ mol^{-1})	15.3	19.7	21.2
$D_{0,trans}$ (m^2 s^{-1})	1.8 $\times 10^{-7}$	1.68 $\times 10^{-6}$	2.45 $\times 10^{-6}$
	Simulated		
$E_{a,trans}$ (kJ mol^{-1})	15.3	16.1	10.3
$D_{0,trans}$ (m^2 s^{-1})	3.79 $\times 10^{-7}$	3.93 $\times 10^{-8}$	5.06 $\times 10^{-7}$

suggests that their translational diffusion mechanism involves the hopping of molecules between these sites and thus that these adsorbates must overcome a larger free energy barrier to diffuse compared with *para*-xylene. These observations are consistent with the trend in the experimentally determined translational activation energies.

3.4 Rotational Motion

We define rotational displacement in the MD simulations as:

$$\psi(\tau) = \int_0^t \Delta\hat{\psi}(t')dt' \tag{3.3}$$

where both the magnitude and direction of vector $\Delta\hat{\psi}(t')$ are given by the normalized vector

Table 3.3: Experimental $E_{a,rot}$ of xylene molecules calculated from fitting the experimental longitudinal relaxation rate to an Arrhenius relation given in Fig. 3.7.

	para-xylene	*meta*-xylene	*ortho*-xylene
$E_{a,rot}$ (kJ mol^{-1})	47.26	12.88	11.55

of interest $u(t)$ at times $t = t'$, $t' + dt'$. The magnitude of $\Delta\hat{\psi}(t')$ is given by:

$$|\Delta\hat{\psi}(t')| = \cos^{-1}\left(u(t' + dt') \cdot u(t')\right) \tag{3.4}$$

and the direction is given by $u(t' + dt') \times u(t')$[153].

In this work, the vector of interest $u(t)$ is either the bond vector pointing from an aromatic xylene ring carbon to the its bonded methyl group (in-plane, $\parallel$) or the vector normal to the aromatic xylene ring (out-of-plane, $\perp$). Analogously to translational motion, rotational self-diffusion coefficients were obtained by fitting the relation:

$$D_R = \frac{1}{6}\lim_{t\to\infty}\frac{d}{dt}\left\langle[\psi(t) - \psi(0)]^2\right\rangle \tag{3.5}$$

to the linear portion of the rotational MSD versus time plot, defined as:

$$MSD_R(t) = \left\langle\Delta\psi(\tau)^2\right\rangle = \left\langle[\psi(t+\tau) - \psi(t)]^2\right\rangle \tag{3.6}$$

Experimentally measured molecular rotation relaxations rates (R_1) are shown in Fig. 3.7, and activation energies resulting from Arrhenius linear fits to this data are shown in Table 3.3. *Para*-xylene is found to have almost four times the rotational activation energy of the other isomers and thus must be experiencing some combination of increased spatial restriction and/or a longer isotropic rotational correlation time. This is different from bulk behavior where the rotational activation energy ($E_{a,rot}$) of all the xylene isomers are on the same order of magnitude[154].

Table 3.4: The simulated in-plane ($\parallel$) and out-of-plane ($\perp$) rotational activation energies and the pre-exponential factors fitted from an Arrhenius relation in Fig. 3.8.

	para-xylene	*meta*-xylene	*ortho*-xylene
$E_{a,rot,\parallel}$ (kJ mol^{-1})	17.03	11.37	6.0
$D_{0,rot,\parallel}$ (rad^2 s^{-1})	37.83	5.95	1.4
$E_{a,rot,\perp}$ (kJ mol^{-1})	10.84	10.06	9.05
$D_{0,rot,\perp}$ (rad^2 s^{-1})	10.43	4.2	2.44

MD simulations performed at the aforementioned loadings affirm the notion of *para*-xylene restricted rotational motion. For all three xylenes, two types of rotational motion were distinguished and tracked during the course of simulations. In-plane xylene rotation was tracked with the methyl bond vectors as a reference, and out-of-plane xylene rotation

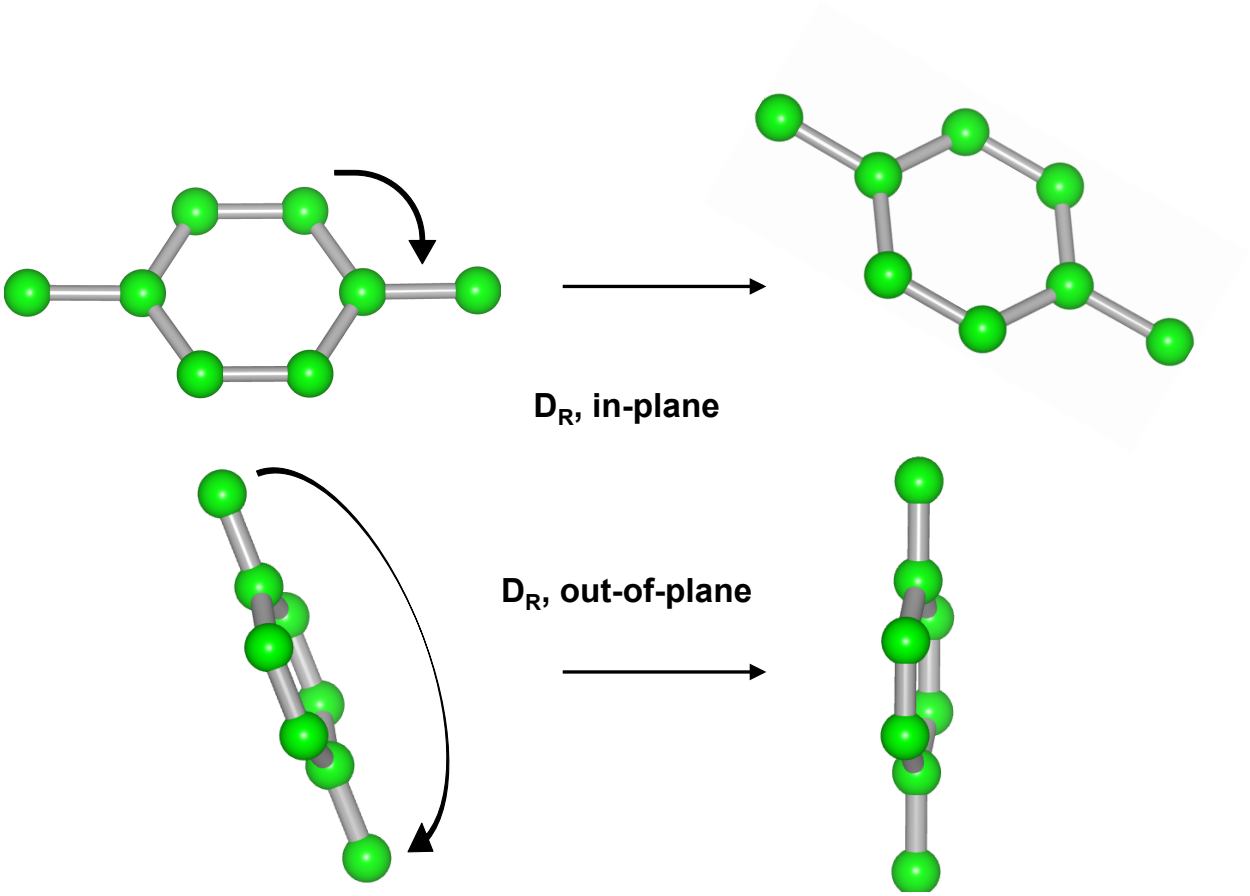

Figure 3.6: The two types of rotational motion for which simulated rotational self-diffusion coefficients were measured: in-plane ($\parallel$) and out-of-plane ($\perp$) motion. The in-plane rotational motion is tracked using the orientation of the methyl bond vectors, while the out-of-plane rotational motion is using the orientation of the vector normal to the plane of the aromatic ring. The isomer shown in the examples is *para*-xylene and carbon atoms are shown in green. Although *para*-xylene is used to illustrate the example, the orientation reference vector definitions were the same for all xylenes.

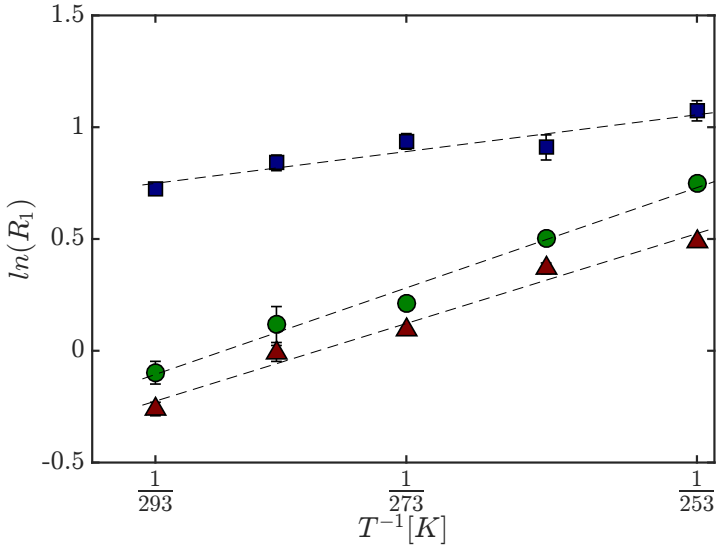

Figure 3.7: The experimental inverse temperature dependence of R_1 for each xylene isomer (para ■, ortho ●, meta ▲). The dashed lines represent a linear fit to an Arrhenius relationship.

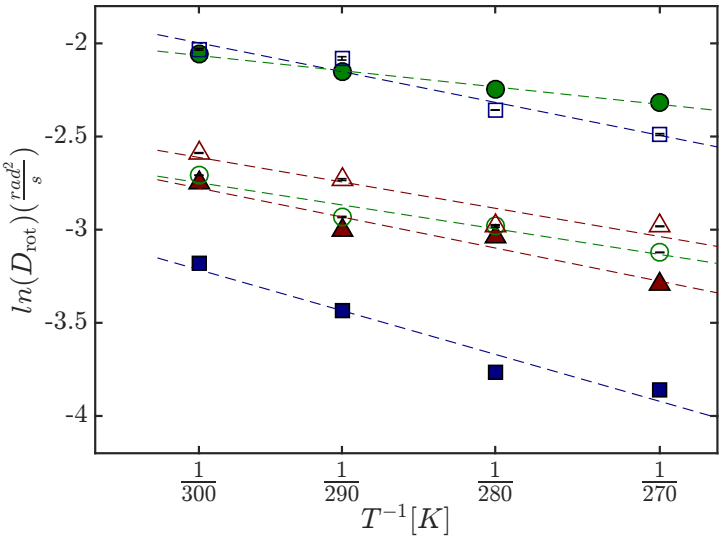

Figure 3.8: The inverse temperature dependence of the simulated rotational self-diffusion coefficients for each xylene isomer where the filled symbols represent the in-plane ($\parallel$) rotation (para ■, ortho ●, meta ▲) and the empty symbols represent out-of-plane ($\perp$) rotation (para □, ortho ◯, meta △). The dashed lines represent a linear fit to an Arrhenius relationship.

was tracked with the vector normal to the aromatic ring as a reference. The two rotational modes are visually illustrated in Fig. 3.6.

Para-xylene displays a large difference between the in-plane and out-of-plane diffusion coefficients, with the out-of-plane coefficients being a factor of three larger (Fig. 3.8). The difference between in-plane and out-of-plane rotational diffusion coefficients was less pronounced for the other two isomers, although the magnitudes of the diffusion coefficients are also smaller. The trend in the in-plane activation energies derived from the simulation results show that *para*-xylene's in-plane rotational motion activation energy is greater than that of both *meta*-xylene and *ortho*-xylene (Table 3.4).

To further explore the effect of confinement on the orientations sampled during rotational motion, the angle between the methyl bond and the bond connecting the nearest-neighbor carboxylate group to the aromatic part of organic linker was tracked. The probability of finding a molecule oriented at a particular angle was then calculated for each xylene and the results are displayed in Fig. 3.9. The observed probability distributions shown in solid black lines can be compared to the dashed black lines, which shows a random distribution of methyl group orientations using the functional form $P(\theta) = \frac{1}{2}\sin(\theta)$. All xylenes display a dominating peak larger than that of the random distribution around 90°. This suggests the most favored orientation for a methyl group relative to the framework phenyl ring may be a *t*-configuration near a π-pocket of the ligand. This cannot, however, be the case for *ortho*-xylene, as Fig. 3.5 shows that the molecular center-of-mass is predominantly found in the corners of the pore rather than the center.

Additional features in the *meta*-xylene and *para*-xylene angle probability distributions can be intuited by considering the positions of the two methyl groups relative to each other. Fig 3.10 demonstrates the proposed unique *meta*-xylene configurations. The peaks at 60° and 120° in the *meta*-xylene plot are observed because when one methyl group is in the favored orientation (perpendicular to one set of linkers) and the aromatic xylene ring is parallel to the other set of organic linkers, the second methyl group forms a 60° or 120° angle with the nearest neighboring carboxylate group. The *para*-xylene distribution is unique because when the aromatic xylene ring is similarly aligned parallel to one set of organic linkers, both methyl groups are perpendicular to the other set, and there should therefore be only a single peak at 90°. The additional features at 140° and 40° indicate that *para*-xylene cannot fit into configurations where it is oriented exactly parallel to a set of organic linkers and must be tilted with respect to the pore. *Para*-xylene therefore samples a more restrictive environment due to its rigid rod like shape.

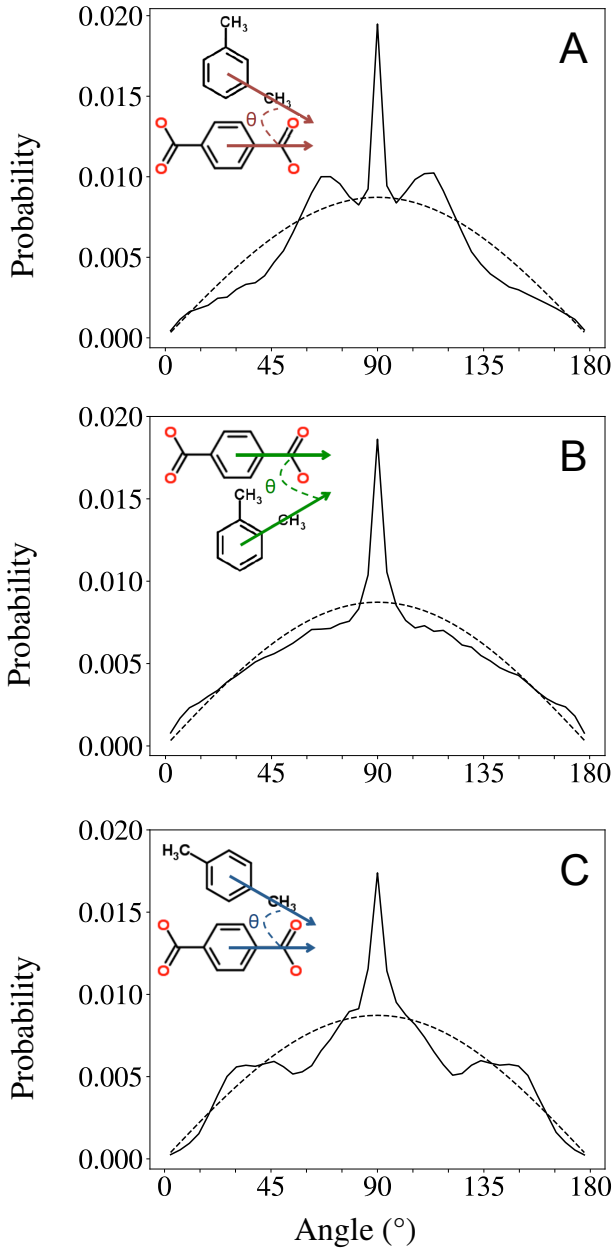

Figure 3.9: Probability density functions describing the likelihood of finding a methyl bond on a xylene molecule oriented at a range of angles relative to the nearest neighboring carboxylate group on a framework linker, measured according to the figure insets and the examples of Fig 3.10. Resulting distributions (A) *meta*-xylene, (B) *ortho*-xylene, (C) *para*-xylene. In (A), (B) and (C), the dashed black lines reflect a random distribution of methyl orientations.

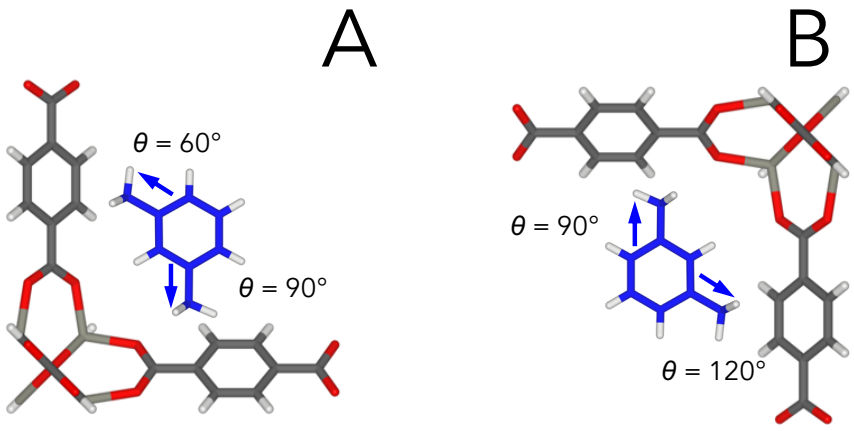

Figure 3.10: Proposed configurations that explain the symmetric peaks in the *meta*-xylene probability density functions shown in Fig 3.9. The examples demonstrate how the instantaneous methyl-carboxylate angles are measured. Oxygen atoms are red, hydrogen atoms are white, zinc atoms are light grey, and carbon atoms on the xylene and linker are blue and dark grey, respectively.

3.5 Conclusion

MOF-5, experimentally synthesized as a large crystal, was imbibed with saturated-liquid loadings of *meta*-xylene, *ortho*-xylene, and *para*-xylene. The effects of subtle geometric differences between the isomers are manifest in the guest molecule translational and rotational motions, as observed using NMR techniques. Measurement of the experimental self-diffusion coefficients and the longitudinal relaxation times as functions of temperature at constant loading allowed for the quantification of the translational and rotational activation energies for each species. *Para*-xylene was experimentally observed to have the fastest self-diffusion coefficient at all temperatures ($para > meta > ortho$), the lowest activation energy for translational motion ($para < meta < ortho$), and the highest activation energy for rotational motion ($para > meta > ortho$). These results were compared with MD simulations and confirm the constriction of rotational freedom in an isotropically confined geometry and the faster translational motion of the most rod-like molecule, *para*-xylene. MD simulations indicate that neither *meta*-xylene nor *ortho*-xylene experience comparable restrictions for in-plane rotations when adsorbed in MOF-5, supporting the experimental findings that *para*-xylene faces higher energy barriers for rotational motion.

Chapter 4

Refinement of Cationic Dummy Model Parameters for M-MOF-74 Series

We present force fields developed from periodic density functional theory (DFT) calculations that can be used in classical molecular simulations to model M-MOF-74 (M = Co, Fe, Mg, Mn, Ni, Zn) and its extended linker analogs. Our force fields are based on cationic dummy models (CDMs). These dummy models simplify the methodology required to tune the parameters and improve the accuracy of the force fields. We have used our force fields to compare mechanical properties across the M-MOF-74 series, and determine that increasing the size of the linker decreases the framework rigidity. In addition, we have applied our force fields to an extended linker analog of Mg-MOF-74 and characterized the free energy of previously-reported deformation pattern, in which the one-dimensional hexagonal channels of the framework become irregular. The free energy profiles confirm that the deformation is adsorbate-induced and impossible to access solely by a pressure stimulus. Based on our results, we conclude that the force fields presented here and others that may be developed using our methodology are transferable across metal-organic framework series that share a metal center topology. Finally, we believe that these force fields have the potential to be adapted for the study of complex problems in MOF chemistry, including defects and crystal growth, that have thus far been beyond the scope of classical molecular simulations.

This chapter is based on material from the following publication:

S. Jawahery, N. Rampal, S. M. Moosavi, M. Witman, B. Smit. *Ab Initio* Flexible Force Field for Metal-Organic Frameworks Using Dummy Model Coordination Bonds. *Journal of Chemical Theory and Computation*, **2019**.

4.1 Introduction

For sufficiently rigid materials, accurate force fields have been developed to predict the thermodynamic properties of adsorbed gases in MOFs[155, 25]. However, to predict adsorption in flexible materials and study mechanical properties, one cannot assume that a material is rigid and force fields that allow MOF atoms to move are required. The dependence of framework mechanical properties on the structure and chemical identity of some MOFs has recently been explored. Experimental and recent computational works on zeolitic imidazolate framework (ZIF), a sub-class of MOFs, mechanical properties address the dependence of framework elasticity on topology and linker chemistry[156, 157, 158]. However, further investigation is needed to understand the effects of linker chemistry beyond this framework series.

Both DFT and classical molecular simulations have been used to study structure-property relationships of nanoporous materials[22, 23, 159, 160], In principle, *ab initio* methods such as density functional theory (DFT) can be used to study MOF properties influenced by framework flexibility. In practice, the scope of and number of structures included in DFT-based studies is necessarily small (on the order of hundreds of structures) because of the significant computational expense[161, 162, 159]. By contrast, molecular simulation studies that take advantage of classical force fields have been used to screen the adsorption properties of hundreds of thousands of structures[18]. It remains difficult, however, to use classical force field-based approaches to capture properties relating to the dynamics and integrity of the framework itself. There is still a practical need for simulations to be able to capture framework flexibility, as recent experimental and theoretical works have demonstrated that both subtle flexible modes and large framework volume changes can influence MOF performance with regards to adsorption-based applications[93, 163, 164, 165].

There are two approaches to describe flexibility at a MOF's coordination centers, where metals and atoms on organic linker molecules form coordination bonds[166]. Bonded force field terms are the more common approach, using functional forms such as harmonic or Morse potentials to capture the coupled motion of two atoms forming a coordination bond, and similar angle, torsion and dihedral terms to capture three-body and four-body interactions. This is the approach taken by an extension of the Universal Force Field to MOFs (UFF4MOF), the MOF-FF force field, and a number of other force fields made for specific structures[167, 168]. The QuickFF package developed by the Van Speybroeck group, which aims to parameterize force fields on-the-fly from *ab initio* data also uses bonded force field terms[169]. A second approach uses only non-bonded potentials to describe interactions between metals and coordinating linker atom. This approach is well suited to describing subtle changes in the framework that preserve coordination geometry. Non-bonded potentials have been used in structure prediction procedures for inorganic chemistry including[170, 171], more recently, Zr-based MOFs[172]. The non-bonded potential approach has been used to demonstrate water-induced dissolution of MOF-5[110], investigate MOF self-assembly[42, 43, 44, 45] and also allowed us in a previous work to computationally establish the occurrence of a novel deformation pattern by an extended linker analog of Mg-MOF-74 upon argon

adsorption[173]. The same deformation pattern was experimentally reported as occurring in Co-MOF-74 upon adsorption of *ortho*-xylene[126].

In a previous work by Mercado *et al.*, a periodic DFT-based approach was used to estimate and fit non-bonded interaction potentials between adsorbate molecules and framework atoms[25]. In this work, we present a procedure to develop models of metal-coordinating atom interactions using only non-bonded potentials. We present a methodology that uses periodic DFT calculations to estimate the pairwise force between metals and coordinating atoms, and fit interaction potentials to these pairwise forces. We focus here on the M-MOF-74 series (M = Co, Fe, Mg, Mn, Ni, Zn), but the method can be applied to other frameworks. We demonstrate that the resulting force fields are robust and are transferable to experimentally-synthesized extended linker analogs of M-MOF-74[174]. This force field development methodology can help further our understanding of how MOF mechanical properties depend on topology and building block chemistry[158]. Our force fields also have the potential to push MOF modeling research into new directions. Because these force fields allow coordination bonds to break and form, we envision adapting this model to be compatible with reliable parameters for metal-solvent and linker-solvent interactions. A compatible combination of framework-solvent and metal-linker interactions would enable us to study complex problems such as defects, surface properties, formation and dissolution of MOFs, which have thus far been largely inaccessible topics for classical molecular simulations.

4.2 Methodology

Overview

We have parameterized classical force fields to be used for molecular simulations of M-MOF-74 analogs by employing cationic dummy models (CDMs)[59, 63, 67], which capture the experimentally-observed octahedral coordination sphere of the metal cations[49]. The function of the CDMs is illustrated in Fig. 4.1. Rather than using a single point charge, the CDMs consist of six point charges arranged in octahedral symmetry around a central bead, which is a center for both a point charge and a Van der Waals interaction. Ligands interact with both the six surrounding point charges and the central bead. Because of the set number and geometrical arrangement of the surrounding point charges, the metals remain bound to the correct number of linker atoms, replicating the effect of octahedrally arranged orbitals.

We present here a method by which we estimate and fit interatomic framework potentials to forces from periodic density functional theory (DFT) calculations. Vanduyfhuys *et al.* took a related approach when developing their MOF force field development method implemented in the QuickFF package. Their method uses the Hessian matrix (composed of second derivatives of the framework energy with respect to the geometry) of the equilibrium framework structure to develop force field parameters[169]. In this work, we take a different approach. Instead of optimizing many force field parameters simultaneously in order to capture the total force acting on each atom, we focus on optimizing one pairwise interaction at

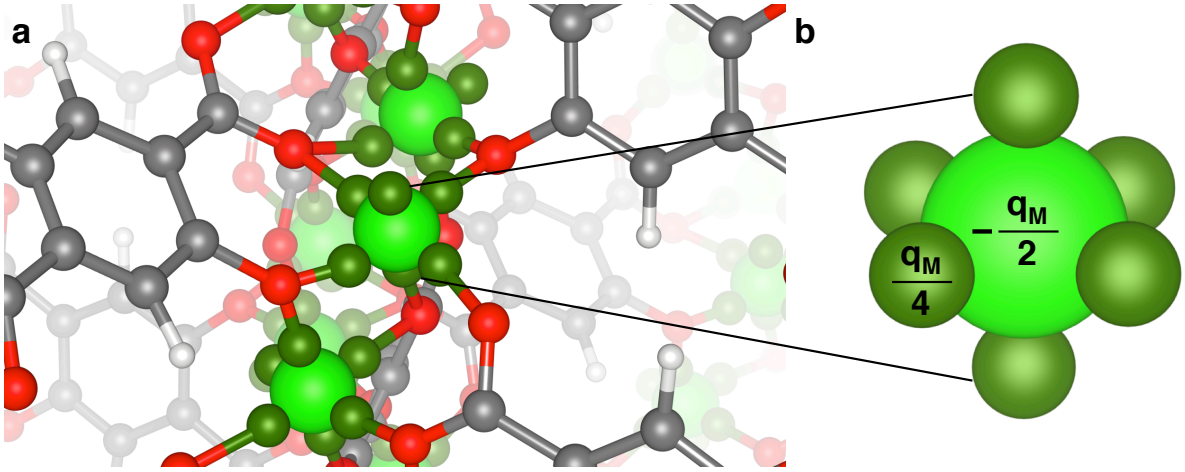

Figure 4.1: (a) Cationic Dummy Models (CDMs) in a snapshot of the structure of M-MOF-74 and (b) the distribution of total metal charge q_M on each CDM. Oxygen, carbon, hydrogen, metal atoms and dummy beads are shown in red, grey, white, light green, and dark green, respectively. Charge is delocalized around the central metal atom such that the octahedral coordination environment of the metals is reproduced. Five of the six dummy beads on each CDM form bonds via non-bonded interaction potentials with linker oxygen atoms. One dummy bead forms no bonds with linker oxygens and points towards the center of the pore, reproducing the open-metal site in M-MOF-74.

a time while fitting each interaction to independent sets of data. We fit potentials that act between the central bead of the metal CDMs and their directly coordinating oxygen atoms. Our fitted potentials are developed by estimating pairwise metal-oxygen forces from total *ab initio* atomic forces.

Ab Initio Force Calculations

For each M-MOF-74 analog, we perform 101 *ab initio* calculations. To fit our force field, we calculate *ab initio* atomic forces on 100 configurations that relate to displacements of a single metal atom. The procedure for displacing this metal atom is described later. We perform an additional calculation to determine the forces in a structure where the displaced metal atom is far from its original neighbors. The *ab initio* atomic forces from this final calculation are used later to estimate pairwise metal-oxygen forces.

All *ab initio* calculations were performed using DFT with periodic boundary conditions as implemented in the Vienna *Ab initio* Simulation Package[175]. Calculations were performed with PBE[176] and projector augmented wave (PAW) pseudopotentials[177, 178]. For all frameworks M-MOF-74 (M = Co, Fe, Mn, Ni), Hubbard U corrections were applied with values optimized specifically for M-MOF-74[179]. These Hubbard U values were: 5.3, 6.5, 5.5 and 6.7 for Co-, Fe-, Mn- and Ni-MOF-74, respectively. The DFT calculations were spin-polarized for all M-MOF-74 frameworks except Mg-MOF-74 and Zn-MOF-74, with starting

magnetic moments that were calculated in a prior work using the optimized Hubbard U values: 2.6, 3.4, 4.3 and 1.7 for Co-, Fe-, Mn- and Ni-MOF-74, respectively[179].

The DFT calculations of all configurations were based on $3 \times 1 \times 1$ supercells of the geometry-optimized M-MOF-74 structure reported by Lee *et al.*[180] A supercell was used so that the forces calculated after metal displacements would not be significantly influenced by metals in neighboring periodic unit cells. The cutoff in the plane wave basis set was 800 eV, Γ-point sampling was used and the wave function energy convergence criterion was set to 10^{-7} eV. Performing our displacements on an equilibrium structure affords us consistency between analogs and confidence that the displacement structures as closely as possible reflect physically reasonable configurations.

Generating Configurations

To generate configurations for our DFT calculations, we displace a single metal atom in the framework and calculate forces on its neighbors. By moving only one metal atom at a time and making the assumption that the forces experienced by framework atoms are strictly pairwise, we are able to estimate the pairwise forces between the metal and the neighboring oxygen atoms.

In prior works, configurations for fitting adsorbate-framework non-bonded potentials were generated by identifying a low-energy pathway in the pore and moving the adsorbate molecule along this pathway[24, 25]. Generating configurations for framework-framework interactions poses a different type of challenge because the framework atoms move less and can explore much less space in the pore than an adsorbate molecule.

We generate 100 configurations per M-MOF-74 analog studied. To make these configurations, we perform a molecular dynamics (MD) simulation of the motion of one metal atom at elevated temperature, using the force field adapted from the work of Duarte *et al.*[58], which is described under the Classical Molecular Simulations subheading. The MD simulation is run for 1 ps between each stored displacement, freezing all atoms except the dummy beads on all CDMs and the displaced metal atom. At each displacement, the position of all dummy beads in the system are optimized such that the system energy is minimized. The classical system must be at the lowest possible energy for this configuration of atomic centers to be accurately compared to the DFT.

Classical Force Calculation

The functional form used to describe metal-oxygen interactions is a Born-Mayer-Huggins + Coulomb potential to account for dispersion and electrostatic interactions, respectively (Eq. 4.1 and Eq. 4.3). The Born-Mayer-Huggins potential was chosen because the exponential term better reproduces *ab initio* repulsive forces compared to the repuslive term in Lennard-Jones potentials[24, 25]. It is common practice to set the parameter σ in the Born-Mayer-Huggins potential to the same value when developing parameters for a series of materials[181], and in this work σ is set to 1.5 Å for metal-O_a, -O_b and -O_c interactions. Metal-metal

interactions are similarly described using a Lennard-Jones + Coulomb potential to account for dispersion and electrostatic interactions, respectively (Eq. 4.2 and Eq. 4.3). Beyond a cutoff distance of 12.0 Å, only electrostatic interactions are accounted for between all pair types.

$$E_{ij} = A_{ij}e^{B_{ij}(\sigma - r_{ij})} - \frac{C_{ij}}{{r_{ij}}^6} + \frac{q_i q_j}{4\pi\epsilon_0 r_{ij}} \qquad \begin{array}{r} r_{ij} \leq 12.0\,\text{Å}, \\ i = M,\ j = O_a,\ O_b\ or\ O_c \end{array} \tag{4.1}$$

$$E_{ij} = 4\epsilon_{ij}((\frac{\sigma_{ij}}{r_{ij}})^{12} - (\frac{\sigma_{ij}}{r_{ij}})^{6}) + \frac{q_i q_j}{4\pi\epsilon_0 r_{ij}} \qquad \begin{array}{r} r_{ij} \leq 12.0\,\text{Å}, \\ i,\ j = M \end{array} \tag{4.2}$$

$$E_{ij} = \frac{q_i q_j}{4\pi\epsilon_0 r_{ij}} \qquad r_{ij} \geq 12.0\,\text{Å} \tag{4.3}$$

For each M-MOF-74 analog studied, we have parameterized the A_{ij}, B_{ij} and C_{ij} terms in Eq. 4.1 for metal-O_a, metal-O_b and metal-O_c interactions. Similarly, we have parameterized the ϵ_{ij} and σ_{ij} terms in Eq. 4.2 for metal-metal interactions. Additional force field terms not parameterized in this work are described below.

Force Decomposition

The force decomposition method detailed here is based on the assumption that the forces experienced by framework atoms are strictly pairwise. While we do not attempt to assess the full implications of this assumption, our results will demonstrate that DFT forces can be reproduced without considering three-body or higher interactions. The procedure for estimating the dispersive pairwise force vector between the displaced metal and its neighbor atoms is as follows:

1. For each configuration structure n_k, a DFT calculation is performed to determine the force on each atom.

2. An additional DFT calculation is performed on structure m, where the displaced metal is moved far from its position in the geometry-optimized structure, effectively removing its interactions with its original neighbor atoms. This procedure will be described in more detail later.

3. For each configuration n_k, the total pairwise force between the displaced metal atom and the neighboring atoms is extracted by assuming that each time a single metal atom is displaced, the force on each atom can be broken down into two parts: interactions with only

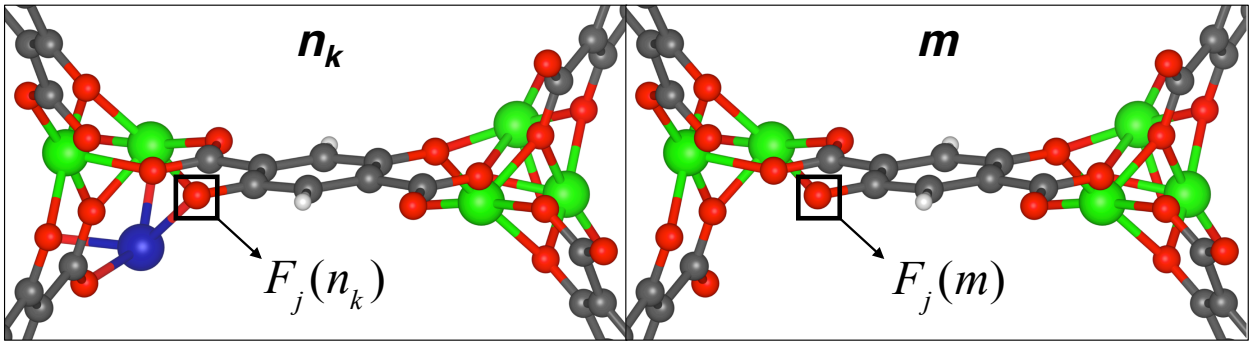

Figure 4.2: Example configurations used for DFT calculations of atomic forces. The displaced metal atom is shown in blue, while other metals, oxygen, carbon, and hydrogen are shown in green, red, grey and white, respectively. The force acting on atom j as a result of interactions with only the rest of the framework $F_j(m)$ is calculated in configuration m, while the force including interactions with the displaced metal $F_j(n_k)$ is calculated in configuration n_k. The pairwise force between the displaced metal and atom j $F_j'(n_k)$ can be estimated from these two calculations.

the displaced metal and interactions with the rest of the framework. For a given atom j at configuration k, we then write: $F_j(n_k) = F_j(m) + F_j'(n_k)$, where the prime denotes the pairwise force vector and $F_j(m)$ represents the interactions of atom j with the rest of the framework. A visual aid for this step is available in Fig. 4.2. This equation is easily rearranged to solve for $F_j'(n_k)$.

4. Having extracted the pairwise forces, we estimate the contributions from electrostatic interactions, as well as the minor contributions resulting from the purely repulsive interactions with dummy beads.[58] The electrostatic forces are calculated using charges determined by Mercado *et al.*[25] The total contributions are subtracted from $F_j'(n_k)$, yielding a final estimate of the dispersive pairwise force vector, $F_j''(n_k)$, between the displaced metal and neighbor atom j.

Two possibilities were considered for system m, where the displaced metal atom is not present. In one case, the displaced metal was completely absent from the calculation and the DFT supercell has a net charge, which was accounted for in VASP by adjusting the total number of electrons and using a neutralizing background charge for Ewald summations. In a second case, the displaced metal is moved to the center of the pore and displaced along the M-MOF-74 c-axis as far as possible from its original position within the DFT supercell. $F_j(n_k)$ and $F_j'(n_k)$ were calculated and extracted in both cases, and the difference between the two sets of estimated forces was negligible. Ultimately, we used the second case of system

m, without a net charge in the DFT supercell.

Pairwise force fitting was not possible for the forces generated from all configurations because upon subtracting the electrostatic contributions, the components of the remaining contributions occasionally were not all aligned with either an attractive or repulsive force vector. For example, for a given configuration being tested the x-component ($F''_{j,x}$) of the estimated metal-oxygen dispersion force vector may point in the direction of an attractive metal-oxygen vector, while the y-component ($F''_{j,y}$) points in the opposite direction. This problem could have two possible sources: **1.** the assumption we make that the metal-oxygen interaction is purely pairwise is not valid for this case, and/or **2.** the electrostatic interactions for this case are not accurately computed by the Mercado *et al.* charges. This case was impossible to fit, and such data were therefore excluded.

Parameter Optimization

We have parameterized the interactions between metals in M-MOF-74 and the oxygen atoms that coordinate directly to them. There are three distinct types of M-MOF-74 oxygen atoms first described in a prior work[24] and displayed again in Fig. 4.3. The carboxylate oxygens, O_a and O_b, are distinguishable by their distance from the phenolic oxygen, O_c.

The A_{ij}, B_{ij} and C_{ij} terms in Eq. 4.1 are optimized to best fit metal-oxygen forces by minimizing the weighted residual sum of squares (RSS) shown in Eq. 4.4.

$$\begin{aligned} RSS = \sum_{j,k} w_k^{gauss}[(F''_{j,x}(n_k) - F_{j,x}^{fit}(n_k))^2 + (F''_{j,y}(n_k) - F_{j,y}^{fit}(n_k))^2 + (F''_{j,z}(n_k) \\ -F_{j,z}^{fit}(n_k))^2] + 3\frac{N_c}{N_t}\sum_{j,k} w_k^{gauss}(||F'_j(n_k)|| - (||F_j^{fit}(n_k) + F_j^{coul}(n_k)||))^2 \end{aligned} \tag{4.4}$$

$F''_j(n_k)$, j and k refer to the estimated dispersive pairwise force vector, atoms and configurations from DFT calculations. $F_j^{fit}(n_k)$ is the dispersive pairwise force vector derived from fitted interaction potentials. The x, y and z subscripts on $F''_j(n_k)$ and $F_j^{fit}(n_k)$ indicate the Cartesian components of the force vector. The weighting parameter w_k^{gauss} is dependent on the pairwise distance sampled at n_k, and takes the form of a Gaussian distribution function centered about the distance r_0, at which the total force is equal to zero, with a standard deviation of 0.5 Å. The $\frac{N_c}{N_t}$ term was included to balance the weighting equally between the component fit and the total force fit, where the total force includes electrostatic contributions. N_c denotes the number of configurations used to fit against components and N_t denotes the number of configurations used to fit against the total force.

The ϵ_{ij} and σ_{ij} terms in Eq. 4.2 are optimized to best fit metal-metal forces by minimizing

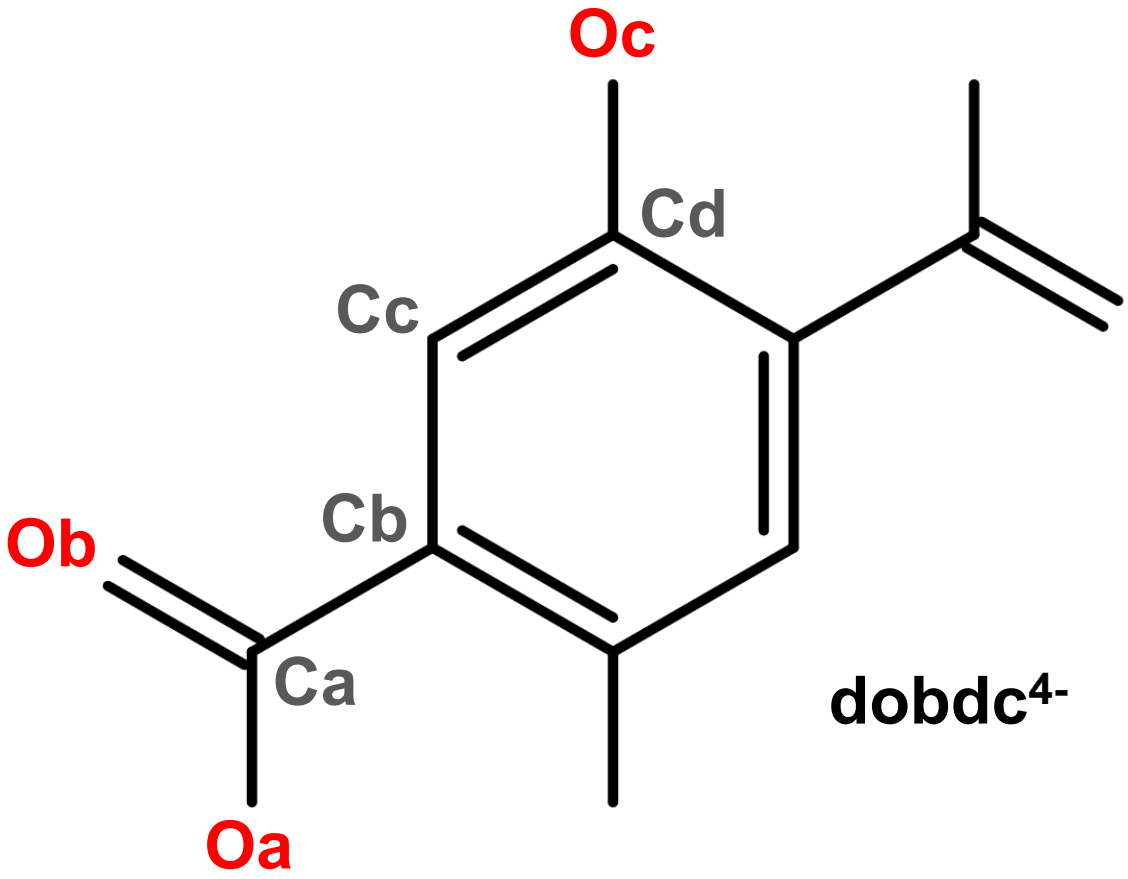

Figure 4.3: The linker molecule in M-MOF-74, dobdc^{4-} = 2,5-dioxido-1,4-benzenedicarboxylate, with atomic labels. Half of the atoms are labeled because the molecule is symmetrical. The interactions between the metal and O_a, O_b and O_c are parameterized in this work.

the weighted RSS shown in Eq. 4.5.

$$RSS = \sum_{j,k} w_k^{skew}[(F''_{j,x}(n_k) - F_{j,x}^{fit}(n_k))^2 + (F''_{j,y}(n_k) - F_{j,y}^{fit}(n_k))^2 + (F''_{j,z}(n_k) - F_{j,z}^{fit}(n_k))^2] \quad (4.5)$$

The terms in Eq. 4.5 are similar to those described above for Eq. 4.4. The weighting parameter w_k^{skew} is a skewed Gaussian distribution function centered about the same distance r_0, with a standard deviation of 4.0 Å and a skew factor $\lambda = 4.0$ [182]. Nelder-Mead optimization as implemented in the SciPy Python library was used for the optimization.

Although the DFT calculations also allow us to extract a total energy change associated with each configuration, it was unfeasible to include energy in the fitting procedure without reparameterizing the metal-carbon interactions. Because the nearest neighbor metal-carbon distances fall well within the cutoff distance for dispersion interactions, they contribute significantly to the total energy associated with configurations, and it was not possible to obtain a converged energy fit without adjusting them. Initially, we attempted to fit metal-carbon interactions as well. However, we observed that the components of the pairwise force vectors and even the pairwise total force vectors before subtracting electrostatic contributions were usually not aligned. We therefore did not fit these interactions, and subsequently were not able to fit to the total energy change.

Upon subtracting the electrostatic contributions, we determined that the attractive part of the metal-oxygen pairwise forces was entirely accounted for by electrostatic interactions, due to the large degree of charge separation between the framework metals and their bonded oxygen neighbors. As a result, for many fitted pairs the C_{ij} terms are frequently zero, although in some cases a nonzero C_{ij} improved the quality of the fits without causing the Born-Mayer-Huggins potential to ever be attractive.

Classical Molecular Simulations

MD simulations in the canonical (NVT) ensemble are used to calculate M-MOF-74 radial distribution functions (RDFs) and pressures of M-MOF-74 analogs at various volumes. Simulations to calculate RDFs were 100 ps long, while pressure calculations were 2 ns long. In both cases, the last 50% of the simulation data were analyzed. All MD simulations were run with a timestep of 1 fs using a Nosé-Hoover thermostat (298 K for simulations of M-MOF-74 analogs and 87 K for simulations of IRMOF-74-V) in the LAMMPS molecular software package[118].

Non-bonded interactions between linker atoms are taken from the Dreiding force field[85]. The bond, angle, dihedral and torsion parameters necessary to describe linker dynamics are also taken from Dreiding. Dreiding Lennard-Jones parameters for carbon and hydrogen are used with geometric mixing rules and the metal-metal interactions determined in this work to compute the non-bonded metal-carbon and metal-hydrogen interactions.

To generate the configurations used for DFT calculations, we rely on a force field based on CDMs parameterized by Duarte *et al.*[58] to model solvated metal cations. This force field will henceforth be referred to as the Duarte *et al.*-adapted force field. The parameters of Duarte *et al.* were used for metal-metal interactions, and geometric mixing rules were used to calculate non-bonded interactions between metals and linker oxygens, carbons and hydrogens with Dreiding Lennard-Jones parameters. This force field also uses Dreiding for bond, angle, dihedral and torsion linker parameters.

Born-Mayer-Huggins, Lennard-Jones and short-range (real space) electrostatic interactions were truncated at 12.0 Å, and Ewald summations were used to calculate long-range electrostatic interactions. For both the fitted and Duarte *et al.*-adapted force fields, M-MOF-

74 point charges were taken from the work of Mercado *et al.*[25] The metal point charges were then distributed between the central metal atom and dummy beads as shown in Fig. 4.1b.

4.3 Reproducing *Ab Initio* Forces with CDM Models

We optimized metal-metal interactions and metal-oxygen interactions in M-MOF-74 to best fit forces calculated via DFT. Fitted force field parameters are available in the Appendices. Our starting point was the Duarte *et al.*-adapted force field described in the Methodology section. Because we extract an estimate of the pairwise force between framework atoms, we are able to reduce the risk of overfitting by only parameterizing metal-metal and metal-coordinating atom interactions, and rely upon well-developed organic molecule force fields for the other interactions.[85] Fig. 4.4, Fig. 4.5, Fig. 4.6 and Fig. 4.7 allow us to assess the quality and success of the force field parameterization procedure.

The panels of Fig. 4.5, Fig. 4.6 and Fig. 4.7 show the agreement between the *ab initio* metal-O forces. The solid lines show the parameterized force functions fit to the *ab initio* force data, shown as squares, while the dashed lines represent the Duarte *et al.*-adapted force functions. In all cases, the parameterized force functions more accurately reproduce the DFT data, and the Duarte *et al.*-adapted force functions consistently underpredict the minimum energy distance of the metal-oxygen interaction. The minimum energy distance corresponds to the distance at which the force is zero - usually between 1.8 and 1.9 Å. The closer the metal-oxygen pair distance sampled by a given configuration is to the minimum energy distance of the metal-oxygen interaction, the higher the weighting of this configuration. Because of this weighting procedure and the fact that the sampled distances have a hard lower bound due to repulsive interactions, the fitted potential reproduces the DFT forces at smaller distances better than at larger distances. As a result, the fitted potential deviates from the DFT forces at large distances, while the small distance data is generally fit accurately.

Fig. 4.4 displays the weighted RSS for metal-metal interactions against the distance between a pair of metal atoms. Each square corresponds to an RSS value calculated at a tested configuration. By displaying the weighted RSS values for both the fitted force field, shown in blue, and the starting point, shown in red, we can demonstrate the improvement in the fit. The peaks in data of each panel of Fig. 4.4 reflect the correlation of the weighted RSS to the skewed Gaussian weighting function, which is plotted as a black dashed line. In all cases, the fitted force field parameters for metal-metal interactions show markedly better agreement with DFT forces.

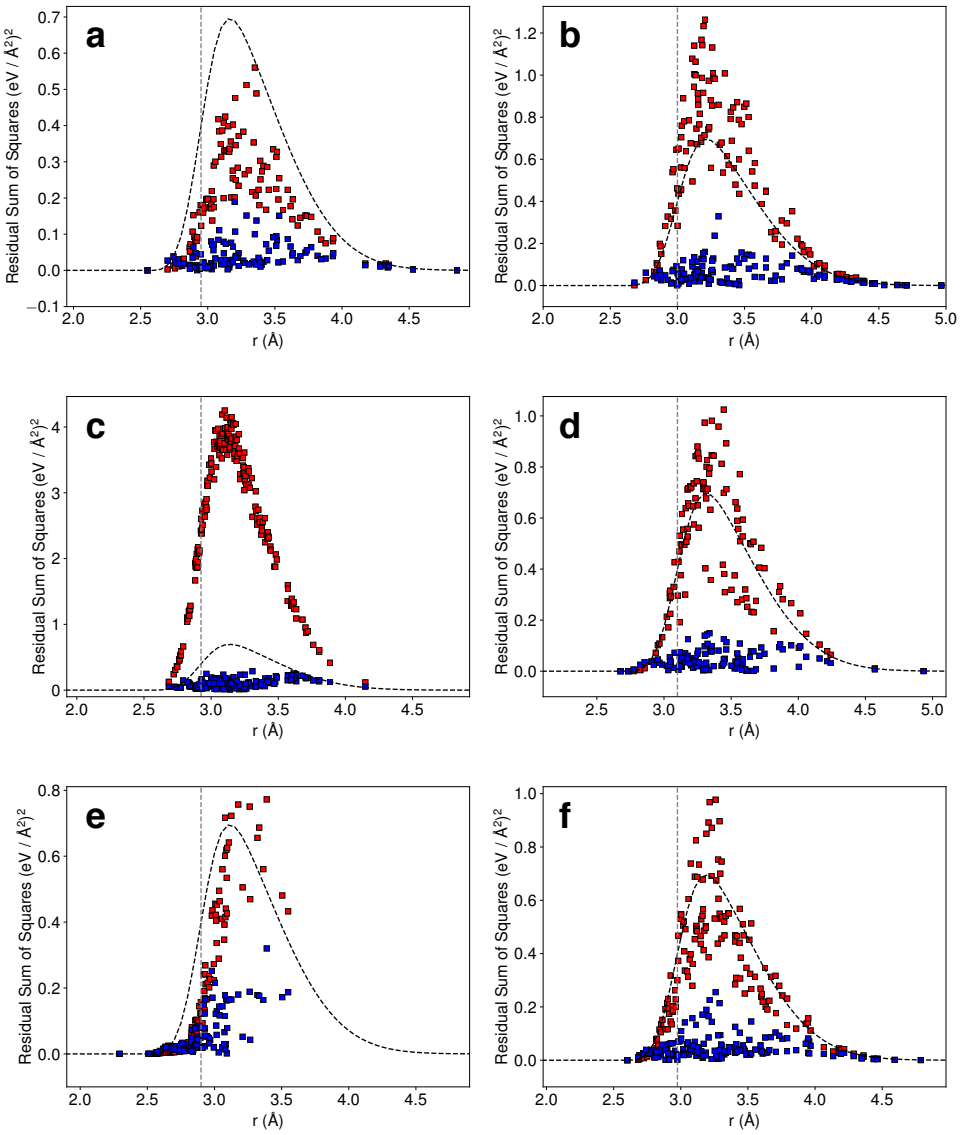

Figure 4.4: The weighted residual sum of squares (RSS) between the force field force vectors and the DFT force vectors resulting from metal-metal interactions in Co-, Fe-, Mg-, Mn-, Ni- and Zn-MOF-74 are shown in panels (a), (b), (c), (d), (e) and (f), respectively. The Duarte *et al.*-adapted RSS values are plotted as red points, while the fitted RSS values are plotted as blue points. Each square point represents an RSS value calculated based on a force vector resulting from a given configuration. The black dashed curve is the skewed Gaussian weighting function with skew factor $\lambda = 4.0$ and standard deviation 4.0 Å. The energy minima determined from the DFT calculations is plotted as the grey dashed vertical line.

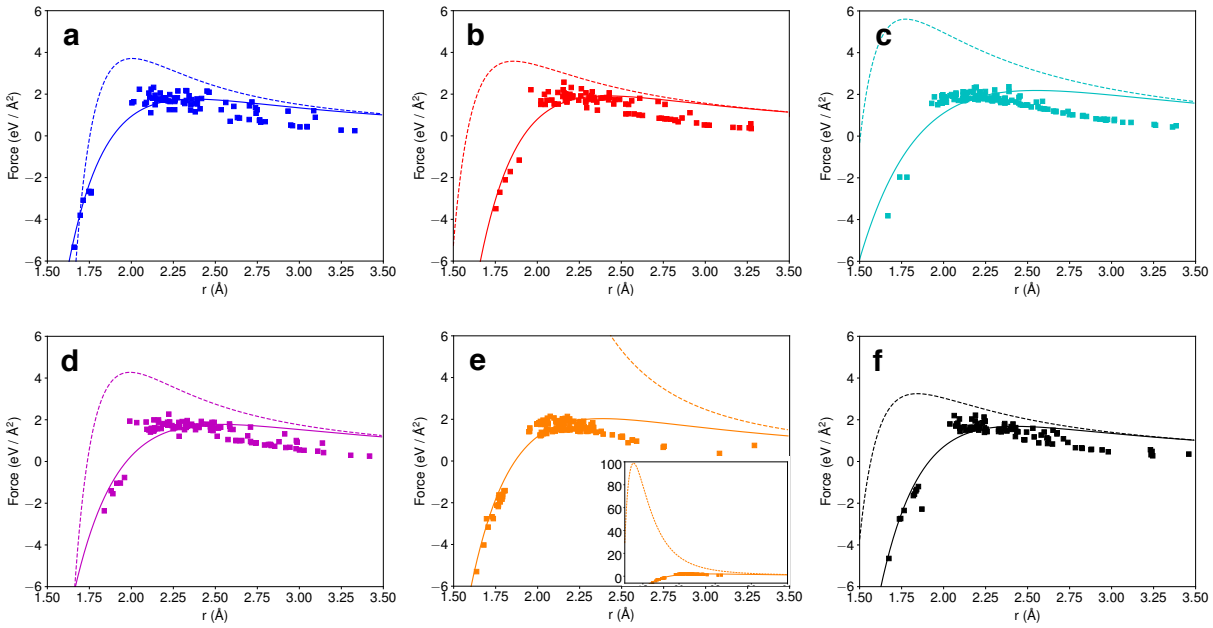

Figure 4.5: Panels (a)-(f) show how the estimated metal-O_a forces from *ab initio* calculations are reproduced by the parameterized Born-Mayer-Huggins + Coulomb potential. Panels (a), (b), (c), (d), (e), and (f) show data for Co-, Fe-, Mg-, Mn-, Ni-, and Zn-MOF-74, respectively. The distance is the distance between a metal-O_a pair. The squares each represent a different system configuration used for a DFT calculation, and the solid lines represent the fitted force functions, while the dashed lines represent the Duarte *et al.*-adapted force functions. The inset of panel (e) shows the full range of the forces predicted by the Duarte *et al.*-adapted parameters, which are extremely far from the DFT-predictions.

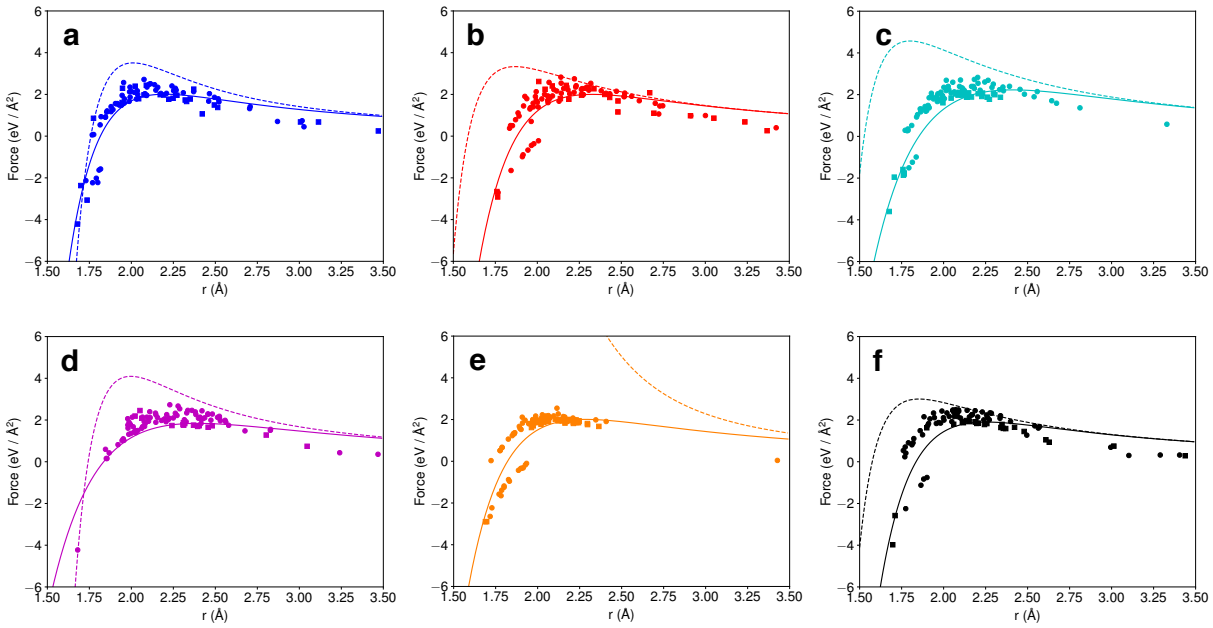

Figure 4.6: Panels (a)-(f) show how the estimated metal-O_b forces from *ab initio* calculations are reproduced by the parameterized Born-Mayer-Huggins + Coulomb potential. Panels (a), (b), (c), (d), (e), and (f) show data for Co-, Fe-, Mg-, Mn-, Ni-, and Zn-MOF-74, respectively. The distance is the distance between a metal-O_b pair. The squares each represent a different system configuration used for a DFT calculation, and the solid lines represent the fitted force functions, while the dashed lines represent the Duarte *et al.*-adapted force functions.

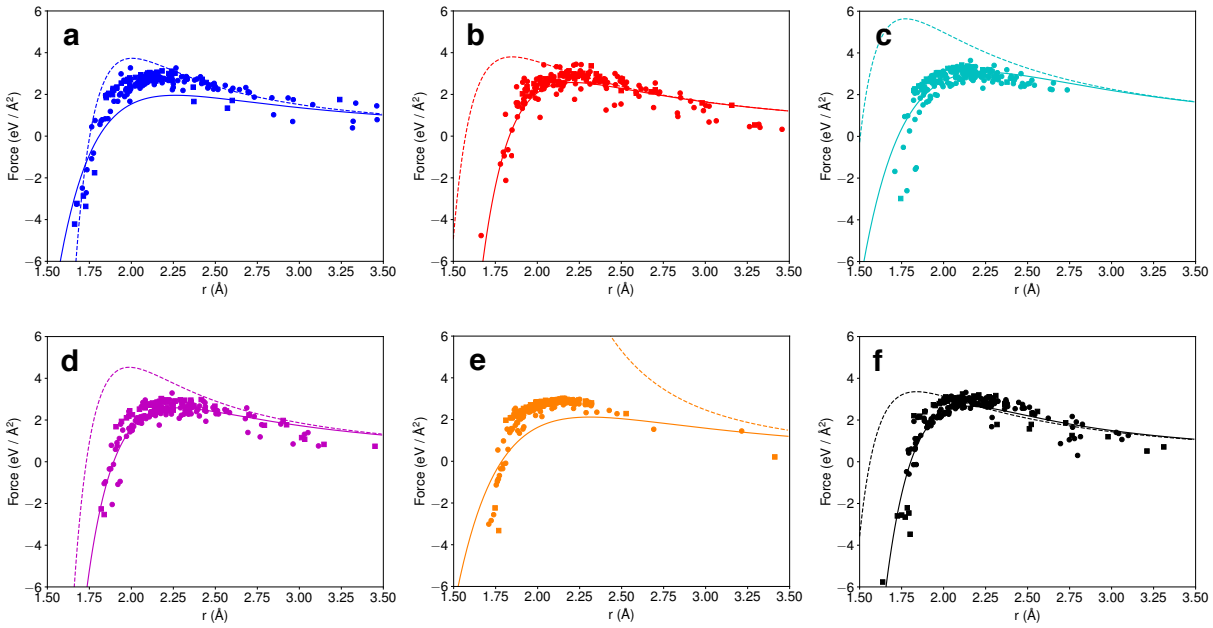

Figure 4.7: Panels (a)-(f) show how the estimated metal-O_c forces from *ab initio* calculations are reproduced by the parameterized Born-Mayer-Huggins + Coulomb potential. Panels (a), (b), (c), (d), (e), and (f) show data for Co-, Fe-, Mg-, Mn-, Ni-, and Zn-MOF-74, respectively. The distance is the distance between a metal-O_c pair. The squares each represent a different system configuration used for a DFT calculation, and the solid lines represent the fitted force functions, while the dashed lines represent the Duarte *et al.*-adapted force functions.

4.4 Validation: Geometric Properties

Fig. 4.8 shows metal-metal and metal-oxygen radial distribution functions (RDFs) for all M-MOF-74 analogs simulated using both the fitted and Duarte *et al.*-adapted force fields. Both force fields can be compared to the RDF calculated using the DFT optimized structures at 0 K, which is shown as a dashed black line. In many cases, the force field RDF curves at 0 K coincide with the 0 K DFT peaks, meaning that the equilibrium distance in the metal-metal and metal-oxygen interactions as predicted by DFT is also captured by the force field. In other cases, the force field RDF curves are offset from 0 K DFT peaks, meaning that the equilibrium distances as predicted by DFT are either over- or under-predicted by the force field.

The Duarte *et al.* force field was parameterized to model solvated metal cations and was never intended to be used to model MOFs. As a result, the reasonable RDFs that result from many of the Duarte *et al.*-adapted force fields are quite impressive and indicate that the frameworks remain intact when simulated at 298 K, as is shown in Fig. 4.9. The fact that most of the frameworks remain intact is therefore a testament to the adaptability of CDMs. We will later take advantage of this adaptability to model a larger analog of M-MOF-74. A notable exception to the relative success of the Duarte *et al.*-adapted force field is the Ni-MOF-74 analog. When the Ni-MOF-74 analog is annealed using the Duarte *et al.*-adapted force field, the framework falls apart after the metals cluster together unphysically. This feature can be observed in Fig. 4.9i.

A close examination of the metal-metal RDFs in Fig. 4.8 shows that the fitted force field captures the DFT-predicted equilibrium distance as well or better than the Duarte *et al.*-adapted force field for all M-MOF-74 analogs except Mn-MOF-74. In the case of Mn-MOF-74, the fitted force field equilibrium distance is incrementally farther off from the DFT distance than that which is predicted by the Duarte *et al.*-adapted force field. Both force fields, however, predict equilibrium distances that are within 0.1 Å of the DFT prediction.

An examination of the metal-oxygen RDFs shows that the fitted force field is able to capture a separation in the first peak that is predicted by DFT for the Mn- and Zn-MOF-74 analogs but missed entirely by the Duarte *et al.*-adapted force field. This is a result of the fact that metal-O_a, -O_b and -O_c interactions are fitted separately, and thus the slightly different equilibrium distances can be captured by the fitted force field parameters. The separation in the first peak becomes less apparent but is still visible for some analogs when the frameworks are simulated at 298 K, as is seen in Fig 4.9. The equilibrium metal-oxygen distances, accounting for the separation in the first peak by averaging, predicted by the fitted force field are always in better agreement with the DFT predictions than the Duarte *et al.*-adapted force field.

To perform both our fitting procedure and our MD simulations, we assume constant charges on the metals and the linker atoms. In reality, the charges on the metals and linkers depend on the metal position. When the metals are displaced such that they form longer coordination bonds with linker oxygens, the charge separation between the metals and linker atoms will increase, and the attractive electrostatic force between metals and oxygens will

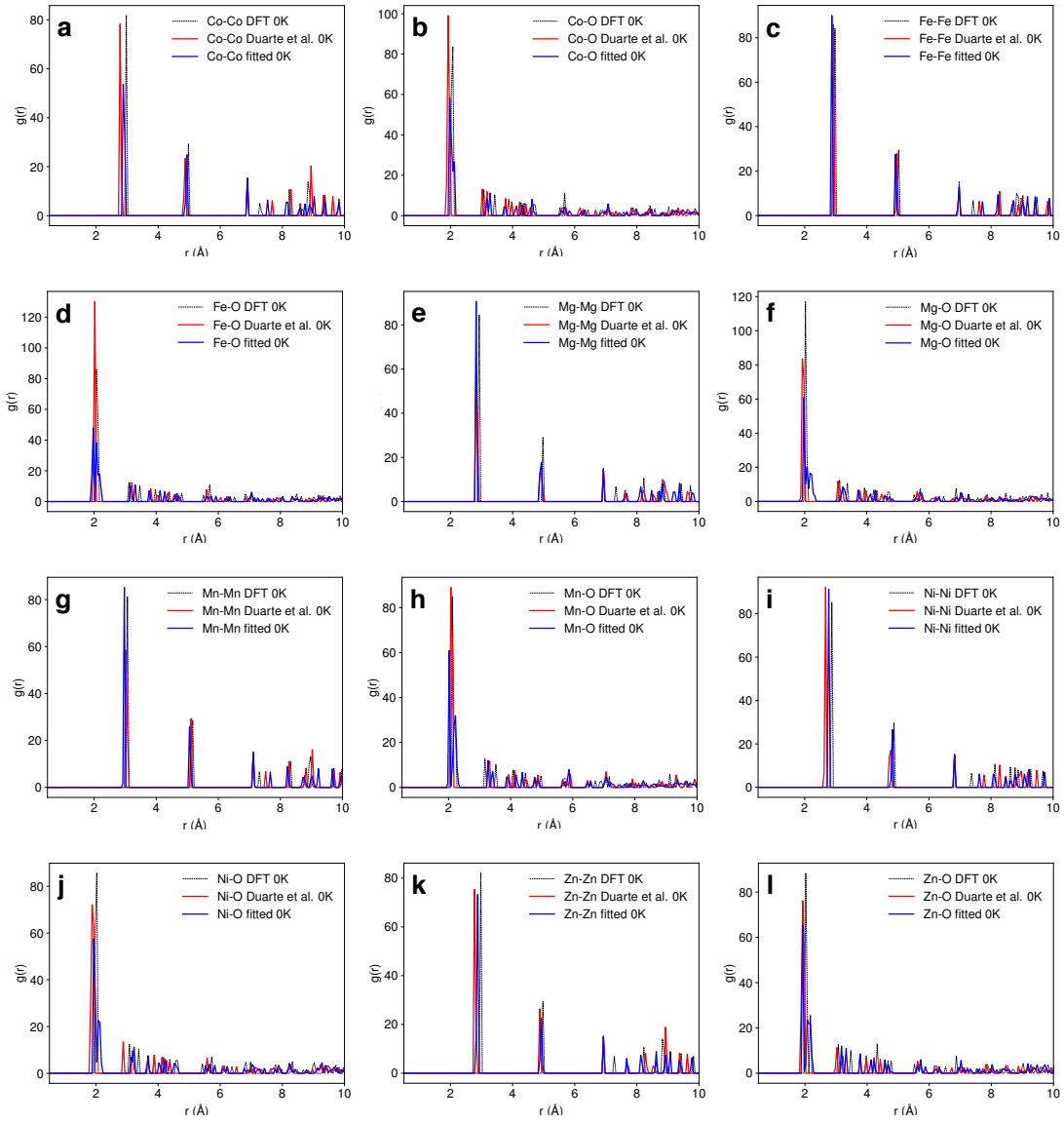

Figure 4.8: The metal-metal radial distribution functions (RDFs) resulting from the force field-predicted 0 K structures of Co-, Fe-, Mg-, Mn-, Ni- and Zn-MOF-74 are shown in panels (a), (c), (e), (g), (i) and (k), respectively. The metal-oxygen RDFs resulting from force field-predicted 0 K structures of Co-, Fe-, Mg-, Mn-, Ni- and Zn-MOF-74 are shown in panels (b), (d), (f), (h), (j) and (l), respectively. The fitted force field RDFs are plotted in blue, while the Duarte *et al.*-adapted force field RDFs are plotted in red. The RDF calculated from the DFT optimized structure at 0 K is plotted as a black dashed line and is included to facilitate comparisons between the predictions.

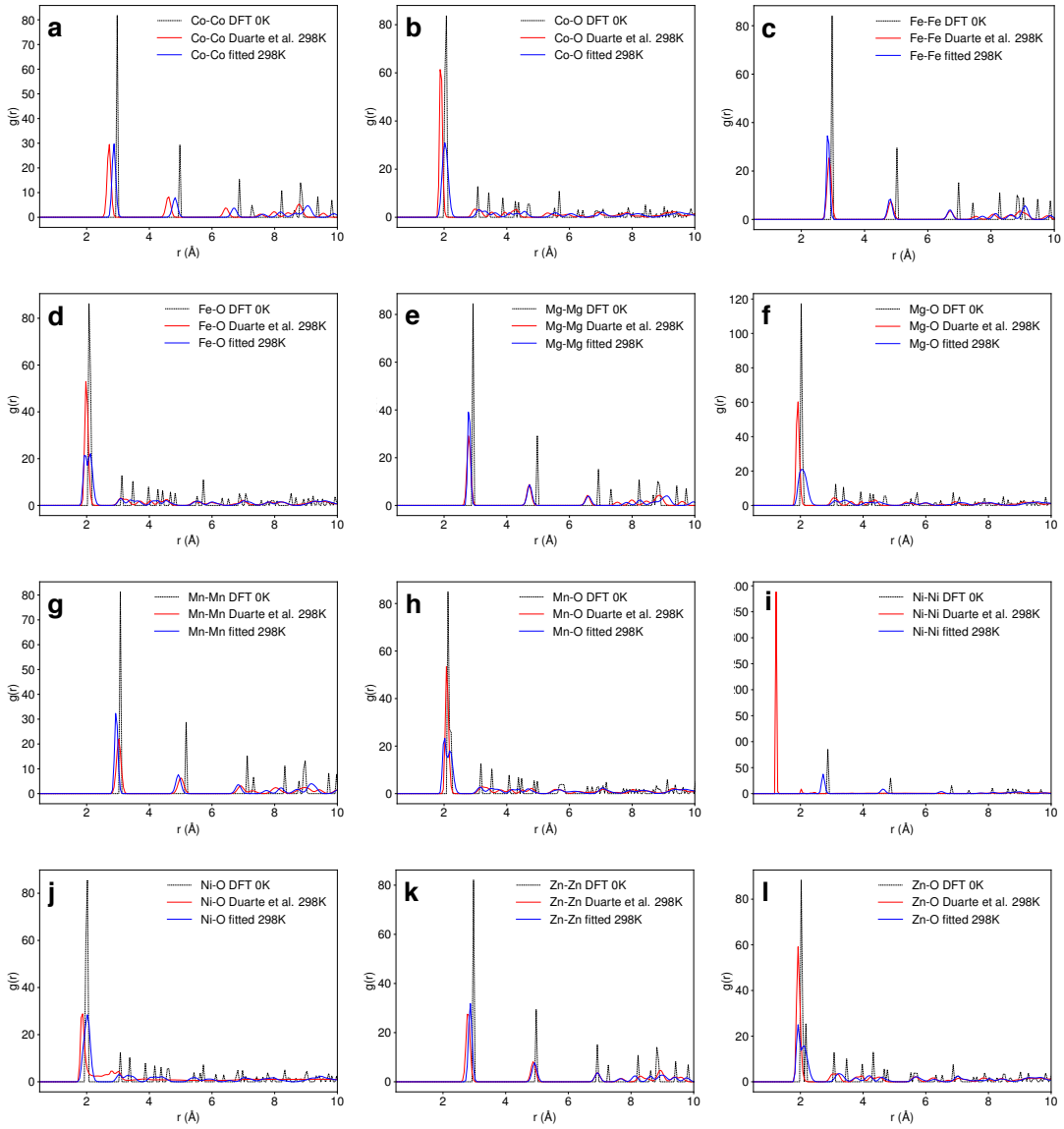

Figure 4.9: The metal-metal radial distribution functions (RDFs) resulting from the force field-predicted 298 K structures of Co-, Fe-, Mg-, Mn-, Ni- and Zn-MOF-74 are shown in panels (a), (c), (e), (g), (i) and (k), respectively. The metal-oxygen RDFs resulting from force field-predicted 298 K structures of Co-, Fe-, Mg-, Mn-, Ni- and Zn-MOF-74 are shown in panels (b), (d), (f), (h), (j) and (l), respectively. The fitted force field RDFs are plotted in blue, while the Duarte *et al.*-adapted force field RDFs are plotted in red. The RDF calculated from the DFT optimized structure at 0 K is plotted as a black dashed line and is included to facilitate comparisons between the predictions.

	Co-MOF-74	Fe-MOF-74	Mg-MOF-74	Mn-MOF-74	Ni-MOF-74	Zn-MOF-74
B	22.78	27.71	12.47	25.46	22.22	29.76
G	3.75	4.38	3.47	3.59	3.84	4.30
B/G	6.07	6.33	3.59	7.09	5.79	6.92
Y	10.66	12.47	9.54	10.28	10.89	12.31
Y_x	33.07	35.18	27.16	26.58	29.49	34.60
Y_y	7.88	14.59	15.30	9.67	8.86	9.72
Y_z	7.82	15.93	13.51	9.86	8.04	10.44

Table 4.1: Bulk (B), shear (G), orientationally-averaged and components of the Young's (Y) moduli are reported for M-MOF-74 (M = Co, Fe, Mg, Mn, Ni, Zn) in GPa. The unitless measure of ductility (B/G) is also reported.

likewise increase. When the metals are displaced far enough from the linker oxygens that they start to resemble neutral metals, the attractive electrostatic interactions will likely decrease. Thus, we might *a priori* expect our method, which neglects these effects, to fit potentials for metal-oxygen interactions that are too attractive beyond the equilibrium distance but are within the coordination bond range (around 2.5-3.0 Å), and too repulsive at larger distances. We do not see an effect of this limitation on the RDFs shown in Fig. 4.8, possibly because our Gaussian weights focus our fitting efforts on the vicinity of the equilibrium distance. Because the metal-oxygen distances sampled in MD simulations are generally close to the equilibrium distance, the forces effective in the simulation stay within the accurately parameterized range.

4.5 Validation: Mechanical Properties

We have computed the elastic properties of M-MOF-74 modeled using our fitted force field parameters. These properties are presented in Table 4.1. The bulk moduli B predicted here can be compared to bulk moduli reported for other frameworks. The B that we predict for M-MOF-74 are of a similar range as has been predicted for MOF-5 by force field and DFT-based approaches, as well as has been measured by experiment[183]. The predicted M-MOF-74 B are, however, lower than the predicted and measured bulk moduli of HKUST-1 and UiO-66[183]. As all of these frameworks are generally considered to be quite rigid[184, 185], we find the fitted force field predictions to be in line with our expectations. The shear moduli G predicted here are not exceptionally high, but are well within the range of the experimentally measured values for rigid MOFs[184]. This is not surprising, as any indication of an easily accessible shear mode for M-MOF-74 without adsorbates would have been unprecedented.

Table 4.1 also reports the Young's moduli (Y) predicted by the fitted force field in all M-MOF-74 analogs. In the elastic moduli calculations, the x-axis corresponds to M-MOF-74 crystallographic c-axis, which is well known as the axis in which the one-dimensional rods are oriented[37]. These one-dimensional rods are particularly rigid components. As expected,

	B	G	Y
Co-MOF-274	**5.19**	**1.62**	**4.41**
Co-MOF-274	8.51	2.55	6.95
Fe-MOF-274	**6.00**	**1.90**	**5.17**
Fe-MOF-274	9.69	3.19	8.63
Mg-MOF-274	**5.30**	**2.40**	**6.25**
Mg-MOF-274	10.05	3.32	8.97
Mn-MOF-274	**5.66**	**1.96**	**5.27**
Mn-MOF-274	11.98	2.28	6.42
Ni-MOF-274	**5.70**	**1.93**	**5.21**
Ni-MOF-274	—	—	—
Zn-MOF-274	**7.00**	**2.26**	**6.11**
Zn-MOF-274	10.28	2.48	6.89

Table 4.2: Bulk (B), shear (G) and orientationally-averaged Young's (Y) moduli are reported for M-MOF-274 (M = Co, Fe, Mg, Mn, Ni, Zn) in GPa, computed both with this force field and by Lee *et al*[186]. The data for the fitted force field are shown in bold to differentiate from the *ab initio* Lee *et al.* computed moduli, which do not include Ni-MOF-274.

the x-components of the predicted Y are particularly high, both compared to the predicted y- and z-components as well as the general range of elastic moduli predicted for MOFs. We have established in a prior work that an extended analog of Mg-MOF-74 can deform in a way that changes the crystal symmetry of the framework[173]. The deformation is associated with structural changes that take place in the *ab*-plane, orthogonal to the direction of the one-dimensional rods and hexagonal channels[37, 173]. We might therefore expect the y- and z-components of Y to be relevant to this deformation, as the metal-oxygen distances in the *ab*-plane must change to accommodate the deformation pattern[173]. From the Y reported in Table 4.1, M-MOF-74 analogs synthesized from Mg do not appear to be more likely to deform than any other analogs, as the Y_y and Y_z values for Mg-MOF-74 are actually the largest of the series. Based on this prediction, M-MOF-74 analogs synthesized from any metal may be susceptible to deformation. This prediction is consistent with the experimental observation of adsorbate-induced Co-MOF-74 deformation[126].

Recently, Lee *et al.* computed the elastic moduli of an extended framework analog, M-MOF-274 (M = Co, Fe, Mg, Mn, Zn)[186]. We have applied our M-MOF-74 force fields to the same series, and are thus able to test the transferability of our force field fitting procedure. A comparison of any of the three M-MOF-274 elastic moduli reported in Table 4.2 to their corresponding values reported in Table 4.1 leads us to the conclusion that the extended analogs are all less rigid than their smaller-pore counterparts. This result can be rationalized by the fact that the linker in M-MOF-274 has two aromatic rings rather than one, and these rings are connected by a bond which imparts extra flexibility to the structure.

By comparing our elastic moduli to the Lee *et al. ab initio* computed moduli, we are also

able to assess the accuracy of our predictions. The force field B values are in general a factor of two off from the *ab initio* predictions, with the best and worst agreement corresponding to Co- and Mn-MOF-274. The fact that the classical model consistently underpredicts B may indicate a systematic error, such as insufficiently rigid linker parameters, which were taken from the Dreiding force field and not parameterized in this work. The force field G and Y values also similarly undershoot the *ab initio* predictions, but with even smaller margins of error. Overall, the level of agreement between the force field and *ab initio* predictions are good, especially considering the fact that linker bonded and linker-linker nonbonded interactions were explicitly not parameterized in this work. We therefore conclude that the force field model accurately describes metal-oxygen nodes and that the force field parameterization procedure is transferable to extended M-MOF-74 analogs.

4.6 Structural Transitions in M-MOF-74 Series

We have applied our fitted force field for Mg-MOF-74 to the system in which we previously established the M-MOF-74 extended linker series deformation pattern: IRMOF-74-V (Mg) with adsorbed argon. The complex deformation is characterized and can be accessed by a decrease in the equivalent a and b lattice parameters[173]. To study the free energy of the deformation, we then performed NVT simulations of this system while recording the instantaneous hydrostatic pressure at different a and b lattice parameters. By leaving all other simulation cell parameters unchanged, we have assumed that a hydrostatic external pressure will have no effect on the c lattice parameter or on the triclininc box angles. The Helmholtz free energy at a given volume, which is related to the a and b unit cell parameters, is[187]:

$$F(V) - F(V_0) = -\int_{V_0}^{V} \langle P_i(V') \rangle dV' \tag{4.6}$$

In Eq. 4.4, V_0 is set to be the volume of the simulation found to have the lowest free energy, and P_i is the instantaneous hydrostatic pressure. Fig. 4.10a shows the average hydrostatic pressure as a function of volume, which is implicitly a function of the equivalent a and b lattice parameters. Fig. 4.10b shows the free energy of IRMOF-74-V, calculated using Eq. 4.6, as a function of volume both with and without adsorbed argon in the pores. We performed simulations at multiple argon adsorbate loadings, only one of which, marked with black and cyan circles, induces the structural transition. The cyan-black color spectrum used for the system with 486 argon per channel represents the extent of deformation observed, which is quantified by the order parameter calculated in Eq. 4.7.

$$OP = \frac{1}{N_a} \sum_{a} \left\langle \frac{1}{\mid \theta_i - 120^\circ \mid +1} \right\rangle \tag{4.7}$$

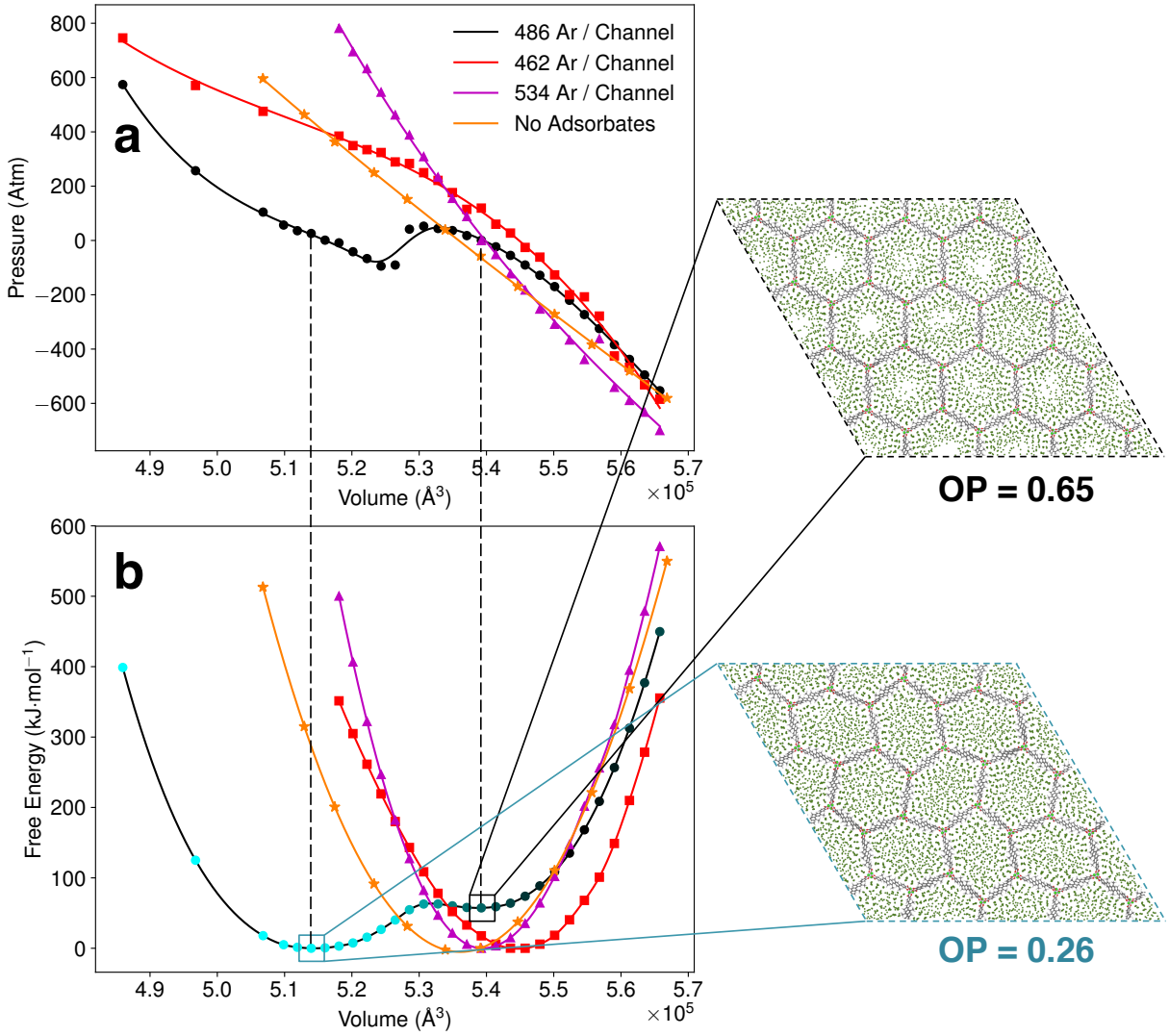

Figure 4.10: (a) Average hydrostatic pressures resulting from simulations of IRMOF-74-V with adsorbed argon at different volumes modeled using the fitted force field and (b) the free energy profile as a function of volume for the aforementioned system, calculated using the pressures in panel (a) and Eq. 4.4. Panel (b) also shows the free energy profile for bare IRMOF-74-V as a function of volume, which is plotted in orange while the data for the systems with adsorbates are plotted in black, magenta and red. The magenta and red curves show data for the framework with slightly more and slightly less adsorbates than the deformed lattice system. Visualizations show snapshots of IRMOF-74-V with adsorbed argon simulated at both the system's free energy minimum and the volume corresponding to the free energy minimum of the bare framework. In both panels (a) and (b), the plotted curves are spline functions fitted to the simulation data points, shown as markers, and are included as a guide to the eye. The cyan-black color spectrum for the deformed lattice system shows the extent of deformation quantified by Eq. 4.7, where cyan means more deformed.

In Eq. 4.7, the sum is performed over all interior angles of the hexagonal channels, where the vertices are determined by calculating the center-of-mass of each one-dimensional metal rod (metal helix). N_a is the number of interior angles, and θ_i is the instantaneous measured value of the interior angle. When the interior angles approach 120°, the hexagons are more regular and the order parameter is closer to 1.0. Similarly, when the hexagon is more deformed and the interior angles deviate from 120°, the order parameter is closer to 0.0. In this study, the order parameter ranged from 0.25 at low volumes to 0.65 at the bare framework stable volume. The plotted colored and black curves are fitted spline functions and are intended to guide the eye.

An examination of the free energy of the system with 486 argon per channel, plotted in black, and a comparison to its bare counterpart leads us to several conclusions. Most notably, there are two free energy minima in the system with 486 argon per channel - a global minimum and a local minimum - while the bare system has only one minimum. The global minimum in the argon system is shifted to a smaller volume. This global minimum corresponds to a framework exhibiting the deformation pattern as previously reported. At the local minimum, which occurs at a volume similar to the empty framework minimum, the framework structure exhibits the standard undeformed hexagonal channels. By contrast, the bare framework has no feature other than a parabolic free energy profile, meaning that the observed deformation pattern is not accessible by pressure alone.

The local minimum in the deformed system occurs at a slightly larger volume. The local minimum volume is therefore evidence of framework swelling upon argon adsorption. This conclusion is supported by the shift of the free energy minimum volume of the system with 462 argon per channel, which occurs at a significantly larger volume than the bare system. In our prior work, which relied on the Duarte *et al.*-adapted force field, we noted that the unit cell parameters measured below the deformation loading changed much more during the simulated argon adsorption process compared to the experiment[173]. It is therefore interesting to note that after the tailored fitting procedure was applied, the framework still appears to be more prone to swelling than was reported in an experimental argon adsorption study in the Mg-MOF-74 series[99].

We can compare the behavior of the systems with slightly more and slightly less adsorbates necessary for the lattice deformation, displayed in Fig. 4.10b in magenta and red, respectively with the deformed system. This comparison allows us to confirm that our force field captures the expected sensitivity of the deformation. In both our prior work and the experimental adsorption study featuring *ortho*-xylene as an adsorbate, the unit cell parameter associated with the lattice deformation only decreased in a small range surrounding the loading of interest[173, 99]. In the case of argon, the loading of interest is associated with the pore being close to filled, but not yet saturated. Intra-channel interactions between adsorbates at these conditions favor argon droplet formation, with the caveat that argon is adsorbed to the walls of the framework. The complex deformation pattern occurs because it allows the structure to shrink, allowing an argon droplet to form, and is stabilized by the presence of the adsorbate. At higher loadings, the deformation pattern would compress the adsorbed argon overmuch such that it is no longer stabilized. Because the magenta and red

curves both have only one free energy minima, we see that also in this work we only predict stable deformation in a small range of adsorbate loadings.

Recently, Vanduyfhuys *et al.* described expected experimental responses to stimuli with the shapes of flexible framework free energy profiles as a function of volume[187]. By their descriptions, IRMOF-74-V loaded with argon is a triggered disperser, meaning that while the smaller-volume structure is the true free energy minimum, both minima are mechanically stable. This implies that changes in the framework structure will be irreversible, and fluctuations large enough to drive the system over the free energy barrier separating the two minima will result in at least a metastable structure.

The same free energy analysis was performed using the Duarte *et al.*-adapted force field, with the results presented in Fig. 4.11. The importance of the tailored force field parameters is immediately apparent upon comparison of the free energy profiles resulting from the fitted and Duarte *et al.*-adapted parameters. The Duarte *et al.*-adapted model displays both qualitatively and quantitatively different behavior. There is only one free energy minimum, as opposed to two in the fitted model. This leads us to the conclusion that a free energy barrier between the deformed and non-deformed states is somehow absent from the Duarte *et al.*-adapted model, implying that the subtle differences in metal-metal and metal-oxygen bond energies are sufficient to influence large scale structural properties in the crystal. In addition, the location of the minimum predicted by the Duarte *et al.*-adapted model is shifted from either of the minima in the fitted model. This is unsurprising, considering the fact that the metal-oxygen RDFs predicted by the two force fields for Mg-MOF-74 do not overlap, as can be seen in Fig. 4.8f and Fig. 4.9f.

Applying the description of Vanduyfhuys *et al.* to the free energy profile predicted by the Duarte *et al.*-adapted force field leads to different predictions about the response of the IRMOF-74-V + argon system to pressure. Because the Duarte *et al.*-adapted force field predicts no free energy barrier between the deformed and non-deformed crystal structures, the transition between these states is thermodynamically reversible, and the model is classified as an ideal spring: both the framework and the environment can return to their original states after a pressure-induced structural change. The key differences between the models provide further motivation for our goal to make tailored force fields to describe metal interactions in MOFs, as it seems that the deformation is sensitive enough to the force field parameters to display qualitatively different behavior.

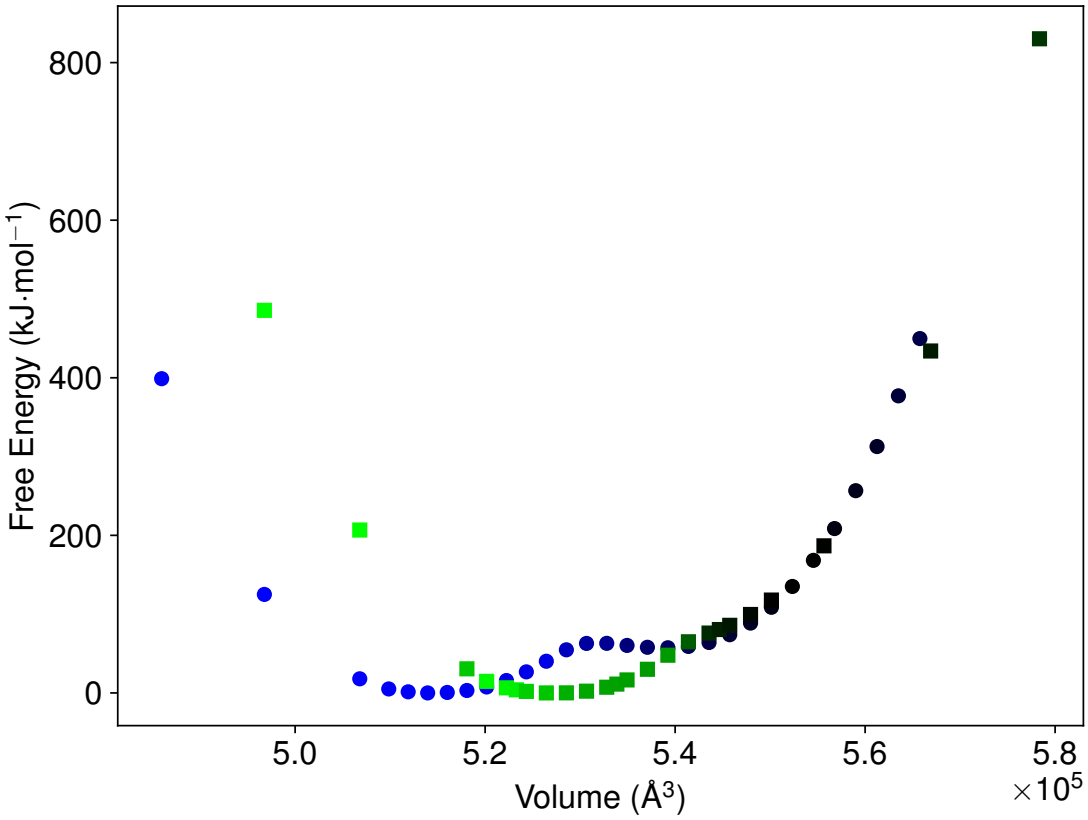

Figure 4.11: The free energy profile as a function of volume for the IRMOF-74-V (Mg) system with 486 argon per channel, modeled using both the Duarte *et al.*-adapted force field (black and green squares) and the force field developed in this work (blue and black circles). The blue and green colors indicate extent of deformation, defined by the order parameter in Eq. 4.7. This plot overlays the two sets of data in order to highlight the major differences between the free energy profiles: 1) the fitted force field shows two free energy minima, while the Duarte *et al.*-adapted force field shows one. Thus, the predicted free energy barrier between the deformed and undeformed states is somehow absent in the Duarte *et al.*-adapted model, implying that the deformation is sensitive enough to the metal-metal and metal-oxygen force field parameters to display qualitatively different behavior; 2) the minima predicted by the different models occur at different volumes.

4.7 Conclusion

We have developed force fields that for the first time allow us to reproduce *ab initio* forces towards modeling framework flexibility in M-MOF-74. Due to the similarity of the metal-oxygen nodes across the M-MOF-74 extended linker series and the fact that our force fields are specifically parameterized to capture the chemistry at these nodes, our force fields are inherently transferable to systems containing octahedrally coordinated M-O secondary building units (SBUs). We have used these force fields to better understand the thermodynamics of structural transitions in an extended linker analog of Mg-MOF-74. We have found that the previously reported deformation pattern in IRMOF-74-V is truly adsorbate-induced and cannot be accessed purely by external pressure changes. The force field parameterization method presented here is in no way specific to the M-MOF-74 structure and can be easily applied to other MOFs. Importantly, force fields based on CDMs use purely non-bonded potentials to capture coordination chemistry and therefore have the ability to capture bond breakage and formation. We believe our findings provide a strong motivation for further efforts in combining MOF force fields with accurate solvent models such that CDM-based force fields can be used to study complex problems such as defects and crystal growth. Future work should include reconciling the use of framework-specific charges typically present in MOF studies with the full metal ion charges used in the parameterization of accurate metal-solvent force fields.

Chapter 5

Conclusions

The sheer number of synthesizable (tens of thousands) and hypothetical (hundreds of millions) of MOFs makes them an exciting class of materials to consider for an extraordinarily wide range of applications[17, 18, 19]. A number of outstanding challenges still face the MOF community, however, and include our lack of knowledge about MOF formation. We need to understand how MOFs form such that we can rationally design synthesis conditions to maximize yield of the desired product. We also need to be able to control features such as crystal aspect ratio and size, both of which have been shown to be important for the implementation of MOF crystallites in adsorption-based applications[188, 189]. Finally, as the community increasingly considers using MOFs as materials for liquid-based separations, such as water purification and pervaporation[190, 191], a stronger mechanistic understanding of how liquids order and diffuse in MOFs is required. In this thesis, I have sought to address these fundamental gaps in knowledge by performing molecular simulation studies and developing new computational tools.

5.1 Summary of Projects

In Chapter 2, we used for the first time a model without explicit bonding interactions between metals and coordinating linker atoms to study an analog of M-MOF-74: IRMOF-74-V (Mg). We sought to understand the origin of an intriguing signal in experimental SAXS profiles. Our results were unexpected: we ruled out a proposed experimental mechanism that used long-range ordering of argon atoms as its basis. Not only did we find no thermodynamic justification for such a phenomenon, we also discovered a unique deformation pattern of the M-MOF-74 series. These findings also had implications for the rest of this thesis, as the novelty of the results demonstrated the versatility and validity of the nonbonded approach to describing coordination bonds, referred to in this text as the Cationic Dummy Model (CDM)-based approach.

In Chapter 3, we studied the dynamics of xylene isomers in MOF-5. Both translational and rotational diffusion of xylenes were quantified and compared to complementary

experimental data that were measured by NMR. We made an interesting discovery: while *para*-xylene has the fastest translational motion, it experiences the slowest rotational motion. The rotational activation energy barrier for *para*-xylene is also higher than for the other two isomers. This observation is notable because in bulk, the rotational activation energy barriers for all xylenes are the same. A deeper computational analysis revealed that the shape of *para*-xylene causes it to be more rotationally constricted than the other two isomers due to intermolecular interactions between the xylene and the aromatic group of the MOF linker. These findings have implications for the rational design of MOFs for liquid-phase xylene separations.

In Chapter 4, we sought to make the CDM-based approach for studying coordination complexes directly applicable to MOFs by developing a methodology for parameterizing CDM-based MOF force fields from *ab initio* quantum chemistry calculations. We demonstrated that our approach yields models for the M-MOF-74 series that are stable, and that result in simulated structural properties that are in good agreement with quantum chemistry calculations. We demonstrate the importance of using tailored CDMs by computing free energies of the structural transition described in Chapter 2 and showing that different models can lead to qualitatively different free energy landscapes. The long-term implications of this work lie in the development of a novel methodology for parameterizing CDM-based models, which have the potential to be used for simulations of MOF formation.

5.2 Future Directions

While carrying out the research presented in this thesis, I have had the unshakable goal of making progress towards a better understanding of MOF synthesis. With the models and methodology presented in Chapter 4, I believe a step has been taken in the right direction. I am excited by recent studies in the literature that have characterized the free energy landscapes of growing MOF crystals by using similar nonbonded approaches to describing coordination bonds[42, 43, 44, 45]. I feel that by combining the progress made in these works towards developing order parameters and sampling methods for MOF crystallization with the CDM-based models described in Chapter 4, we can turn the dream of making quantitative predictions about MOF formation into a reality. A practical challenge that remains is to make the electrostatics of MOF models fully compatible with metal-solvent models. Metal-water models[58] are parameterized using full metal ion charges (in M-MOF-74, 2+), while the models in Chapter 4 rely on charges obtained from charge equilibration procedures performed on the framework (in M-MOF-74, all less than 2+). This discrepancy should be accounted for in order to model metals in both solution phase and MOF phase in the same simulation. I am actively working on a solution to this discrepancy, and am inspired by the recent advances made by Moosavi *et al.* towards gaining intuition of the parameters relevant to MOF synthesis using machine learning[41]. If expensive experiments can facilitate data-driven learning, it seems to me glaringly obvious that cheap, abundant simulation data teem with potential for enhancing our understanding.

Appendix A

Additional Information for Chapter 2

Table A.1: Descriptions of CVFF atom types in Fig. A.1. All information on nonbonded, bond, angle, dihedral and torsional interactions is obtained from the tables in the original CVFF paper[84].

CVFF (Labeled) Atom Type	Description
C-	Carboxylic Acid Carbon
Cp	Aromatic Carbon
C3	Aliphatic Carbon
O	Phenolic Carbon
O-	Carboxylic Acid Oxygen
H	Hydrogen

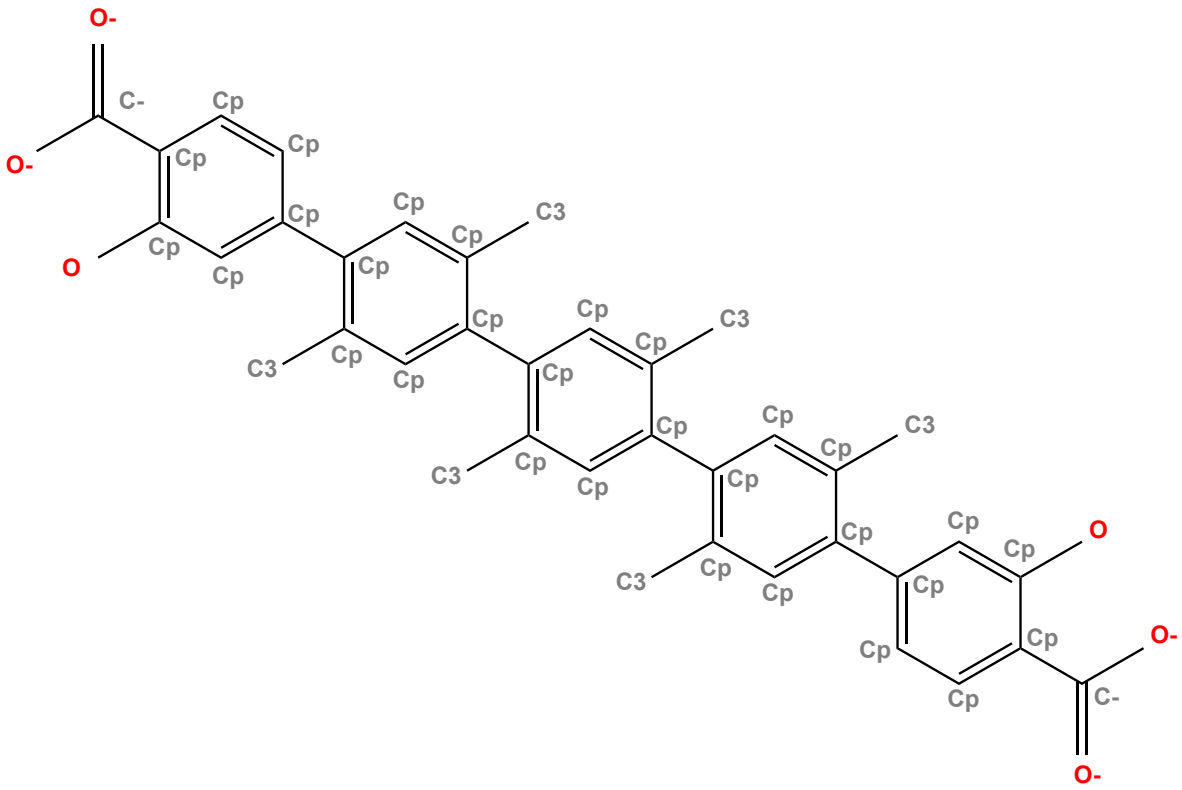

Figure A.1: The central aromatic rings and salicylic acid groups of the the linker in IRMOF-74-V (Mg). The atoms on all three aromatic rings are equivalent, as are the atoms on the two salicylic acids. The linker has a 4− charge. The CVFF atom types are labeled for each atom, and descriptions for each type are shown in Table A.1. Hydrogens are emitted for clarity.

Appendix B

Additional Information for Chapter 3

Table B.1: Translational self-diffusion coefficients (D_S) of *para*-xylene in MOF-5 computed from MD simulations.

Temperature (K)	D_S (m^2 / s)	Error (m^2 / s)
270	4.48×10^{-10}	1.84×10^{-12}
280	4.84×10^{-10}	4.13×10^{-12}
290	6.77×10^{-10}	8.36×10^{-12}
300	8.26×10^{-10}	1.87×10^{-12}

Table B.2: Translational self-diffusion coefficients (D_S) of *meta*-xylene in MOF-5 computed from MD simulations.

Temperature (K)	D_S (m^2 / s)	Error (m^2 / s)
270	4.05×10^{-10}	6.46×10^{-12}
280	4.61×10^{-10}	3.13×10^{-12}
290	6.34×10^{-10}	4.28×10^{-12}
300	7.87×10^{-10}	5.15×10^{-12}

Table B.3: Translational self-diffusion coefficients (D_S) of *ortho*-xylene in MOF-5 computed from MD simulations.

Temperature (K)	D_S (m^2 / s)	Error (m^2 / s)
270	3.99×10^{-10}	4.46×10^{-12}
280	4.82×10^{-10}	3.33×10^{-12}
290	5.25×10^{-10}	4.83×10^{-12}
300	6.41×10^{-10}	3.04×10^{-12}

Table B.4: In-plane rotational self-diffusion coefficients ($D_{R,\parallel}$) of *para*-xylene in MOF-5 computed from MD simulations.

Temperature (K)	$D_{R,\parallel}$ (rad^2 / ps)	Error (rad^2 / ps)
270	2.11×10^{-2}	4.46×10^{-4}
280	2.31×10^{-2}	3.33×10^{-4}
290	3.22×10^{-2}	4.83×10^{-4}
300	4.16×10^{-2}	3.04×10^{-4}

Table B.5: In-plane rotational self-diffusion coefficients ($D_{R,\parallel}$) of *meta*-xylene in MOF-5 computed from MD simulations.

Temperature (K)	$D_{R,\parallel}$ (rad^2 / ps)	Error (rad^2 / ps)
270	3.71×10^{-2}	4.55×10^{-3}
280	4.79×10^{-2}	1.36×10^{-3}
290	4.97×10^{-2}	5.19×10^{-5}
300	6.39×10^{-2}	2.03×10^{-3}

Table B.6: In-plane rotational self-diffusion coefficients ($D_{R,\parallel}$) of *ortho*-xylene in MOF-5 computed from MD simulations.

Temperature (K)	$D_{R,\parallel}$ (rad^2 / ps)	Error (rad^2 / ps)
270	9.87×10^{-2}	6.27×10^{-3}
280	1.06×10^{-1}	4.99×10^{-3}
290	1.16×10^{-1}	7.54×10^{-3}
300	1.28×10^{-1}	1.05×10^{-4}

Table B.7: Out-of-plane rotational self-diffusion coefficients ($D_{R,\perp}$) of *para*-xylene in MOF-5 computed from MD simulations.

Temperature (K)	$D_{R,\perp}$ (rad^2 / ps)	Error (rad^2 / ps)
270	8.30×10^{-2}	4.87×10^{-3}
280	9.46×10^{-2}	5.63×10^{-4}
290	1.25×10^{-1}	9.06×10^{-3}
300	1.31×10^{-1}	4.72×10^{-3}

Table B.8: Out-of-plane rotational self-diffusion coefficients ($D_{R,\perp}$) of *meta*-xylene in MOF-5 computed from MD simulations.

Temperature (K)	$D_{R,\perp}$ (rad^2 / ps)	Error (rad^2 / ps)
270	5.07×10^{-2}	1.48×10^{-3}
280	5.10×10^{-2}	3.07×10^{-3}
290	6.51×10^{-2}	4.65×10^{-3}
300	7.51×10^{-2}	1.84×10^{-3}

Table B.9: Out-of-plane rotational self-diffusion coefficients ($D_{R,\perp}$) of *ortho*-xylene in MOF-5 computed from MD simulations.

Temperature (K)	$D_{R,\perp}$ (rad^2 / ps)	Error (rad^2 / ps)
270	4.41×10^{-2}	3.86×10^{-4}
280	5.07×10^{-2}	6.16×10^{-3}
290	5.33×10^{-2}	3.03×10^{-3}
300	6.66×10^{-2}	7.42×10^{-4}

Appendix C

Additional Information for Chapter 4

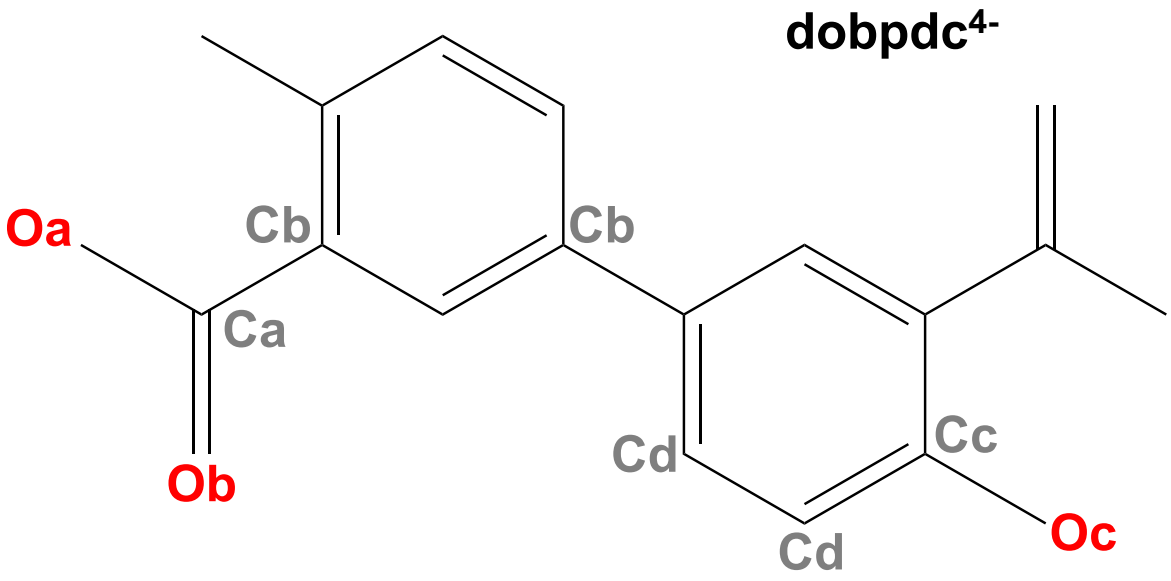

Figure C.1: The linker molecule in M-MOF-274, dobpdc^{4-} = 4,4-dioxidobiphenyl-3,3-dicarboxylate, with atomic labels. Half of the atoms are labeled because the molecule is symmetrical.

Table C.1: Cobalt-Oxygen parameters for Co-MOF-74, where the intermolecular potential is the Born-Mayer-Huggins potential: $E_{ij} = A_{ij}e^{B_{ij}(\sigma - r_{ij})} - \frac{C_{ij}}{{r_{ij}}^6}$; $\sigma = 1.5$.

	A (kcal mol^{-1})	B (Å^{-1})	C (kcal Å^6 mol^{-1})
Co-O_a	99.49	4.33	0.0
Co-O_b	87.04	5.83	0.0
Co-O_c	78.49	4.61	0.0

Table C.2: Iron-Oxygen parameters for Fe-MOF-74, where the intermolecular potential is the Born-Mayer-Huggins potential: $E_{ij} = A_{ij}e^{B_{ij}(\sigma - r_{ij})} - \frac{C_{ij}}{{r_{ij}}^6}$; $\sigma = 1.5$.

	A (kcal mol^{-1})	B (Å^{-1})	C (kcal Å^6 mol^{-1})
Fe-O_a	119.77	4.17	0.0
Fe-O_b	117.04	4.70	98.29
Fe-O_c	127.79	5.92	46.74

Table C.3: Magnesium-Oxygen parameters for Mg-MOF-74, where the intermolecular potential is the Born-Mayer-Huggins potential: $E_{ij} = A_{ij}e^{B_{ij}(\sigma - r_{ij})} - \frac{C_{ij}}{{r_{ij}}^6}$; $\sigma = 1.5$.

	A (kcal mol^{-1})	B (Å^{-1})	C (kcal Å^6 mol^{-1})
Mg-O_a	137.71	2.50	128.62
Mg-O_b	111.86	3.55	0.0
Mg-O_c	134.87	3.49	0.0

Table C.4: Manganese-Oxygen parameters for Mn-MOF-74, where the intermolecular potential is the Born-Mayer-Huggins potential: $E_{ij} = A_{ij}e^{B_{ij}(\sigma - r_{ij})} - \frac{C_{ij}}{{r_{ij}}^6}$; $\sigma = 1.5$.

	A (kcal mol^{-1})	B (Å^{-1})	C (kcal Å^6 mol^{-1})
Mn-O_a	131.25	3.61	0.0
Mn-O_b	87.72	3.51	0.0
Mn-O_c	182.10	5.88	72.41

Table C.5: Nickel-Oxygen parameters for Ni-MOF-74, where the intermolecular potential is the Born-Mayer-Huggins potential: $E_{ij} = A_{ij}e^{B_{ij}(\sigma - r_{ij})} - \frac{C_{ij}}{{r_{ij}}^6}$; $\sigma = 1.5$.

	A (kcal mol^{-1})	B (Å^{-1})	C (kcal Å^6 mol^{-1})
Ni-O_a	104.20	3.89	0.0
Ni-O_b	85.24	4.51	0.0
Ni-O_c	82.71	3.79	0.0

Table C.6: Zinc-Oxygen parameters for Zn-MOF-74, where the intermolecular potential is the Born-Mayer-Huggins potential: $E_{ij} = A_{ij}e^{B_{ij}(\sigma - r_{ij})} - \frac{C_{ij}}{{r_{ij}}^6}$; $\sigma = 1.5$.

	A (kcal mol^{-1})	B (Å^{-1})	C (kcal Å^6 mol^{-1})
Zn-O_a	102.84	3.99	0.0
Zn-O_b	87.93	5.18	0.0
Zn-O_c	150.96	5.83	603.83

Bibliography

[1] O. M. Yaghi, G. Li, and H. Li. "Selective Binding and Removal of Guests in a Microporous Metal-Organic Framework". In: *Nature* 378 (1995), pp. 703–706.

[2] C. J. Keper and M. J. Rosseinsky. "Zeolite-like Crystal Structure of an Empty Microporous Molecular Framework ". In: *Chem. Commun.* 0 (1999), pp. 375–376.

[3] L. R. MacGillivray, R. H. Groeneman, and J. L. Atwood. "Design and Self-Assembly of Cavity-Containing Rectangular Grids". In: *J. Am. Chem. Soc.* 120 (1998), pp. 2676–2677.

[4] G. B. Gardner et al. "Spontaneous Assembly of a Hinged Coordination Network". In: *Nature* 374 (1995), pp. 792–795.

[5] H. Li et al. "Design and Synthesis of an Exceptionally Stable and Highly Porous Metal-Organic Framework". In: *Nature* 402 (1999), pp. 276–279.

[6] G. L. Miessler, P. J. Fischer, and D. A. Tarr. *Inorganic Chemistry*. New York, NY: Pearson, 2014.

[7] H. Furukawa et al. "The Chemistry and Applications of Metal-Organic Frameworks". In: *Science* 341 (2013), p. 974.

[8] C. A. Trickett et al. "The Chemistry of Metal-Organic Frameworks for CO2 Capture, Regeneration and Conversion". In: *Nat. Rev. Mater.* 2 (2017), p. 17045.

[9] M. P. Suh et al. "Hydrogen Storage in Metal-Organic Frameworks". In: *Chem. Rev.* 112 (2012), pp. 782–835.

[10] Y. He et al. "Methane Storage in Metal-Organic Frameworks". In: *Chem. Soc. Rev.* 43 (2014), pp. 5657–5678.

[11] J. Liu et al. "Applications of Metal-Organic Frameworks in Heterogeneous Supramolecular Catalysis". In: *Chem. Soc. Rev.* 43 (2014), pp. 6011–6061.

[12] J. Gascon et al. "Metal Organic Framework Catalysis: Quo vadis?" In: *ACS. Catal.* 4 (2014), pp. 361–378.

[13] M. B. Majewski et al. "Metal-Organic Frameworks as Platform Materials for Solar Fuels Catalysis". In: *ACS Energy Lett.* 3 (2018), pp. 598–611.

[14] Y. Chen et al. "Acid-Resistant Mesoporous Metal-Organic Framework toward Oral Insulin Delivery: Protein Encapsulation, Protection, and Release". In: *J. Am. Chem. Soc* 140 (2018), pp. 5678–5681.

[15] S. Wang et al. "DNA-Functionalized Metal-Organic Framework Nanoparticles for Intracellular Delivery of Proteins". In: *J. Am. Chem. Soc.* 141 (2019), pp. 2215–2219.

[16] H. C. Zhou and S. Kitagawa. "Metal-Organic Frameworks (MOFs)". In: *Chem. Soc. Rev.* 43 (2014), pp. 5415–5418.

[17] P. Z. Moghadam et al. "Development of a Cambridge Structural Database Subset: A Collection of Metal-Organic Frameworks for Past, Present and Future". In: *Chem. Mater.* 29 (2017), pp. 2618–2625.

[18] P. G. Boyd, Y. Lee, and B. Smit. "Computational Development of the Nanoporous Materials Genome". In: *Nat. Rev. Mater.* 2 (2017), p. 17037.

[19] P. G. Boyd and T. K. Woo. "A Generalized Method for Constructing Hypothetical Nanoporous Materials of Any Net Topology from Graph Theory". In: *CrystEngComm* 18 (2016), pp. 3777–3792.

[20] D. A. Gomez-Gualdron et al. "Evaluating Topologically Diverse Metal-Organic Frameworks for Cryo-Adsorbed Hydrogen Storage". In: *Energy Environ. Sci.* 9 (2016), pp. 3279–3289.

[21] S. Li, Y. G. Chung, and R. Q. Snurr. "High-Throughput Screening of Metal-Organic Frameworks for CO2 Capture in the Presence of Water". In: *Langmuir* 32 (2016), pp. 10368–10376.

[22] M. Fernandez et al. "Large-Scale Quantitative Structure-Property Relationship (QSPR) Analysis of Methane Storage in Metal-Organic Frameworks". In: *J. Phys. Chem. C* 117 (2013), pp. 7681–7689.

[23] J. Canivet et al. "Structure-Property Relationships of Water Adsorption in Metal-Organic Frameworks". In: *New J. Chem.* 38 (2014), pp. 3102–3111.

[24] L.-C. Lin et al. "Force-Field Development from Electronic Structure Calculations with Periodic Boundary Conditions: Applications to Gaseous Adsorption and Transport in Metal-Organic Frameworks". In: *J. Chem. Theory Comput.* 10 (2014), pp. 1477–1488.

[25] R. Mercado et al. "Force Field Development from Periodic Density Functional Theory Calculations for Gas Separation Applications using Metal-Organic Frameworks". In: *J. Phys. Chem. C* 120 (2016), pp. 12590–12604.

[26] H. Li et al. "Establishing Microporosity in Open Metal-Organic Frameworks: Gas Sorption Isotherms for Zn(BDC) (BDC = 1,4-Benzenedicarboxylate)". In: *J. Am. Chem. Soc.* 120 (1998), pp. 8571–8572.

[27] P. A. Wright. *Microporous Framework Solids*. London, UK: Royal Society of Chemistry, 2008.

[28] E. D. Bloch et al. "Selective Binding of O2 over N2 in a Redox-Active Metal-Organic Framework with Open Iron(II) Coordination Sites". In: *J. Am. Chem. Soc.* 133 (2011), pp. 14814–14822.

[29] E. D. Bloch et al. "Hydrocarbon Separations in a Metal-Organic Framework with Open Iron (II) Coordination Sites". In: *Science* 335 (2012), pp. 1606–1610.

[30] W. L Queen et al. "Comprehensive Study of Carbon Dioxide Adsorption in the Metal-Organic Frameworks M2(dobdc)(M= Mg, Mn, Fe, Co, Ni, Cu, Zn)". In: *Chem. Sci.* 5 (2014), pp. 4569–4581.

[31] M. Asgari et al. "An Experimental and Computational Study of CO2 Adsorption in the Sodalite-type M-BTT (M= Cr, Mn, Fe, Cu) Metal-Organic Frameworks Featuring Open Metal Sites". In: *Chem. Sci* 9 (2018), pp. 4579–4588.

[32] S. Xiang et al. "Exceptionally High Acetylene Uptake in a Microporous Metal-Organic Framework with Open Metal Sites". In: *J. Am. Chem. Soc.* 131 (2009), pp. 12415–12419.

[33] O. M. Yaghi et al. "Reticular Synthesis and the Design of New Materials". In: *Nature* 423 (2003), pp. 705–714.

[34] N. W. Ockwig et al. "Reticular Chemistry: Occurrence and Taxonomy of Nets and Grammar for the Design of Frameworks". In: *Acc. Chem. Res.* 38 (2005), pp. 176–182.

[35] K. E. Cordova and O. M. Yaghi. "The 'Folklore' and Reality of Reticular Chemistry". In: *Mater. Chem. Front.* 1 (2017), pp. 1304–1309.

[36] D. J. Tranchemontagne et al. "Reticular Chemistry of Metal-Organic Polyhedra". In: *Angew. Chem. Int. Ed.* 47 (2008), pp. 5136–5147.

[37] M. Witman et al. "In Silico Design and Screening of Hypothetical MOF-74 Analogs and their Experimental Synthesis". In: *Chem. Sci.* 7 (2016), pp. 6263–6272.

[38] C. E. Wilmer et al. "Large-Scale Screening of Hypothetical Metal-Organic Frameworks". In: *Nat. Chem.* 4 (2012), pp. 83–89.

[39] M. Fernandez et al. "Rapid and Accurate Machine Learning Recognition of High Performing Metal Organic Frameworks for CO2 Capture". In: *J. Phys. Chem. Lett.* 5 (2014), pp. 3056–3060.

[40] M. L. Kelty et al. "High-Throughput Synthesis and Characterization of Nanocrystalline Porphyrinic Zirconium Metal-Organic Frameworks". In: *Chem. Commun.* 52 (2016), pp. 7854–7857.

[41] S. M. Moosavi et al. "Capturing Chemical Intuition in Synthesis of Metal-Organic Frameworks". In: *Nat. Commun.* 10 (2019), p. 539.

[42] M. Yoneya, S. Tsuzuki, and M. Aoyagi. "Simulation of Metal-Organic Framework Self-Assembly". In: *Phys. Chem. Chem. Phys.* 17 (2015), pp. 8649–8652.

[43] D. Biswal and P. G. Kusalik. "Probing Molecular Mechanisms of Self-Assembly in Metal-Organic Frameworks". In: *ACS Nano* 11 (2017), pp. 258–268.

[44] D. Biswal and P. G. Kusalik. "Molecular Simulations of Self-Assembly Processes in Metal-Organic Frameworks: Model Dependence". In: *J. Chem. Phys.* 147 (2017), p. 044702.

[45] Y. J. Colón et al. "Free Energy of Metal-Organic Framework Self-Assembly". In: 150 (2019), p. 104502.

[46] N. L. Rosi et al. "Rod Packings and Metal-Organic Frameworks Constructed from Rod-Shaped Secondary Building Units". In: *J. Am. Chem. Soc* 127 (2005), pp. 1504–1518.

[47] P. D. C. Dietzel et al. "An In Situ High-Temperature Single-Crystal Investigation of a Dehydrated Metal-Organic Framework Compound and Field-Induced Magnetization of One-Dimensional Metal-Oxygen Chains". In: *Angew. Chem. Int. Ed.* 44 (2005), pp. 6354–6358.

[48] P. D. C. Dietzel et al. "Hydrogen Adsorption in a Nickel Based Coordination Polymer with Open Metal Sites in the Cylindrical Cavities of the Desolvated Framework". In: *Chem. Commun.* 0 (2006), pp. 959–961.

[49] P. D. C. Dietzel, R. Blom, and H. Fjellvåg. "Base-Induced Formation of Two Magnesium Metal-Organic Framework Compounds with a Bifunctional Tetratopic Ligand". In: *Eur. J. Inorg. Chem.* 2008 (2008), pp. 3624–3632.

[50] S. Bhattacharjee et al. "Solvothermal Synthesis of Fe-MOF-74 and Its Catalytic Properties in Phenol Hydroxylation". In: *J. Nanosci. Nanotechnol.* 10 (2010), pp. 135–141.

[51] W. Zhou, H. Wu, and T. Yildirim. "Enhanced H2 Adsorption in Isostructural Metal-Organic Frameworks with Open Metal Sites: Strong Dependence of the Binding Strength on Metal Ions". In: *J. Am. Chem. Soc* 130 (2008), pp. 15268–15269.

[52] R. Sanz et al. "Synthesis of a Honeycomb-Like Cu-based Metal-Organic Framework and Its Carbon Dioxide Adsorption Behaviour". In: *Dalton Tran.* 32 (2013), pp. 2392–2398.

[53] L. J Wang et al. "Synthesis and Characterization of Metal-Organic Framework-74 Containing 2, 4, 6, 8, and 10 Different Metals". In: *Inorg. Chem.* 53 (2014), pp. 5881–5883.

[54] A. L. Dzubak et al. "Ab Initio Carbon Capture in Open-Site Metal-Organic Frameworks". In: *Nat. Chem.* 4 (2012), pp. 810–816.

[55] R. H. Holm, P. Kennepohl, and E. I. Solomon. "Structural and Functional Aspects of Metal Sites in Biology". In: *Chem. Rev.* 96 (1996), pp. 2239–2314.

[56] J. Reedijk and E. Bouwman. *Bioinorganic Catalysis*. Boca Raton, FL: CRC Press, 1999.

[57] C. M. Gomes and P. W. Stafshede. *Protein Folding and Metal Ions: Mechanisms, Biology and Disease*. Boca Raton, FL: CRC Press, 2010.

[58] F. Duarte et al. "Force Field Independent Metal Parameters Using a Nonbonded Dummy Model". In: *J. Phys. Chem. B.* 118 (2014), pp. 4351–4362.

[59] J. Åqvist and A. Warshel. "Free Energy Relationships in Metalloenzyme-Catalyzed Reactions. Calculations of the Effects of Metal Ion Substitutions in Staphylococcal Nuclease". In: *J. Am. Chem. Soc* 112 (1990), pp. 2860–2868.

[60] C. N. Pace et al. "Protein Structure, Stability and Solubility in Water and Other Solvents". In: *Phil. Trans. R. Soc. Lond. B* 359 (2004), pp. 1225–1235.

[61] M.-C. Bellissent-Funel et al. "Water Determines the Structure and Dynamics of Proteins". In: *Chem. Rev.* 116 (2016), pp. 7673–7697.

[62] D. J. Cole and N. D. M. Hine. "Applications of Large-Scale Density Functional Theory in Biology". In: *J. Phys. Condens. Matter* 28 (2016), p. 393001.

[63] J. Åqvist and A. Warshel. "Computer Simulation of the Initial Proton Transfer Step in Human Carbonic Anhydrase I". In: *J. Mol. Biol.* 224 (1992), pp. 7–14.

[64] Y. Jiang, H. Zhang, and T. Tan. "Rational Design of Methodology-Independent Metal Parameters Using a Nonbonded Dummy Model". In: *J. Chem. Theory Comput.* 12 (2016), pp. 3250–3260.

[65] A. Saxena and D. Sept. "Multisite Ion Models That Improve Coordination and Free Energy Calculations in Molecular Dynamics Simulations". In: *J. Chem. Theory Comput.* 9 (2013), pp. 3538–3542.

[66] Liao. Q. et al. "Extending the Nonbonded Cationic Dummy Model to Account for Ion-Induced Dipole Interactions". In: *J. Phys. Chem. Lett.* 8 (2017), pp. 5408–5414.

[67] Y.-P. Pang. "Novel Zinc Protein Molecular Dynamics Simulations: Steps Toward Antiangiogenesis for Cancer Treatment". In: *J. Mol. Model.* 5 (1999), pp. 196–202.

[68] Y.-P. Pang. "Successful Molecular Dynamics Simulation of Two Zinc Complexes Bridged by a Hydroxide in Phosphotriesterase Using the Cationic Dummy Atom". In: *Proteins* 45 (2001), pp. 183–189.

[69] Q. Liao, S. C. L. Kamerlin, and B. Strodel. "Development and Application of a Nonbonded Cu2+ Model That Includes the Jahn-Teller Effect". In: *J. Phys. Chem. Lett.* 6 (2015), pp. 2657–2662.

[70] Y. X. Xiang and J. W. Ponder. "A Valence Bond Model for Aqueous Cu(II) and Zn(II) Ions". In: *J. Comput. Chem* 34 (2013), pp. 739–749.

[71] Y. X. Xiang and J. W. Ponder. "An Angular Overlap Model for Cu(II) Ion in the AMOEBA Polarizable Force Field". In: *J. Chem. Theory. Comput.* 10 (2014), pp. 298–311.

[72] R. Ren and J. W. Ponder. "Consistent Treatment of Inter- and Intramolecular Polarization in Molecular Mechanics Calculations". In: *J. Comput. Chem.* 23 (2002), pp. 1497–1506.

[73] D. Dubbeldam et al. "Exceptional Negative Thermal Expansion in Isoreticular Metal-Organic Frameworks". In: *Angew. Chem. Int. Ed.* 46 (2007), pp. 4496–4499.

[74] D. Frenkel and B. Smit. *Understanding Molecular Simulation: From Algorithms to Applications*. San Diego, CA: Academic Press, 2002.

[75] M. Tuckerman. *Statistical Mechanics: Theory and Molecular Simulation*. Oxford, UK: Oxford University Press, 2010.

[76] D. J. Evans and G Morriss. *Statistical Mechanics of Nonequilibrium Liquids*. Cambridge, UK: Cambridge University Press, 2014.

[77] E. Braun, S. M. Moosavi, and B. Smit. "Anomalous Effects of Velocity Rescaling Algorithms: The Flying Ice Cube Effect Revisited". In: *J. Chem. Theory Comput.* 14 (2018), pp. 5262–5272.

[78] S. Nosé. "A Molecular Dynamics Method for Simulations in the Canonical Ensemble". In: *Mol. Phys.* 52 (1984), pp. 255–268.

[79] W. G. Hoover. "Canonical Dynamics: Equilibrium Phase-Space Distributions". In: *Phys. Rev. A* 31.3 (1985), pp. 1695–1697.

[80] M. Parrinello and A. Rahman. "Crystal Structure and Pair Potentials: A Molecular-Dynamics Study". In: *Phys. Rev. Lett.* 45 (1980), p. 1196.

[81] M. Parrinello and A. Rahman. "Polymorphic Transitions in Single Crystals: A New Molecular Dynamics Method". In: *J. Appl. Phys.* 52 (1981), p. 7182.

[82] M. Parrinello and A. Rahman. "Strain Fluctuations and Elastic Constants". In: *J. Chem. Phys.* 76 (1982), p. 2662.

[83] G. J. Martyna, D. J. Tobias, and M. L. Klein. "Constant Pressure Molecular Dynamics Algorithms". In: *J. Chem. Phys* 101 (1994), p. 4177.

[84] P. Dauber-Osguthorpe et al. "Structure and Energetics of Ligand Binding to Proteins: Escheria coli Dihydrofolate Reductase-Trimethoprim, a Drug-Receptor System". In: *PROTEINS* 4 (1988), pp. 31–47.

[85] S. L. Mayo, B. D. Olafson, and W. A. Goddard. "DREIDING: A Generic Force Field for Molecular Simulations". In: *J. Phys. Chem.* 94 (1990), pp. 8897–8909.

[86] A. Schneemann et al. "Flexible Metal-Organic Frameworks". In: *Chem. Soc. Rev.* 43 (2014), pp. 6062–6096.

[87] M. D. Allendorf et al. "Stress-Induced Chemical Detection Using Flexible Metal-Organic Frameworks". In: *J. Am. Chem. Soc.* 130 (2008), pp. 14404–14405.

[88] A. V. Neimark et al. "Stress-based Model for the Breathing of Metal-Organic Frameworks". In: *J. Phys. Chem. Lett.* 1 (2010), pp. 445–449.

[89] F. X. Coudert et al. "Adsorption Deformation and Structural Transitions in Metal-Organic Frameworks: From the Unit Cell to the Crystal". In: *J. Phys. Chem. Lett.* 4 (2013), pp. 3198–3205.

[90] C. Serre et al. "Role of Solvent-Host Interactions that Lead to Very Large Swelling of Hybrid Frameworks". In: *Science* 315 (2007), pp. 1828–1831.

[91] G. Férey and C. Serre. "Large Breathing Effects in Three-Dimensional Porous Hybrid Matter: Facts, Analyses, Rules and Consequences". In: *Chem. Soc. Rev.* 38 (2009), pp. 1380–1399.

[92] T. Loiseau et al. "A Rationale for the Large Breathing of the Porous Aluminum Terephthalate (MIL-53) upon Hydration". In: *Chem. Eur. Jour.* 10 (2004), pp. 1373–1382.

[93] J. A. Mason et al. "Methane Storage in Flexible Metal-Organic Frameworks with Intrinsic Thermal Management". In: *Nature* 527 (2015), pp. 357–361.

[94] W. Yang et al. "Selective CO2 Uptake and Inverse CO2/C2H2 Selectivity in a Dynamic Bifunctional Metal-Organic Framework". In: *Chem. Sci.* 3 (2012), pp. 2993–2999.

[95] S. Krause et al. "A Pressure-amplifying Framework Material with Negative Gas Adsorption Transitions". In: *Nature* 532 (2016), pp. 348–352.

[96] F. X. Coudert et al. "Thermodynamics of Guest-induced Structural Transitions in Hybrid Organic-Inorganic Frameworks". In: *J. Am. Chem. Soc.* 130 (2008), pp. 14293–14302.

[97] P. Küsgens et al. "Characterization of Metal-Organic Frameworks by Water Adsorption". In: *Microporous Mesoporous Mater.* (2009), pp. 325–330.

[98] T. M. McDonald et al. "Cooperative Insertion of CO2 in Diamine-Appended Metal-Organic Frameworks". In: *Nature* 519 (2015), pp. 303–308.

[99] H. S. Cho et al. "Extra Adsorption and Adsorbate Superlattice Formation in Metal-Organic Frameworks". In: *Nature* 527 (2015), pp. 503–507.

[100] H. Deng et al. "Large-Pore Apertures in a Series of Metal-Organic Frameworks". In: *Science* 336 (2012), pp. 1018–1023.

[101] G. Kresse and J. Furthmüller. "Efficient Iterative Schemes for Ab Initio Total-Energy Calculations Using a Plane-wave Basis Set". In: *Phys. Rev. B* 54 (1996), pp. 11169–11186.

[102] P. E. Blöchl. "Projector Augmented-wave Method". In: *Phys. Rev. B* 50 (1994), 17953–17979s.

[103] G. Kresse and D. Joubert. "From Ultrasoft Pseudopotentials to the Projector Augmented-wave Method". In: *Phys. Rev. B* 59 (1999), pp. 1758–1775.

[104] J. P. Perdew, K. Burke, and M. Ernzerhof. "Generalized Gradient Approximation Made Simple". In: *Phys. Rev. Lett.* 77 (1996), pp. 3865–3868.

[105] I. Hamada. "Van der Waals Density Functional Made Accurate". In: *Phys. Rev. B* 89 (2014), p. 121103.

[106] J. Klimeš, D. R. Bowler, and A. Michaelides. "Van der Waals Density Functionals Applied to Solids". In: *Phys. Rev. B* 83 (2011), p. 195131.

[107] G. Román-Pérez and J. M. Soler. "Efficient Implementation of a van der Waals Density Functional: Application to Double-Wall Carbon Nanotubes". In: *Phys. Rev. Lett.* 103 (2009), p. 096102.

[108] K. Lee et al. "Small-Molecule Adsorption in Open-Site Metal-Organic Frameworks: A Systematic Density Functional Theory Study for Rational Design". In: *Chem. Mater.* 27 (2015), pp. 668–678.

[109] C. Campañà, B. Mussard, and T. K. Woo. "Electrostatic Potential Derived Atomic Charges for Periodic Systems Using a Modified Error Functional". In: *J. Chem. Theory Comp.* 5 (2009), pp. 2866–2878.

[110] J. A. Greathouse and M. D. Allendorf. "The Interaction of Water with MOF-5 Simulated by Molecular Dynamics". In: *J. Am. Chem Soc.* 128 (2006), pp. 10678–10679.

[111] D. Brown and J. H. R. Clarke. "A Comparison of Constant Energy, Constant Temperature and Constant Pressure Ensembles in Molecular Dynamics Simulations of Atomic Liquids". In: *Mol. Phys.* 51 (1984), pp. 1243–1252.

[112] M. D. Macedonia, D. D. Moore, and E. J. Maginn. "Adsorption Studies of Methane, Ethane, and Argon, in the Zeolite Mordenite: Molecular Simulations and Experiments". In: *Langmuir* 16 (2000), pp. 3823–3834.

[113] J. J. Potoff and J. I. Siepmann. "Vapor-Liquid Equilibria of Mixtures Containing Alkanes, Carbon Dioxide and Nitrogen". In: *AICHE J.* 47 (2001), pp. 1676–1682.

[114] J. G. Harris and K. H. Yung. "Carbon Dioxide's Liquid-Vapor Coexistence Curve and Critical Properties as Predicted by a Simple Molecular Model". In: *J. Phys. Chem.* 99 (1995), pp. 12021–12024.

[115] P. B. Balbuena and K. E. Gubbins. "Theoretical Interpretation of Adsorption Behavior of Simple Fluids in Slit Pores". In: *Langmuir* 9 (1993), pp. 1801–1814.

[116] L. Sarkisov and P. A. Monson. "Hysteresis in Monte Carlo and Molecular Dynamics Simulations of Adsorption in Porous Media". In: *Langmuir* 16 (2000), pp. 9857–9860.

[117] H. Demir et al. "DFT-based Force Field Development for Noble Gas Adsorption in Metal Organic Frameworks". In: *J. Mater. Chem. A.* 3 (2015), pp. 23539–23548.

[118] S. Plimpton. "Fast Parallel Algorithms for Short-Range Molecular Dynamics". In: *J. Comp. Phys.* 117 (1995), pp. 1–19.

[119] R. J Hunter. *Foundations of Colloid Science*. Oxford, UK: Oxford University Press, 2001.

[120] X. Wang et al. "Anisotropic Lattice Thermal Conductivity and Suppressed Acoustic Phonons in MOF-74 from First Principles". In: *J. Phys. Chem. C* 119 (2015), pp. 26000–26008.

[121] S. R. Caskey, A. G. Wong-Foy, and A. J. Matzger. "Dramatic Tuning of Carbon Dioxide Uptake via Metal Substitution in a Coordinate Polymer with Cylindrical Pores". In: *J. Am. Chem. Soc.* 130 (2008), pp. 10870–10871.

[122] S. P. Coleman, D. E. Spearot, and L. Capolungo. "Virtual Diffraction Analysis of Ni [0 1 0] Symmetric Tilt Grain Boundaries". In: *Model. Simul. Mater. Sci. Eng.* 21 (2013), p. 16.

[123] D. Schneidman-Duhovny et al. "Accurate SAXS Profile Computation and Its Assessment by Contrast Variation Experiments". In: *Biophys. J.* 105 (2013), pp. 962–974.

[124] D. S. Sholl and R. P. Lively. "Seven Chemical Separations to Change the World". In: *Nature* 532.7600 (2016), p. 435.

[125] Y. Yang, P. Bai, and X. Guo. "Separation of Xylene Isomers: A Review of Recent Advances in Materials". In: *Ind. Eng. Chem. Res.* 56 (2017), pp. 14725–14753.

[126] M. I. Gonzalez et al. "Separation of Xylene Isomers through Multiple Metal Site Interactions in Metal-Organic Frameworks". In: *J. Am. Chem. Soc.* 140 (2018), pp. 3412–3422.

[127] J. Kärger et al. "Benefit of Microscopic Diffusion Measurement for the Characterization of Nanoporous Materials". In: *Chem. Eng. Technol.* 32 (2009), pp. 1494–1511.

[128] Mark E Davis. "Ordered Porous Materials for Emerging Applications". In: *Nature* 417 (2002), pp. 813–821.

[129] Christian Chmelik et al. "Ethene/Ethane Mixture Diffusion in the MOF Sieve ZIF-8 Studied by MAS PFG NMR Diffusometry". In: *Microporous Mesoporous Mater.* 147 (2012), pp. 135–141.

[130] A.-K. Pusch et al. "NMR Studies of Carbon Dioxide and Methane Self-Diffusion in ZIF-8 at Elevated Gas Pressures". In: *Adsorption* 18 (2012), pp. 359–366.

[131] L. Alaerts et al. "Activation of the Metal-Organic Framework MIL-47 for Selective Adsorption of Xylenes and Other Difunctionalized Aromatics". In: *Phys. Chem. Chem. Phys.* 10 (2008), pp. 2979–2985.

[132] S. Rives et al. "Diffusion of Xylene Isomers in the MIL-47 (V) MOF Material: Synergic Combination of Computational and Experimental Tools". In: *J. Phys. Chem.* 47.117 (2013), pp. 6293–6302.

[133] A. Gabrienko and B. Frick. "Diffusion of Xylene Isomers in the MIL-47 (V) MOF Material : A Synergic Combination of Synergic Combination of Computational and Experimental Tools". In: *J. Phys. Chem. C* 47.117 (2013), pp. 6293–6302.

[134] M. A. Moreira et al. “Influence of the Eluent in the MIL-53 (Al) Selectivity for Xylene Isomers Separation”. In: *Ind. Eng. Chem. Res.* 50 (2011), pp. 7688–7695.

[135] L. Duan et al. “Adsorption and Diffusion Properties of Xylene Isomers and Ethylbenzene in Metal-Organic Framework MIL-53 (Al)”. In: *J. Porous Mater.* 53 (2013), pp. 431–440.

[136] L. Alaerts et al. “Selective Adsorption and Separation of Xylene isomers and Ethylbenzene with the Microporous Vanadium(IV) Terephthalate MIL-47.” In: *Angew. Chem. Int. Ed.* 46.23 (2007), pp. 4293–7.

[137] V. Finsy et al. “Pore-Filling-Dependent Selectivity Effects in the Vapor-Phase Separation of Xylene Isomers on the Metal-Organic Framework MIL-47”. In: *J. Am. Chem. Soc.* 130.22 (2008), pp. 7110–8.

[138] Z.-Y. Gu et al. “Adsorption and Separation of Xylene Isomers and Ethylbenzene on Two Zn-Terephthalate Metal-Organic Frameworks”. In: *J. Phys. Chem. C* 114 (2010), pp. 311–316.

[139] J. A. Gee and D. S. Sholl. “Effect of Framework Flexibility on C 8 Aromatic Adsorption at High Loadings in Metal-Organic Frameworks”. In: *J. Phys. Chem. C* 120.1 (2016), pp. 370–376.

[140] A. Germanus et al. “Intracrystalline Self-Diffusion of Benzene, Toluene and Xylene Isomers in Zeolites Na-X”. In: *Zeolites* 5 (1985), pp. 91–95.

[141] P. Trens et al. “Adsorption and Xeparation of Xylene Isomers Vapors onto the Chromium Terephthalate-Based Porous Material MIL-101 (Cr): An Experimental and Computational study”. In: *Microporous Mesoporous Mater.* 183 (2014), pp. 17–22.

[142] M. A. Moreira et al. “Reverse Shape Selectivity in the Liquid-Phase Adsorption of Xylene Isomers in Zirconium Terephthalate MOF UiO-66”. In: *Langmuir* 21 (2012), pp. 5715–5723.

[143] F. Stallmach et al. “NMR Studies on the Diffusion of Hydrocarbons on the Metal-Organic Framework Material MOF-5.” In: *Angew. Chem. Int. Ed.* 45 (2006), pp. 2123–6.

[144] D. I. Kolokolov et al. “Rotational and Translational Motion of Benzene in ZIF-8 Studied by 2H NMR: Estimation of Microscopic Self-Diffusivity and Its Comparison with Macroscopic Measurements”. In: 118 (2014), pp. 12873–12879.

[145] S. Schlayer et al. “X-Nuclei NMR Self-Diffusion Studies in Mesoporous Silica Foam and Microporous MOF CuBTC”. In: *Materials (Basel)* 5 (2012), pp. 617–633.

[146] D. C. Ford, D. Dubbeldam, and R. Q. Snurr. “The Effect of Framework Flexibility on Diffusion of Small Molecules in the Metal-Organic Framework IRMOF-1”. In: *Open-Access J. Basic Princ. Diffus. Theory, Exp. Appl.* 11 (2009), pp. 1–8.

[147] C. D. Wick, M. G. Martin, and J. I. Siepmann. "Transferable Potentials for Phase Equilibria. 4. United-Atom Description of Linear and Branched Alkenes and Alkylbenzenes". In: *J. Phys. Chem. B* 104 (2000), pp. 8008–8016.

[148] E. Braun et al. "Nanoporous Materials Can Tune the Critical Point of a Pure Substance". In: *Angew. Chem. Int. Ed.* 54 (2015), pp. 14349–52.

[149] H. Kamberaj, R. J. Low, and M. P. Neal. "Time Reversible and Symplectic Integrators for Molecular Dynamics Simulations of Rigid Molecules". In: *J. Chem. Phys.* 122.22 (2005), p. 224114.

[150] D. Dubbeldam et al. "A New Perspective on the Order-n Algorithm for Computing Correlation Functions". In: *Mol. Simul.* 35.12-13 (2009), pp. 1084–1097.

[151] B. Rousseau and J. Petravic. "Transport Coefficients of Xylene Isomers". In: *The Journal of Physical Chemistry B* 106 (2002), pp. 13010–13017.

[152] Anup Kitchlew and B D Nageswara Rao. "Temperature Dependence Diffusion in Liquids". In: *Mol. Phys.* 21 (1971), pp. 1145–1147.

[153] M. G. Mazza et al. "Connection of Translational and Rotational Dynamical Heterogeneities with the Breakdown of the Stokes-Einstein and Stokes-Einstein-Debye Relations in Water". In: *Physical Review E* 76.3 (2007), p. 031203.

[154] R. G. Eades, T. A. Jones, and J. P. Llewellyn. "N.M.R. Investigation of Molecular Motions in Solid Xylene". In: *J. Chem. Soc. Faraday Trans. 2: Mol. Chem. Physics* 12 (1972), pp. 1316–1322.

[155] D. Ongari et al. "Origin of the Strong Interaction between Polar Molecules and Copper(II) Paddle-Wheels in Metal Organic Frameworks". In: *J. Phys. Chem. C* 121 (2017), pp. 15136–15144.

[156] J. C. Tan, T. D. Bennett, and A. K. Cheetham. "Chemical Structure, Network Topology, and Porosity Effects on the Mechanical Properties of Zeolitic Imidazolate Frameworks". In: *Proc. Natl. Acad. Sci. U.S.A.* 107 (2010), pp. 9938–9943.

[157] V. Armel et al. "Structural Descriptors of Zeolitic-Imidazolate Frameworks Are Keys to the Activity of Fe-N-C Catalysts". In: *J. Am. Chem. Soc.* 139 (2017), pp. 453–464.

[158] S. M. Moosavi et al. "Improving the Mechanical Stability of Metal-Organic Frameworks Using Chemical Caryatids". In: *ACS Cent. Sci.* 4 (2018), pp. 832–839.

[159] W. You et al. "Competitive Binding of Ethylene, Water, and Carbon Monoxide in Metal-Organic Framework Materials with Open Cu Sites". In: *J. Phys. Chem. C* 122 (2018), pp. 8960–8966.

[160] D. Nazarian et al. "Large-Scale Refinement of Metal-Organic Framework Structures Using Density Functional Theory". In: *Chem. Mater.* 29 (2017), pp. 2521–2528.

[161] T. Watanabe and D. S. Sholl. "Accelerating Applications of Metal-Organic Frameworks for Gas Adsorption and Separation by Computational Screening of Materials". In: *Langmuir* 28 (2012), pp. 14114–14128.

[162] J. A. Greathouse et al. "Computational Screening of Metal-Organic Frameworks for Large-Molecule Chemical Sensing". In: *Phys. Chem. Chem. Phys.* 12 (2010), pp. 12621–12629.

[163] C. M. Simon et al. "Statistical Mechanical Model of Gas Adsorption in Porous Crystals with Dynamic Moieties". In: *Proc. Natl. Acad. Sci. U.S.A.* 114 (2016), E287–E296.

[164] M. Witman et al. "The Influence of Intrinsic Framework Flexibility on Adsorption in Nanoporous Materials". In: *J. Am. Chem. Soc.* 139 (2017), pp. 5547–5557.

[165] A. Gładysiak et al. "Biporous Metal-Organic Framework with Tunable CO2/CH4 Separation Performance Facilitated by Intrinsic Flexibility". In: *ACS Appl. Mater. Interfaces* 10 (2018), pp. 36144–36156.

[166] J. Heinen and D. Dubbeldam. "On Flexible Force Fields for Metal-Organic Frameworks: Recent Developments and Future Prospects". In: *Wiley Interdiscip. Rev. Comput. Mol. Sci.* 8 (2018), e1363.

[167] D. E. Coupry, M. A. Addicoat, and T. Heine. "Extension of the Universal Force Field for Metal-Organic Frameworks". In: *J. Chem. Theory Comput.* 12 (2016), pp. 5215–5225.

[168] S. Bureekaew et al. "MOF-FF - A Flexible First-Principles Derived Force Field for Metal-Organic Frameworks". In: *Phys. Status Solidi B* 250 (2013), pp. 1128–1141.

[169] L. Vanduyfhuys et al. "QuickFF: A Program for a Quick and Easy Derivation of Force Fields for Metal-Organic Frameworks from Ab Initio Input". In: *J. Comput. Chem.* 36 (2015), pp. 1015–1027.

[170] C. M. Draznieks et al. "De Novo Prediction of Inorganic Structures Developed through Automated Assembly of Secondary Building Units (AASBU Method)". In: *Angew. Chem. Intl. Ed.* 39 (2000), pp. 2270–2275.

[171] A. Thirumurugan and S. Natarajan. "Assembly of a Secondary Building Unit (SBU) into Two- and Three-Dimensional Structures in Lanthanide Benzenedicarboxylates". In: *Cryst. Growth Des.* 6 (2006), pp. 983–988.

[172] M. Wahiduzzaman et al. "Computational Structure Determination of Novel Metal-Organic Frameworks". In: *ChemComm* 54 (2018), pp. 10812–10815.

[173] S. Jawahery et al. "Adsorbate-Induced Lattice Deformation in IRMOF-74 Series". In: *Nat. Commun.* 8 (2017), p. 13945.

[174] H. Deng et al. "Large-Pore Apertures in a Series of Metal-Organic Frameworks". In: *Science* 336 (2012), pp. 1018–1023.

[175] G. Kresse and J. Furthmüller. "Efficient Iterative Schemes for Ab Initio Total-energy Calculations Using a Plane-wave Basis Set". In: *Phys. Rev. B* 54 (1996), pp. 11169–11186.

[176] J. P. Perdew, K. Burke, and M. Ernzerhof. "Generalized Gradient Approximation Made Simple". In: *Phys. Rev. Lett.* 77 (1996), pp. 3865–3868.

[177] P. E. Blöchl. "Projector Augmented-wave Method". In: *Phys. Rev. B* 50 (1994), pp. 17953–17979.

[178] G. Kresse and D. Joubert. "From Ultrasoft Pseudopotentials to the Projector Augmented-wave Method". In: *Phys. Rev. B* 59 (1999), pp. 1758–1775.

[179] G. W. Mann et al. "First-Principles Hubbard U Approach for Small Molecule Binding in Metal-Organic Frameworks". In: *J. Chem. Phys.* 144 (2016), p. 174104.

[180] K. Lee et al. "Small-Molecule Adsorption in Open-Site Metal-Organic Frameworks: A Systematic Density Functional Theory Study for Rational Design". In: *Chem. Mater.* 27 (2015), pp. 668–678.

[181] M. P. Tosi and F. G. Fumi. "Ionic Sizes and Born Repulsive Parameters in the NaCl-type Alkali Halides-II: The Generalized Huggins-Mayer Form". In: *J. Phys. Chem. Solids* 25 (1963), pp. 45–52.

[182] S. K. Ashour and M. A. Abdel-hameed. "Approximate Skew Normal Distribution". In: *J. Adv. Res.* 1 (2010), pp. 341–350.

[183] P. G. Boyd et al. "Force-Field Prediction of Materials Properties in Metal-Organic Frameworks". In: *J. Phys. Chem. Lett.* 8 (2017), pp. 357–363.

[184] H. Wu, T. Yildirim, and W. Zhou. "Exceptional Mechanical Stability of Highly Porous Zirconium Metal-Organic Framework UiO-66 and Its Importation Implications". In: *J. Phys. Chem. Lett.* 4 (2013), pp. 925–930.

[185] S. M. J. Rogge, M. Waroquier, and V. Van Speybroeck. "Reliably Modeling the Mechanical Stability of Rigid and Flexible Metal-Organic Frameworks". In: *Acc. Chem. Res.* 51 (2018), pp. 138–148.

[186] J. H. Lee et al. "Enhancement of CO2 Binding and Mechanical Properties upon Diamine Functionalization of M2(dobpdc) Metal-Organic Frameworks". In: *Chem. Sci.* 9 (2018), pp. 5197–5206.

[187] L. Vanduyfhuys et al. "Thermodynamic Insight into Stimuli-Responsive Behavior of Soft Porous Crystals". In: *Nat. Commun.* 9 (2018), p. 204.

[188] C. Y. Lee et al. "Kinetic Separation of Propene and Propane in Metal-Organic Frameworks: Controlling Diffusion Rates in Plate-Shaped Crystals via Tuning of Pore apertures and Crystallite Aspect Ratios". In: *J. Am. Chem. Soc.* 133 (2011), pp. 5228–5231.

[189] R. Lin et al. "Metal Organic Framework Based Mixed Matrix Membranes: An Overview on Filler/Polymer Interfaces". In: *J. Mater. Chem. A* 8 (2018), pp. 293–312.

[190] X. Li et al. "Metal-Organic Frameworks Based Membranes for Liquid Separation". In: *Chem. Soc. Rev.* 46 (2017), pp. 7124–7144.

[191] D. T. Sun et al. "Rapid, Selective Heavy Metal Removal from Water by a Metal-Organic Framework/Polydopamine Composite". In: *ACS Cent. Sci.* 3 (2018), pp. 349–356.